MXenes: from past to future perspectives

Massoud Malaki, Xiantao Jiang, Hanlin Wang, Ramakrishna Podila, Han Zhang, Paolo Samorì, Rajender S. Varma

MXenes: from past to future perspectives

Massoud Malaki[1*], Xiantao Jiang[2,3], Hanlin Wang[4], Ramakrishna Podila[5], Han Zhang[3*], Paolo Samorì[4*], Rajender S. Varma[6*]

[1] *Department of Mechanical Engineering, Isfahan University of Technology, Isfahan, 84156-83111, Iran*

[2] *School of Science, Sun Yat-Sen University, Shen Zhen 518107, China*

[3] *Shenzhen Engineering Laboratory of Phosphorene and Optoelectronics, Collaborative Innovation Center for Optoelectronic Science and Technology, College of Optoelectronic Engineering, Shenzhen University, Shenzhen 518060, China*

[4] *Université de Strasbourg and CNRS, ISIS, 8 allée Gaspard Monge, 67000 Strasbourg, France*

[5] *Laboratory of Nano-biophysics, Department of Physics and Astronomy, Clemson Nanomaterials Institute, Clemson University, Clemson, SC 29634, USA*

[6] *Regional Centre of Advanced Technologies and Materials, Palacký University in Olomouc, Šlechtitelů 27, 783 71 Olomouc, Czech Republic*

[†] *M. Malaki, X. Jiang and H. Wang contributed equally to this manuscript.*

Contents

Abstract

MXenes have recently emerged as a revolutionary class of material displaying exceptional tailored-made properties. The onward journey and remarkable rise are establishing MXene-based materials as multifaceted playgrounds for the technology-oriented explorations and are offering a tool-box for the ad hoc tailoring of advanced materials capable to effectively address current and future societal challenges. Unexpected applications have witnessed a tremendous growth owing to the material's unique chemical and physical properties including, among others, optical, electrical, mechanical and thermal characteristics. Attaining an in-depth and critical understanding on the broadest arsenal of such unique and new properties as well as the synergistic effects of the assorted characteristics will play a pivotal role for new discoveries in both, research and industrial sectors. Herein, the current challenges, bottlenecks, controversies, as well as emerging opportunities are critically discussed by providing, in a single package, comprehensive insight into chemical and physical properties with a particular focus on their disruptive potential for technological applications. The key fundamental properties ranging from electrical, magnetic, thermal, mechanical, tribological to sensing features are elucidated to stimulate emerging opportunities and lucrative potentials with the ultimate goal being the technological exploitation of newfound materials and structures with targeted attributes.

Keywords: MXenes, 2D materials, nanomaterial, nanotechnology

1. Introduction

The development of 2D materials such as MXenes, having a thickness on the atomic scale, have represented a true cornerstone in materials science due to their exceptional tailored-made properties [1-8]. As transition metal carbides (TMCs), nitrides or carbonitrides, MXenes are usually produced by the selective etching of *A* element from a ternary phase of $M_{n+1}AX_n$; *A* refers to the elements of IIIA or IVA group [6, 9-11]. MXene, a new group of 2D materials, was firstly synthesized in 2011 by Gogotsi et al [2]. MXene originates from the MAX ceramic group, and represents transition metal carbides, nitrides, and carbonitrides, with a general formula of $M_{n+1}X_nT_x$, where M stands for an early transition metal, X is C and/or N, and T is a surface termination unit. There are over 30 types of MXenes have been experimentally produced, including ordered mono-M, ordered double-M and solid-solution M elements, i-MXene, and so forth [12-15]. Mostly, MXenes are produced by HF acid etching method, selectively extracting the A elements from their MAX precursors. However, the strong acidity of HF might be harmful to the operator and the environment. Researchers have proposed diverse approaches to further optimize the traditional method and obtain new MXene materials. Representative methods include molten salt synthesis [16], anodic etching in aqueous electrolyte (NH_4Cl+TMAOH)

without using acid [17], chemical transformations (e.g. ammoniation of transition metal carbides, carburization of transition metal sulfide, deoxygenation and carburization of carbides) [18-20], salt-templated growth [21], and Lewis acidic etching [22]. The outside layer of MXene is consistent with metal elements, which are highly active in the solution-based synthesis procedures; a majority of surface terminations (e.g. hydroxyl, oxygen, or fluorine) will be formed, leading to a hydrophilicity nature of MXene [23-27]. Thanks to the great variety of element components of MXene and multiple synthesis approaches, it has shown exceptional programmable properties [28, 29], by changing crystal structures [30-32], the synthesis conditions (HF, LiF/HCl, molten salt, halogenation, etc.) [22, 27, 33-36], or divacancy in MXenes [37].

Based on the following reaction, MXene can be produced where the *A* element can be etched off from the MAX phase leading to an accordion like structure as shown in **Fig. 1** [2]; the resulting material is delaminated and exfoliated to reach a final product. Exfoliation is sometime done by a hand shaking or proper ultrasonication [10, 38-43].

$$M_{n+1}AlX_n + 3HF \rightarrow M_{n+1}X_n + AlF_3 + 1.5\ H_2$$

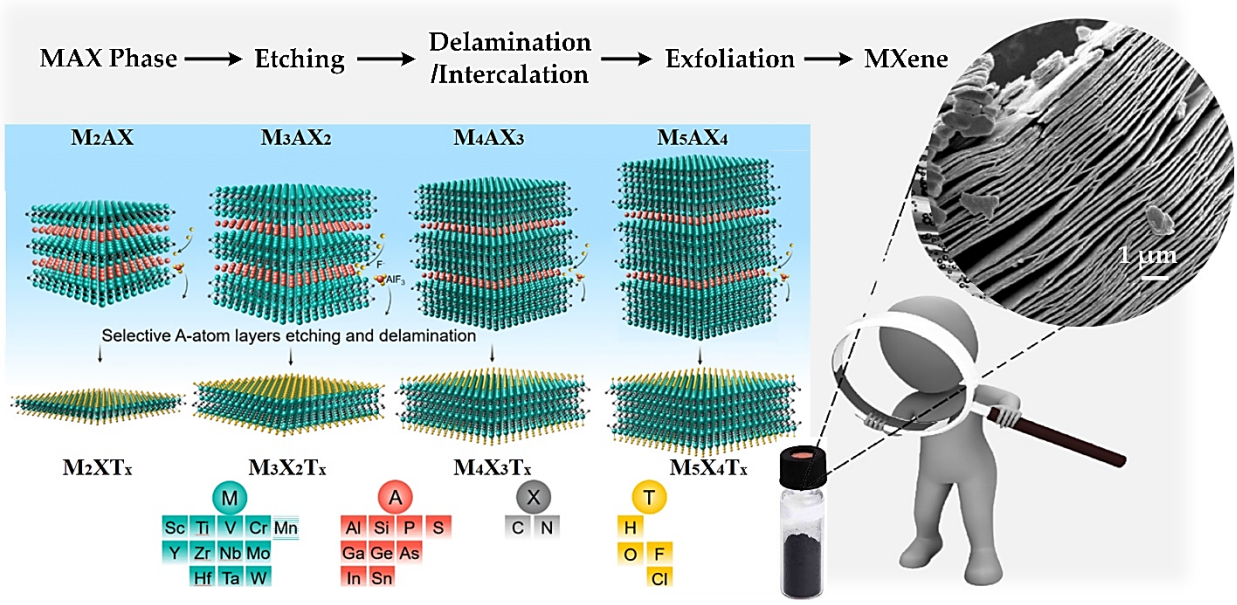

Fig. 1. Different elements in MXene and MAX compound with the synthesis steps of MXene 2D nanoflakes from their parent MAX.

As mentioned earlier, MXenes are highly programmable. It has been shown, for example, that different compositions and crystal phases may result in different electronic properties; for instance, some of them are metallic, and some others are semiconducting with varying band structures, exhibiting different energy levels for different electrochemical processes. Replacing titanium with molybdenum in MXene outer layer may lead to a transition from metallic to

semi-conducting behavior [44] being probably owing to the hybridization of p orbitals in F or O and d orbitals in M element of MXenes [11, 45, 46]. Pinto et al. [47] showed a superior electrochemical performance of MoV solid solution MXenes with more Mo tend to be better for electrochemistry. Lim et al. [48] discussed the effect of synthesis procedures on electrochemical processes; it was reported that the processes of etching, exfoliation, intercalation and delamination are directly responsible for appearing a variety of functional groups of T_x, being directly dictating tailored properties such as semiconductivity, ferromagnetism, and so on. The effect of flake size and morphology effects on the electrochemical performance was studied by Maleski et al. [49] wherein varied lateral sizes, ranging from 0.1 to ~5 μm, could be first achieved by tuning the sonication conditions; then $Ti_3C_2T_x$ flake-size dependence of electrochemical performance was proven, finally the lateral sizes of about 1 μm provided the best electrochemical behavior.

MXene has been revolutionizing many fields due to exceptional programmable properties. The proper understanding about these new 2D materials enormously facilitates the underlying processes for syntheses, processing and applications leading to novel products and devices with superior sustainability, performance and efficiency.

MXene based materials have been exploited in numerous applications in a variety of fields ranging from energy materials, lubricating additives, biomaterials, nanocomposites, etc. owing to excellent properties [6, 50, 51]. They have been used in many fields such as electromagnetic shielding [52], electronics [53], electrical and thermal conductors [54], environmental remediations [55], supercapacitors [56], photocatalysts [57], sensors [58], batteries [59], self-healing composites [60-62], water purifications [63], antibacterial materials [64-66], actuators [67], and other advanced materials and structures [68-70]. Due to the mechano-ceramic nature, MXenes exhibit excellent mechanical, thermal, optical, electrical, magnetic, and sensing properties [50, 71].

MXenes have witnessed a tremendous growth due to their unique and special attributes especially those physical properties, namely electrical, thermal, optical, magnetic, tribological, mechanical and sensing. Undoubtedly, having a comprehensive insight not about a particular trait but all the newly developed properties as well as the synergistic effects of assorted features will play a pivotal role for new discoveries in both, research, and industrial areas. The onward journey and rise of the MXene-based materials would inspire the next generation of chemists, physicists and engineers to tailor and design persuasive advanced materials that could effectively address major societal challenges. The present review, firstly discusses the material's basic mechanical and tribological properties and then focusses on optical and thermal characteristics in view of potential new discoveries and future concerns. Following, after offering a comprehensive insight into their magnetic, electrical and storage features, we discuss how such unique properties can be used for physical and chemical sensing applications. The manuscript ends-up with a summary and outlooks, by paying a special attention to the

challenges, research pitfalls, finally by proposing a comprehensive roadmap for the upcoming efforts.

2. Mechanical aspects

Although a significant deal of research activities has been branched out to magnetic, electromagnetic, thermal, optical, electrical, sensing and other traits, still the mechanical properties of MXene nanoflakes and their hybrids are yet to be fully investigated and understood as abundant questions are still un-resolved to date.

MXene and its mechanical properties are greatly dependent on fabrication routes/techniques as the structural defects, voids and misalignments considerably deteriorate the final mechanical features such as elastic modulus, tensile strength, among others [50, 72]. The most important parameter in the synthesis process is the composition and chemical properties of MAX phase. The bonding type between M and A layers is metallic while it is 3-4 times stronger than mixed ionic/covalent bond between M and X layers. Unlike graphene being mechanically exfoliated from graphite, MXene cannot be mechanically achieved from the parent MAX phase; however, it can be synthesized through a selective etching process whose parameters significantly affect the final strength of MXene. The most important parameters of selective etching are as follows, being directly or indirectly influencing the mechanical properties:

- Etchant type
- Etchant concentration
- Etchant temperature
- Environment
- Etching duration

Harsh or concentrated etching conditions may generally produce more atomic vacancies, defects, or even smaller flake sizes deteriorating mechanical performance [3, 73, 74]. The synthesis in inert gas or vacuum conditions may generally produce high quality MXenes and that it is highly recommended to avoid the high temperatures while synthesizing MXenes. Further, delamination processes may also affect the defects, flake size and vacancies which in turn exert influence on the mechanical strength. For example, the flake size of 3-12 μm and less than 1 μm can be achieved when charged ions like Li^+ and large molecules like DMSO, TBAOH, & TMAOH are utilized, respectively.

Mechanical behavior of MXenes has been explored by density function theory (DFT) analyses and molecular dynamics (MD) approaches [74-82]; however, these techniques still have a long way to address the exact mechanical behavior.

2.1. Atomistic insight

From the atomistic viewpoint, the bonding strength between a transition metal and C/N is a mixed ionic, metallic and covalent bonding owing to the electron orbitals of *d* and *s* in the

transitional metals and the *p*-orbitals of carbon or nitrogen atoms [83-85]. The primary bond between the M and X atoms is the combination of ionic bond with the endowed electrons from M to X as well as a mix of σ and π covalent bonds [86, 87]. The bonding strength between X-X atoms is very weak owing to large distance between these atoms. M-M bond contributes less than M-X bond to the energy of lattice structure. The length and energy of a given bond are the two important values to assess bonding stiffness or bonding strength. Those atomic pairs with shorter length and higher bonding energies are expected to have a higher stiffness (see Fig. 2a-b). In addition, those M-C bonds with higher group number of M are seen to be stiffer (Fig. 2b). According to the literature, Ti, Mo, and W are of the stiffest M-C bonds. M-N pairs, however, have a better mechanical property than that of those M-C bonds since the elastic module of TMNs are usually higher than those TMCs probably owing to the additional electrons of N than C (for example, TiN has an elastic module of ~1.4 times more than TiC) [88].

It is of crucial importance to distinguish the stiffness of 3D crystalline binary transition metal carbides/nitrides materials with that of 2D plane MXenes. In fact, the elastic moduli of MXene usually decreases by increasing the thickness of monolayer MXenes; moreover, the termination groups are estimated to enhance the 2D stiffness (Fig. 2b-c). In addition, the carbon or nitrogen deficiencies may reduce M-X bond strength and hence a reduced stiffness is expected [89, 90].

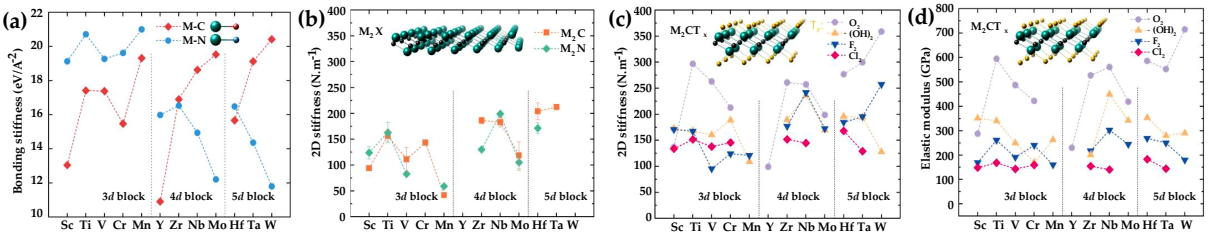

Fig. 2. (a) the bonding stiffness values for early transition metals, (b) the 2D stiffness of pristine MXenes, (c) the 2D stiffness of the terminated MXenes (d) the elastic modulus of the terminated MXenes. Adapted from Ref. [88]. Copyright © 2021.

It is thought that those M-M interactions might be responsible to the reduced 2D stiffness as the bare Ti_2C exhibited a lower stiffness value than those predicted for bare Ti_3C_2 or Ti_4C_2; in other words, the number of interior Ti-C layers of Ti_3C_2 or Ti_4C_2 structures is more than Ti_2C MXene and lower Ti-Ti interactions are seen. The 2D stiffness of bare Ti_2C, Ti_3C_2 and Ti_4C_2 are respectively 112.9 Nm^{-1}, 258.2 Nm^{-1}, and 323.3 Nm^{-1} and a similar trend was interestingly seen for the 2D stiffness of bare transition titanium nitrides 118.4 Nm^{-1}, 241.9 Nm^{-1}, and 353.3 Nm^{-1} respectively, when n = 1, 2, & 3 [79]. In another study conducted by Plummer *et al.* [74] on functionalized MXenes, it was found that oxygen terminated Ti_2CO_2 MXene reveals a higher stiffness than $Ti_3C_2O_2$ probably because of the presence of oxygen functionalization group.

Investigations on other MXenes with different transition metals like Mo, Cr and W show that the thicker MXenes (M_4C_3) have a higher stiffness as it is 8.19 eV/Å^{-2} for Mo_4C_3 compared to 7.84 eV/Å^{-2} for Mo_2C since the M-M interactions are weaker in those thicker MXenes [91, 92].

The bonding strength of M-T_x is an important parameter affecting the mechanical property of the final MXene or MXene based hybrids. The strongest M-T_x bods are for the 4th group of early TMCs due to the electron donation from halide to transition metal as well as less electronegativity differences between the transition metals of 5th/6th groups and surface functionalization groups (see Fig. 2c-d). While oxygen termination group may usually result in a better 2D stiffness value of MXenes, the other functionalization groups, i.e. -Cl, -F and, -OH may have inferior or negligible effects on the 2D stiffness [93, 94] mostly owing to the fact that the oxygen termination group could effectively restrict M-M interactions, more than other terminating groups, being consequently increasing the 2D stiffness.

2.2. Practical characterizations

Although there exist several numerical or computational analysis reports on the mechanical properties of MXenes, a few practical experiments have yet been performed [95, 96] and hence experimental exploration of MXenes is really an uncharted territory. Lipatov *et al.* could measure, for the first time, the main mechanical properties, namely Young's modulus, force-displacement (F- δ) and the fracture force values of $Ti_3C_2T_x$ [95] and $Nb_4C_3T_x$ [96] as depicted in **Fig. 3**.

The Young's modulus of 0.33 ± 0.03 TPa was quantified for a single-layer $Ti_3C_2T_x$. They found that for those small forces of less than 10 nN, a linear dependency between force and displacement is observed (F~δ); however, a non-linear cubic relationship (F~δ^3) is revealed when the applied force is larger than 10 nN. The elastic modulus of 2L $Ti_3C_2T_x$ is twice the measured value for 1L $Ti_3C_2T_x$.

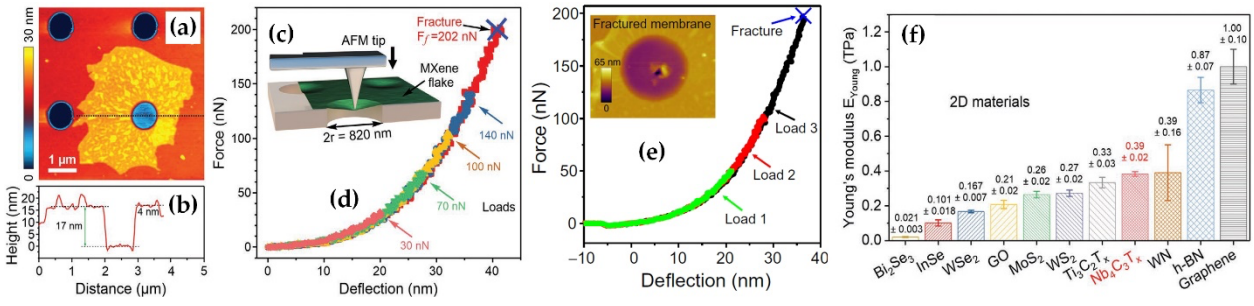

Fig. 3. Mechanical characterization of $Nb_4C_3T_x$ and $Ti_3C_2T_x$ MXenes by AFM nano-indentation. (a) a representative $Nb_4C_3T_x$ sample covering on an 820 nm microwell. (b) the AFM height profile of MXene membrane across the well where it is stretched by ~7 nm on a Si/SiO2

substrate. (c) the schematic view of the nanoindentation process. (d) the force-deflection curves of $Nb_4C_3T_x$ MXene (e) the force-displacement curves for the $Ti_3C_2T_x$. (f) a comparison of elastic values of different 2D materials including $Nb_4C_3T_x$ and $Ti_3C_2T_x$. (a-d, f) adapted from Ref. [96] Copyright 2020. (e) adapted from Ref. [95]. Copyright 2018.

The effective Young's modulus of 386 ± 13 GPa and the breaking strength of 386 ± 1.6 GPa are achieved for single-layer $Nb_4C_3T_x$ being the highest amount among solution-processed 2D nanosheets, e.g. $Ti_3C_2T_x$, graphene oxide (GO) or reduced graphene oxide (rGO) [96]. Owing to acid-etching induced structural defects as well as those terminating groups increasing the sheet thickness without bolstering mechanical properties, the elastic modulus of bulk carbides is slightly greater than their corresponding MXenes. Further, the elastic modulus of bulk TiC (400 GPa) and $Ti_3C_2T_x$ (0.33 ± 0.03 TPa) are respectively lower than bulk NbC (452-488 GPa) and $Nb_4C_3T_x$ (0.386 ± 13 TPa) [95, 96]. The closeness of elastic property measured for the bulk NbC and its $Nb_4C_3T_x$ MXene may be helpful in predicting the elasticity of other MXenes for which no experimentally achieved elasticity has been measured and that it can be estimated through the values known for their bulk carbides.

The 2D stiffness of monolayer $Ti_3C_2T_x$ and $Nb_4C_3T_x$ MXenes are respectively measured as 326±29 Nm^{-1} and 486±18 Nm^{-1} agreeing with the earlier discussion that thicker MXenes have a higher 2D stiffness and that Nb-C bond is stiffer than Ti-C bond [95, 96]. It can be concluded that the 2D stiffness values predicted computationally (366 Nm^{-1} for $Ti_3C_2O_2$ and 605 Nm^{-1} for $Nb_4C_3O_2$ [97]) are greater than those obtained experimentally, probably due to possible vacancies, defects or imperfections in the MXenes being tested in the practical measurements.

The mechanical performance of MXenes and their hybrids are strongly dependent on many parameters ranging from chemical composition to fabrication techniques. For example, the randomly oriented $Ti_3C_2T_x$ MXene film exhibited a poor tensile strength of 40 MPa [98] while those well-oriented MXene based strips may provide a better tensile strength value of ~568 MPa [99] attaining more than 14 times higher mechanical property. In an attempt, Zhang *et al.* [99] revealed that the fabrication technique could be of significant importance as they observed the blade-coating manufacturing method may provide a quite better mechanical strength compared to filtration process.

It is obvious that the knowledge and information in this field are insufficient and further research efforts, not only on computational studies but also on practical examinations must be conducted to find out the effects of different playing role parameters such as thickness, temperature, loading conditions, materials variables, etc. on mechanical properties.

2.3. Computational characterizations

More than any other methods, MXenes have been studied by computational studies; however, still a lot of opportunities are available in this intact field since practical characterizations are

strongly limited to characterization tools and facilities. To date, many computational efforts have been performed to predict the mechanical properties of MXenes from which molecular dynamics (MD) and density functional theory (DFT) [81, 100, 101] were mostly used in the computations. First principle calculations was firstly proposed in 2012 by Kurtoglu *et al.* [102] wherein the elasticity of pristine/bare MXenes (i.e. MXene with no termination) was examined by a DFT analysis; the moduli of exceeding 600 GPa was realized when the MXene nanosheet was stressed along its basal planes. The elastic constant of c_{11} was measured as two times more than that of corresponding MAX phase.

Based on computational studies, it was found that the hexagonal Ti_2C single-layer MXene has a higher stiffness than MoS_2; however, was is lower than the values reported for graphene or hexagonal boron nitride (h-BN) [100]. The mechanical strength of about 0.33 TPa was predicted for mono-layer $Ti_3C_2T_x$ MXene flakes being considerably lower than the value of ~1 TPa Young's modulus for graphene; nonetheless, MXene is stiffer than some other 2D nanomaterials like graphene oxides with ~0.2 TPa Young's modulus of [103]. **Table 1** provides a list of 2D materials with their mechanical properties wherein Y_s (N/m) is in-plane Young's modulus, c_{11} (N/m) and c_{12} (N/m) are both elastic constants, and that υ is Poisson's ratio. **Table 2** presents the structural and elastic properties of different MXenes wherein the value of c_{11} for M_2X nanoflakes is about 40% better than their MAX parents attributing to strong M-X bonds in MXenes. Regarding M_4X_3 & M_3X_2, the improvement in c_{11} is roughly about 70%.

Table 1. Mechanical property of different 2D materials

	Ti_2C	**h-BN**	**MoS_2**	**Graphene**
Y_s	130 [100]	267 [104], 271 [105], 276 [106], 311 [107], 318 [108]	118 [109], 119 [108], 123 [110], 129 [105], 146 [111]	312 [112], 330 [113], 335 [104], 339 [114], 342 [106], 345 [105], 348 [115]
c_{11}	137 [100]	290 [106], 335 [107]	130 [105], 140 [105]	353 [106], 358 [115], 342 [113], 347 [114]
c_{12}	32 [100]	64 [106], 89 [107]	40 [105]	60 [115], 61 [106], 64 [113], 55 [114]
υ	0.23 [100]	0.17 [108], 0.21 [104, 105], 0.22 [106], 0.27 [107]	0.25 [108, 110], 0.29 [105], 0.31 [109]	0.15 [105], 0.16 [104, 114], 0.17 [106, 115], 0.19 [113], 0.31 [112]

Table 2. The elastic moduli of C_{11} for different MXenes and MAX phases; C_{11} values of MAX compound are in the brackets [102].

Type of MXene	**M_2C**						**M_3C_2**		**M_4C_3**	
Name	Ti_2C	V_2C	Cr_2C	Zr_2C	Hf_2C	Ta_2C	Ti_3C_2	Ta_3C_2	Ti_4C_3	Ta_4C_3
C_{11} (GPa)	638 (312)	718 (338)	690 (340)	594 (261)	658 (291)	788 (334)	523 (368)	575 (417)	512 (403)	633 (437)

Mono-layer MXene has usually higher bending rigidity than graphene since it is three times thicker rendering them a superior nanosheets for composite manufacturing [2, 4, 102, 116]. Sometimes, their mechanical performance can be further improved when they are composited with other

nanomaterials and structures; for instance, ~226.3 MPa and ~6.2 MJ m^{-3} are respectively the tensile and toughness values of MXene-functionalized graphene oxides (GOs) being ~2.8 time and ~6.9 times greater than the corresponding values obtained from the neat GOs [117].

According to the literature, surface termination has a considerable influence on the mechanical property of MXenes. Based on a DFT analysis, Ti_2C MXene sustained 9.5%, 18% and 17% tensile strains when it is respectively stressed in biaxial and uniaxial in *x* and *y* orientations (see **Fig. 4**a-b) [101]. However, the mentioned values respectively increased to 20%, 28% and 26.5% when the MXene is terminated by oxygen slowing down the failure of titanium atomic layer and consequently better toughness behavior is achieved as depicted in **Fig. 4**b. As a comparison, graphene has a uniaxial strain value of 15% being much lower than the value attained from the oxygen terminated Ti_2CO_2 MXene. As seen in **Fig. 4**c-d, terminating groups could improve critical strains as well as fracture toughness to a great extent even though the Young's modulus is sacrificed to some extent; furthermore, it is clear from **Fig. 4**e-f, the Young's modulus of MXene nanosheets considerably depends on *'n'* in $Ti_{n+1}C_n$ reducing with increasing *'n'* from 1 to 3 in both bare and terminated MXenes [67, 68]. **Fig. 5** provides the elastic constant values of c_{11} for a variety of MXenes, namely V_2C [102, 118], Ti_3C_2 [79, 102, 119, 120], Hf_2C [102, 118], Ti_2C [79, 102, 118], Zr3C2 [120], Ta_2C [102, 118], Cr_2C [102, 118], and Zr_2C [102, 118] wherein the pristine MXenes exhibit the highest elastic moduli and that elastic behavior reduces with *'n'* in $Ti_{n+1}C_n$ increasing from 1 to 3 (for instance see the pair of Ti_2C and Ti_3C_2 in **Fig. 5**). The mentioned discussion is also valid for those terminated MXenes as it has been seen that Ti_2CO_2 nano-flakes exhibit a stiffer manner than $Ti_3C_2O_2$ MXene [78]. Among terminating groups, namely -O, -OH, and -F, those with oxygen functional groups provide better elasticity, as seen in **Fig. 5**.

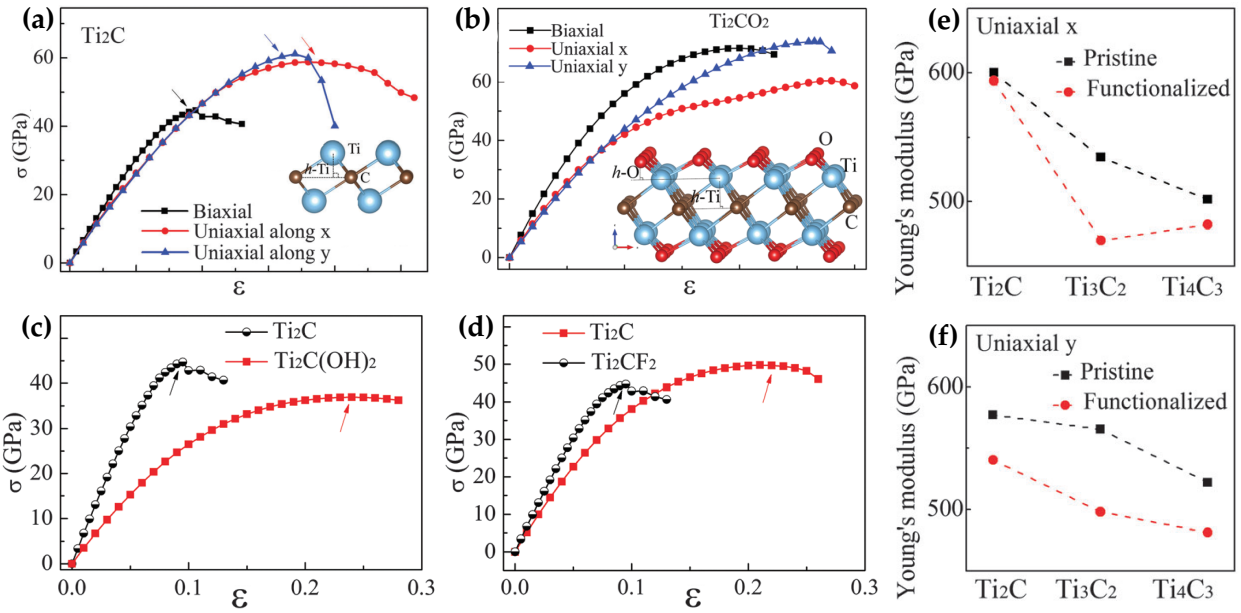

Fig. 4. The simulated stress-strain for bare (a), -O_2 (b), -OH (c) and -F (d) terminated Ti_2C MXene. The Young's modulus of bare and functionalized MXenes decreasing with increasing n in $Ti_{n+1}C_n$ (n=1-3) (e-f). Adapted from Ref. [101]. Copyright 2015.

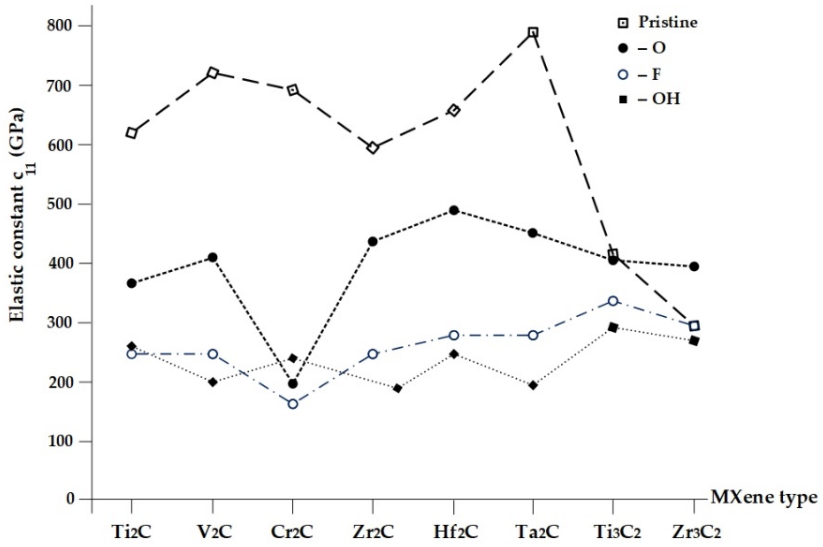

Fig. 5. The effect of different terminating groups on the elastic constant of c_{11} for a variety of MXenes

Apart from the effect of surface terminations, the mechanical properties are strongly dependent on temperature. According to a recent DFT analysis, Ti_2CO_2 MXene began to soften with the increasing temperature mostly due to a losing stiffness as well as higher expansion of interatomic spaces; in the meantime, one cannot neglect the risk of oxidation while synthesis process is carried out at higher temperatures [78]. Moreover, DFT simulation results revealed that

TMNs ($Ti_{n+1}N_n$) usually possess a greater preference to adhere to functional groups and as a result a better in-plane Young's modulus is expected than those values attained from TMCs ($Ti_{n+1}C_n$) attributing to larger lattice constants and monolayer thicknesses [79].

3. Tribology

Reducing friction has always been one of the greatest challenges in industrial applications. Laminated structures/nanomaterials like MoS_2, graphene or MXene have a great potential to reduce friction and wear in different tribological practices [121, 122]. In general, MXenes are used either as solid lubricant in dry lubrication systems or as an additive agent in host liquid media, both to reduce friction, wear and surface damages [123].

MXenes display special features among which its hydrophilic surface and rich chemistry makes them promising candidates for anti-friction purposes. For instance, machine component coated by $Ti_3C_2T_x$ MXene exhibited a reduction in wear rate and friction torque by a factor of about 2.9 and 3.2, respectively wherein the service life in higher loaded rolling-sliding contacts could increase by a factor of 2.1 times being comparable with those other 2D nanosheets like graphene, amorphous carbon, etc. [124].

Tribological features are mostly influenced by M-X chemistry and composition, flake size/geometry, surface functional groups, loading conditions as well as stoichiometry among others [50, 123, 125-131]. It seems MXenes with different M elements have different tribological characteristics as it was seen that Nb_2C has less friction coefficient than Ti_3C_2 while working under the same process conditions, owing most probably to surface dipole moment density [132]. Researches revealed that the thinner MXene flakes (e.g. single layer thickness) have much better anti-friction properties as compared to thicker ones [50, 123]. As one of the earliest computational analysis performed by DFT [126], it is seen that MXenes with larger inter-layer spacings demonstrate easier sliding behavior with lower friction behavior. It should be noted that those friction coefficients reported for MXenes (i.e. 0.06-0.1) cannot yet reach the ones measured for other nanomaterials and hence further research efforts have to be made on the chemistry and physics of MXenes' tribology [133]. AFM studies revealed that the adhesion and friction forces increase when the temperature goes up [128] (see **Fig. 6**). Contact pressure is a dominant factor affecting the tribology of MXene based lubricants. In moderate-pressure contacts with 20% humidity, $Ti_3C_2T_x$ MXene brought a 2.3-fold friction and a 2.7-fold wear volume reductions in steel-steel contacts owing to in-situ formation of tribofilms being a frequently reported lubrication mechanisms; under too high pressures, the mentioned tribofilm was partially ruptured losing its protective wear resistance; further, no wear or friction reductions were observed in the higher humidity of 80% due to the expansion of basal spacings [134]. As mentioned earlier, the formation of tribofilms has repeatedly been believed as the main mechanism of lowering friction values and wear rates especially in solid lubrication systems;

however, direct characterization has not yet been conducted to understand the exact tribological nature of the MXene based lubrication systems.

It has been speculated that amino-functionalization of few-layered $Ti_3C_2T_x$ reinforced composite coating could considerably reduce the corrosion resistance up to 3.12×10^9 Ω cm^2 and wear reduction up to 72.74% owing mostly to (i) the well-dispersion of amino-functionalized MXene sheets in organic material, (ii) a great adhesion between the coating and substrate as well as (iii) those intrinsic properties of MXene sheets [135]. It was shown that MXene reinforced metal matrix composites (MMCs), like Cu or Al based MMCs, reduced the friction coefficient and wear rate notably [136]. The reduction in friction coefficient by a factor of 2.0 and 2.5 has been respectively reported for Cu [60] and Al [137, 138] based MMCs.

Although MXenes have a great potential to reduce wear and friction, their performance can be further improved in super-low friction lubrication systems when hybridized with other nanomaterials like nanodiamond or graphene [139]. It has been reported that the friction coefficient and abrasion resistance performance of Ti_3C_2 could be further enhanced when graphene is also introduced between the mating surfaces achieving a superlubricity regime with the friction coefficient of 0.0067 ± 0.0017 in a dry nitrogen condition; while MXene has a great capacity to reduce friction coefficient and endow excellent anti-wear property, the addition of graphene may also boost wear resistance by a factor of 2.0 and decrease the friction coefficient by 37.3% as compared to the composite coated by MXene alone [140].

Owing to hydrophilic nature endowed by terminating groups, the stability of MXenes in apolar oils is harder than those polar media like water. Also, it is postulated that surface functionalization not only promotes better dispersion and distribution but also enhance tribological characteristics in MXene based lubrication systems. Further experimental efforts should be undertaken to validate those values suggested by those computational DTF and MD analysis tools. According to the DFT and MD simulation efforts of Zhang *et al.* [125], the friction coefficient of 0.24-0.27 and 0.10-0.14 are, respectively estimated for the bare and terminated $Ti_{n+1}C_n$ (n=1-3). They also indicated that the vacancies, either Ti or oxygen terminating groups, could increase the surface roughness and the friction coefficient owing to additional attractive forces in these regions between the two rubbing surfaces. Further, it has been found that the termination by -OH and $-OCH_3$ has a better anti-friction property compared to those oxygen terminated MXenes [125]. It has been reported that 4.0% $Ti_3C_2T_x$ MXene could act as solid lubricant to enormously reduce the friction coefficient by about 300% wherein the main wear mechanisms such as abrasive, adhesive and tribochemical effects could considerably be suppressed; in addition, it is seen that surface termination groups could tailor interfacial bonding strength and therefore lowering shear strength and friction force are expected [141]. The pristine type of MXene exhibits the greatest friction coefficient due to stronger interlayer interactions. Zhang *et al.* [125] obtained a friction coefficient of 0.24-0.27 and 0.10-0.14 respectively for O- and OH-terminated

MXenes while Rosenkranza *et al.* [141] reported an intermediate value of 0.21 for MXenes containing both oxygen and fluorine termination groups.

The optimum concentration or weight fraction of MXene is a vital parameter in wet lubrication systems since the lower weight fraction may not have enough influence while too much amount of MXene nanoflakes may worsen the lubrication situation owing to severe agglomerations, particle breakage, and that the MXene sheets might not be able to enter the narrow contact areas. As shown in **Fig. 6**, $Ti_3C_2T_x$ coated by TiO_2 when added to a base oil using a liquid-phase reaction wherein those oils containing 1.0 wt.% MXene hybrids exhibit the best anti-friction and anti-wear properties due to a uniform layer of tribo-films smoothening the sliding conditions and reducing shear stresses between the rubbing surfaces [142]. The layer of shielding tribofilm has been found to be unstable and discontinuous in lower weight fractions (< 0.8 wt.%) of $Ti_3C_2T_x$ nanoparticles in PAO8 base oil; however, the addition of 0.8 wt.% MXene flakes provide the best anti-friction and anti-wear protective features [131]. In fact, under the optimum condition (=0.8 wt.%), the wear volume of 0.5×10^4 μm^3 and the friction coefficient of 0.11 are reported providing a consistent lubrication status hindering a direct contact between the mating surfaces [131]. Highly exfoliated MXenes could notably decrease the friction and anti-wear properties owing to the MXene adherence to the mating contacts. On the other hand, the lubrication behavior can be deteriorated if an excessive amount of filler nanosheets (>> 0.8 wt.%) are incorporated wherein the friction coefficient will even be higher than the base un-filled oil [131]. The friction coefficient of different MXene-oil mixture is listed in **Table 3**.

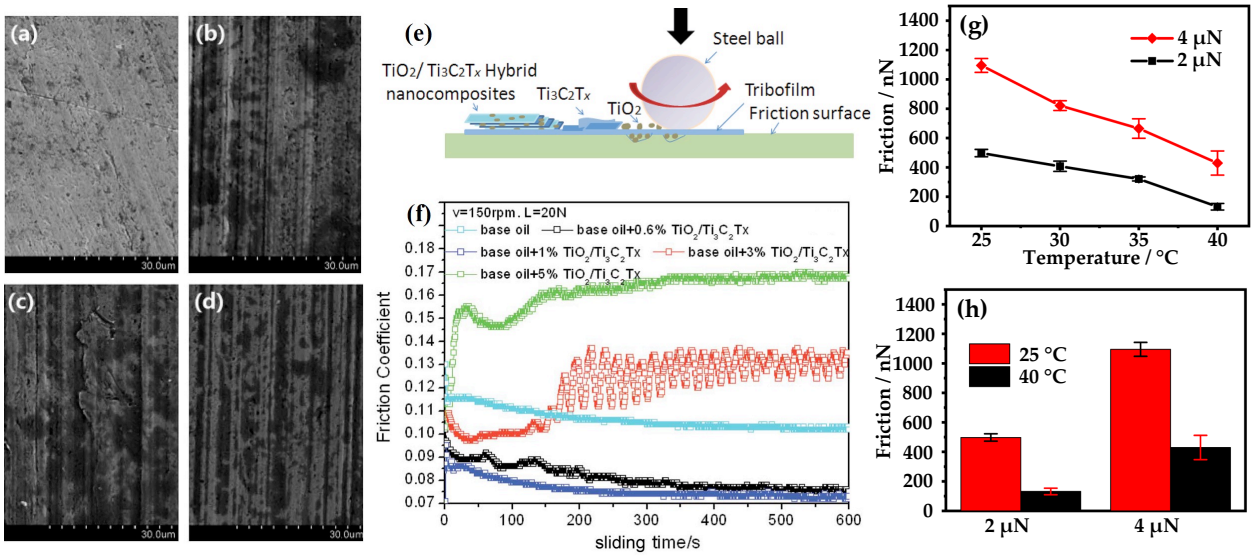

Fig. 6. SEM images of the worn tracks lubricated by base oil having different weight fractions of 0.0 wt.% (a), 0.6 wt.% (b), 3.0 wt.% (c), and 5.0 wt.% (d) $TiO_2/Ti_3C_2T_x$ schematically depicted in (e). The variation of friction coefficient vs. sliding time are shown in (f). The friction behavior of

Ti_3C_2 MXene nanoflakes at varied temperatures and pressures are respectively shown in (g) and (h). (a-f) Adapted from Ref. [142] Copyright 2017. (g-h) Adopted from Ref. [128] Copyright 2019.

As aforementioned, the degree of exfoliation is another key parameter in MXene-based wet lubrication systems; the coefficient of friction and wear rate can be substantially decreased if only small amount of exfoliated MXene is employed [131]. A ~98.4% reduction in the coefficient of friction can be reached if 0.5-6.0 wt.% Ti_3C_2 nanoflakes with the thicknesses of 10-20 nm are homogenously dispersed in a base oil using a pressureless sintering technique wherein it is seen that the coefficient of friction considerably could be reduced from 0.125 to 0.063 with increasing MXene additives from 0.0 to 1.0 wt.%, attributing to the mechanism of in-situ tribo-film layer formed between the worn surfaces [143]. Ascribed to the same tribofilm formation mechanism being revealed by an EDS analysis, it has been found that 1.0 wt.% $Ti_3C_2(OH)_2$ MXene nanosheets with the thicknesses of 10-20 nm added to base oil to lubricate steel component are able to act as an effective agent to drastically reduce tribological problems by lowering shear stresses and avoiding direct contact between the two rubbing surfaces [130].

Table 3. Friction coefficient in different MXene-Oil mixtures

wt.%	**0.8**	**1.0**	**1.0**	**1.0**	**1.0**
MXene type	$Ti_3C_2T_x$	$Ti_3C_2T_x/TiO_2$	$Ti_3C_2T_x$	$Ti_3C_2T_x$	$Ti_3C_2T_x$
Base oil type	PAO8	PAO8	Paraffin	100 SN	PAO8
COF of base oil	0.126	0.103.	0.125	0.092	0.111
COF of filled oil	0.114	0.073	0.063	0.75	0.081
Ref.	131	142	143	130	144

Alongside anti-friction and anti-wear properties, MXene flakes can also be considered to damp the vibrational energy, noise, and impact in relevant critical applications [145]. The loss tangent (tan δ) of 0.37 taken for MXene is 200% better over that of its pure MAX ascribing to sliding/shearing phenomena, interlayer bonding interactions, as well as the compression mechanisms. The damping stability of 50,000 cycles, low friction coefficient, the presence of functional groups and having those van der Waals forces make MXene an extraordinary material for energy dissipation applications [145]. It has also been concluded that MXene can be employed as a coating material to reduce friction and wear of metals; Ti_3C_2 with 200 nm thickness coated on copper was found to provide one tenth wear rate and one forth friction coefficient as compared to uncoated samples as the mentioned protective layer prevents the direct contact and produces a carbon-rich tribofilm brough by the friction phenomenon between the rubbing surfaces [146].

Heat and temperature are the two important parameters influencing the tribological behavior of MXene-based lubricants that have not yet been fully investigated. The stability and

performance of MXenes under different loading and environmental conditions are almost unknown in tribological applications. Those issues such as degradation over the time, particle breakage, agglomerations, oxidation in different media, change under elaborated temperatures or pressures, possible reactions among MXene sheets, as well as those structural defects are yet to be characterized in MXene based tribological applications. Advanced material characterization setups should be developed and employed to study the dispersion and agglomeration state as they tend to change with time. Further investigation is demanded to further grasp the effect of flake size (lateral, thickness), termination group type(s), process parameters, etc. on the surface and tribological features of MXene-based lubrication systems.

4. Optical & thermal MXenes

Light-matter interactions in a material are truly instrumental for their application in functional devices. This section is devoted to the optical properties of MXenes. We first theoretically analyze the parameters that influence the optical properties, then reviewed the light-related phenomena in MXenes and the corresponding functional devices, ending up with a compelling perspective on the challenges and newly emerging opportunities.

Theoretically, the optical properties of 2D materials partially reflect the electron transitions in materials, and are determined by the electronic energy structure, including bandgaps, the density of states (DOS), symmetries, and momentums matching. Numerically, the optical properties are described as the dispersion of complex dielectric function, $\varepsilon(\omega) = \varepsilon_1(\omega) + i\varepsilon_2(\omega)$, where ω is the optical frequency, $\varepsilon_1(\omega)$ and $\varepsilon_2(\omega)$ are the real and imaginary component, or refractive index ($n = \sqrt{\varepsilon\mu}$). The imaginary part of the dielectric function can be theoretically calculated by summing empty states in the first Brillouin zone, once the energy structure has been obtained. The intraband contribution in MXene, especially in the lower photon energy regime is non-trivial and can be considered using a Drude model [147, 148]. The real part of the dielectric can be calculated from the imaginary part using the Kramers-Kronig relations.

The crystal structure of most MXenes through selective etching synthesis is hexagonal atomic lattice $P6_3/mmc$ inherits from their MAX parents. Therefore, the complex dielectric function (ε) tensor has only three non-zero primary components, $\varepsilon^{xx}(\omega) = \varepsilon^{yy}(\omega)\ and\ \varepsilon^{zz}(\omega)$ [147, 149]. Note, other crystal symmetries like orthorhombic, trigonal, and tortured cubic can be realized from different synthesis approaches [71]. The atomic stacking sequences of MXene ($M_{n+1}X_n$) monolayer indicates the sandwiching of carbides and/or nitrides by out layer transition metals, which will significantly affect the Fermi surface. The DOS near the Fermi surface has been theoretically predicted to be determined by the out layer transition metal d-electrons, whereas the energy bands below the Fermi surface are dominated by the p-electrons of X atoms [150, 151]. Therefore, non-terminated MXenes are normally metallic with a high DOS near the Fermi surface due to the transition metal out layers, and thus can be an excellent platform for the surface plasmonic generations and the use of highly conductive electrodes. Taking the 2D screening effect into

consideration, the exciton binding energy for monolayer Sc_2CCl_2 can be as large as 0.75 eV, which is close to the value observed in transition metal dichalcogenides (TMDs) [152]. Large photon flux absorption (1.32~7.80 mA/cm^2) is also predicted in this MXene, reveals a promising light-harvesting ability [153]. Similar to other 2D materials, the thickness or stacking layers of MXenes from monolayer, to few-layer and eventual bulk can also play an important role in the optical properties manipulations [154]. Typically, $M_{n+1}X_n$ with a smaller n value is predicted to be more optical transparent due to the sparser density of states in contrast to the larger n MXenes [147, 148, 155, 156].

Yet, the outer transition metal layers are chemically active and can be passivated by functional groups, such as -F, -OH, and -O, during the synthesis processes. The electronegative surface terminations seize electrons from the out layer transition metals and construct a new energy bands below the Fermi surface, and de-densify the DOS at the Fermi surface or lower the Fermi surface. The stronger electronegative of -O termination compared to -OH and -F may lead to a higher level of decoupling of conduction and valence band, and thus a lower Fermi surface and a larger bandgap breaking. Naguib *et al.* [2]found narrow bandgaps can be slit in -OH (Eg=0.05 eV) and -F (E_g=0.1 eV) terminated Ti_3C_2 MXene in the first report of MXene, while highly semiconductor optical properties can be observed in Ti_2CO_2 with a bandgap of 2.3 eV [148]. Furthermore, it is found -F and -OH terminated Ti_3C_2 have less optical attenuations than the pristine and -O terminated ones, suggesting the optical properties can be altered by changing the surface terminations that might be demanded in the application of transparent electrodes [156] (see **Fig. 7**a). The different transition metal elements in MXenes also alters the optical absorption properties. By using the density functional theory (DFT) method, it is found the Ti_2CO_2 features the smallest bandgap (E_g=0.92 eV) and the highest absorption coefficient in the visible regime, compared to Zr_2CO_2 (E_g=1.54 eV) and Hf_2CO_2 (E_g=1.75 eV), which consists of larger transition metal elements in the same group [149]. The narrower bandgap of Ti_2CO_2 is attributed to the lower energy of Ti 3d as compared to that of Hf and Zr d states. Therefore, it has been suggested to continuously tune the energy bandgap for specifical optical applications, by changing the Ti concentrations in solid-solution MXene $Hf_{2-2x}Ti_{2x}CO_2$ ($0 \le x \le 1$) (**Fig. 7**c) [157]. A 2D topological insulator (TI) with large band gap is an ideal platform for realizing the topological superconductivity and Majorana modes through proximity effect [158]. MXenes consist of heavy elements that normally feature a strong spin-orbit coupling which may significantly modify the electronic structure and forms a topological insulating phase [159-161]. Indeed, most of the reported topological insulating MXenes consist of heavy metals like Mo, W, Ti, Zr, and Hf atoms. For instance, transition metal nitride (TMNs) $Ti_3N_2F_2$ is predicted to be a 2D TI due to the strong spin-orbit coupling (**Fig. 7**d).

Additionally, the optical properties of MXene materials can be altered via several other parameters, including strains [162-164], doping [165, 166], external electric field [167, 168], and the formation of heterostructures [169]. For example, it is suggested that the monolayer Sc_2CO_2 will experience an

indirect-to-direct bandgap transition as the tensile strains increase to a small value of ~2%, which promises optical engineering using strain modulation [162]. While the conversion of semiconductor to metal has been shown in Hf_2CO_2 and Zr_2CO_2 due to the overlapping of conduction and value bands under compressive strains [163]. Undoubtedly, the implementation of an external electric field will change the electron distribution near the Fermi surface and thus change the energy structures both the parallel and perpendicular to the E-field (**Fig. 7**e). The formation of Type II Mo_2CO_2/W_2CO_2 heterostructure allows the confined separation of electrons and holes in the two materials, shows a blue-shift of optical absorption, due to the interlayer charge transfer [169].

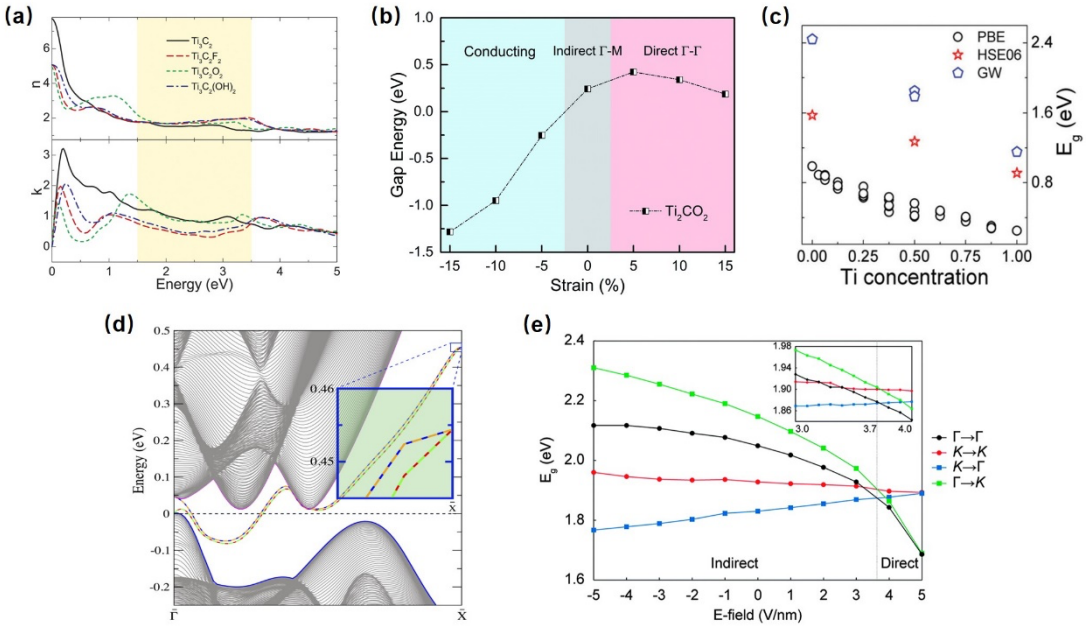

Fig. 7. (a) The dispersion spectra of refractive index (n) and extinction coefficient (k) for $Ti_3C_2T_2$ MXene [156]. (b) The bandgap energy of Ti_2CO_2 under different strains. The negative values indicate the overlap of the valence band maximum (VBM) and conduction band minimum (CBM). Adapted from Ref. [164] Copyright 2017 (c) Band gap of monolayer solid-solution $Hf_{2-2x}Ti_{2x}CO_2$ MXene as functions of Ti concentration. Adapted from Ref. [157] Copyright 2017. (d) The edge states of $Ti_3N_2F_2$ cut along the a axis [170]. (e) Change in the energy gaps as a function of the E-field. Adapted from. [167] Copyright 2017.

4.1. Optical absorption

Experimentally, the linear optical absorption of MXene films, mostly $Ti_3C_2T_x$, has been widely characterized from UV to mid-infrared regimes. Intrinsically, the optical absorption shows a thickness-dependent nature with three characteristic absorption bands: (i) the UV regime below the wavelength of ~230 nm (~5.3 eV), (ii) the 800 nm wavelength band, and (iii) the near-infrared

regime with a wavelength longer than ~1100 nm. The first two absorption bands originate from the interband transitions, while the absorption in the near-infrared stems from the plasmonics where the Real part of epsilon falls below zero (see **Fig. 8**d) [147, 171, 172]. Monolayer graphene shows 2.3% optical attenuation due to the Dirac-cone like energy structure [173], while transition metal dichalcogenides (e.g. MoS_2, WSe_2) absorb 3~10% of the visible light due to the existence of intrinsic absorption peaks [174]. However, MXenes have been demonstrated to show a higher optical transmittance over reduced graphene oxide (rGO) in the visible regime, suggesting the promising use in transparent optoelectronics (**Fig. 8**a-b) [175, 176]. Furthermore, the optical transmission of the $Ti_3C_2T_x$ thin films can be further increased by intercalation of cations between the negatively charged $Ti_3C_2T_x$ layers (see **Fig. 8**c), which was tentatively attributed to the increase of c-lattice parameter of $Ti_3C_2T_x$ layers [175]. Remarkably, a spin-coated $Ti_3C_2T_x$ MXene film with a high optical transmittance of 98% for the visible light has been demonstrated for the use of flexible and conductive high volumetric capacitors (**Fig. 8**f) [177]. Stacking layer independent, giant optical absorption and extinction coefficients are predicted in the terahertz range in Ti_3C_2 by means of systematic density functional theory (DFT) calculations (**Fig. 8**e) [178]. Following that, a 2 mm thick highly porous sponge foam comprising $Ti_3C_2T_x$ MXene has recently been demonstrated to show >99.99% broadband absorption of THz source (0.3 to 1.65 THz) [179].

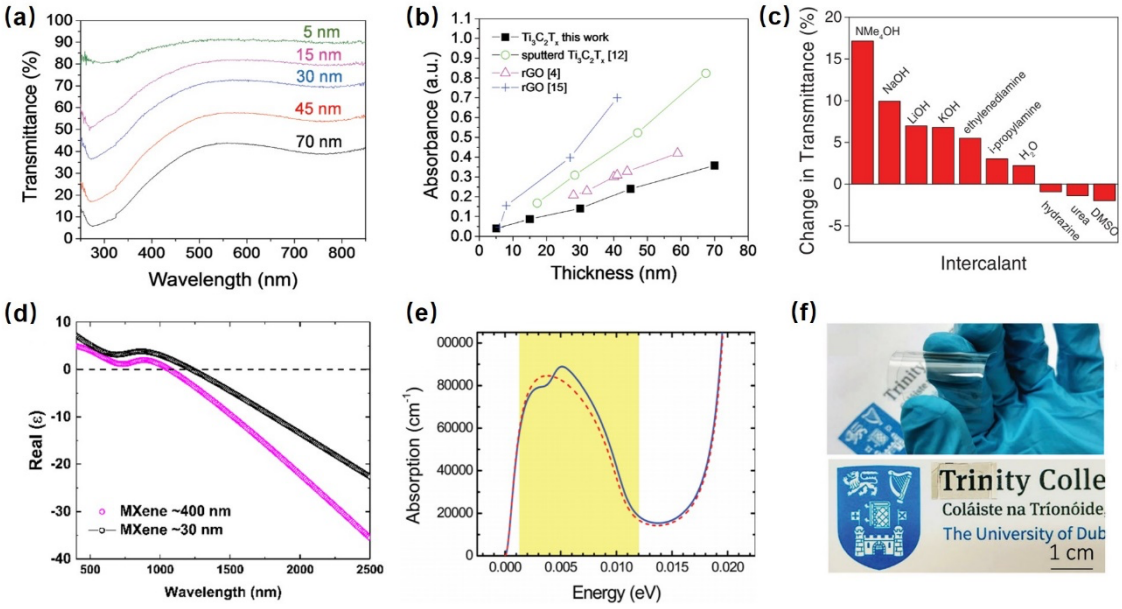

Fig. 8. (a) Linear optical absorption spectra of spin-coated $Ti_3C_2T_x$ films with different thicknesses [175]. (b) Thickness dependent absorbance of $Ti_3C_2T_x$ films compared with reduced graphene oxide (rGO) [175]. (c) Change of transmittance of $Ti_3C_2T_x$ films via different intercalation methods, positive change means increase in transmittance compared to pristine films [175]. (d) Real component of permittivity (ε) of $Ti_3C_2T_x$ films with a thickness of 30 and 400 nm [172]. (e)

Theoretically calculated optical absorption spectrum of monolayer Ti_3C_2. The yellowish shaded regions indicate the THz range. Adapted from Ref. [178] Copyright 2017. (f) Images of flexible, transparent $Ti_3C_2T_x$ film on a PET substrate and symmetric solid-state supercapacitors [177].

4.2. Photon emission

There is no semiconductive MXene bulk materials that have shown the evidence of photoluminescence (PL), the current reports are all from the MXene nanosheets or quantum dots (QDs) due to the bandgap breaking as particle size are being reduced. Three absorption peaks at 260, 310, and 350 nm are normally observed in MXene QDs and the emission spectrum covers 400 to 600 nm [180]. These absorption and emission bands may experience shifts up on particle sizes and chemical compositions. The PL properties of MXenes are found to be sensitive to the temperature, pH values, solvents, and diverse ions in circumstance, thus can be used as the corresponding optical-based sensors, labels, and in imaging [180-182]. Excitation wavelength depended emission spectrum shift is observed in $Ti_4N_3T_x$ MXene, and this shift is ascribed to the defects in $Ti_4N_3T_x$ due to surface oxidation (see **Fig. 9**d) [183]. Two-photon emission is observed by using a 800 femtosecond laser excitation source in Ti_3C_2 MXene QDs [184]. The emission spectra show a white light emission feature that continuously cover 350 to 750 nm, insensitive to extra high-pressure compress (**Fig. 9**b). By using nitrogen-doped Ti_3C_2 QDs as a selective Fe^{3+} probe among 12 ion species, the detection limit can be pushed to 100 μm [180]. While the emission lifetime is normally detected to be a few nanoseconds (4~7 ns), the determined quantum yield of emission varies from < 2% to larger than 18%. The highest quantum yield was realized in nitrogen-doped Ti_3C_2 quantum dots being synthesized by thermal treatment of Ti_3C_2 quantum dots and ethanediamine in an autoclave at 160 °C for 12 h [180]. Giving the high quantum yield and moderate emission lifetime, it is revealed that MXene QDs can be an efficient random laser or amplifier gain media. Ammonia passivated V_2C MXene QDs have been used for the generation of "white" random laser operation, under a high excitation fluence of 4.8 mJ/cm^2 at 355 nm [185]. Undoubtedly, the laser threshold can be further reduced by increasing the concentration of QDs, or mixing nanoparticles (e.g. Au nanoparticles) in the solution to enhance the scattering and plasmonics process. The highly efficient electrochemiluminescence (ECL) performance of $Ti_3C_2T_x$ MXene QDs has been demonstrated, which can be a powerful probe for the biological and environmental diagnostics [186, 187]. The fluorescence resonance energy transfer (FRET) between Cy3 and MXene has also been observed [188, 189], that enables the application for ratiometric detecting and ultra-high resolution biomedical imaging. Amphiphilic carbide-derived graphene quantum dots (GQDs) that can be well dispersed in both hydrophilic and hydrophobic solvents have been synthesized by means of solvothermal treatment of $Ti_3C_2T_x$ MXene in dimethylformamide (DMF) [190]. The carbide-derived GQDs can find applications in the field of fluorescent ink, light-emitting composites and cellular imaging, as shown in **Fig. 9**a-b. MXene-integrated photonic crystal (PhC) array has been prepared for multichannel

bioinformation coding [191]. Due to the fluorescence resonance energy transfer (FRET), the fluorescence signal of closer DNA probes can be quenched by MXene nanosheets. However, when the corresponding target is present, the fluorophore can be kept away from MXene and emit the fluorescence signal. Therefore, the complex sequence information of DNA can be converted into visualized fluorescence signals for detecting (see **Fig. 9**e-f).

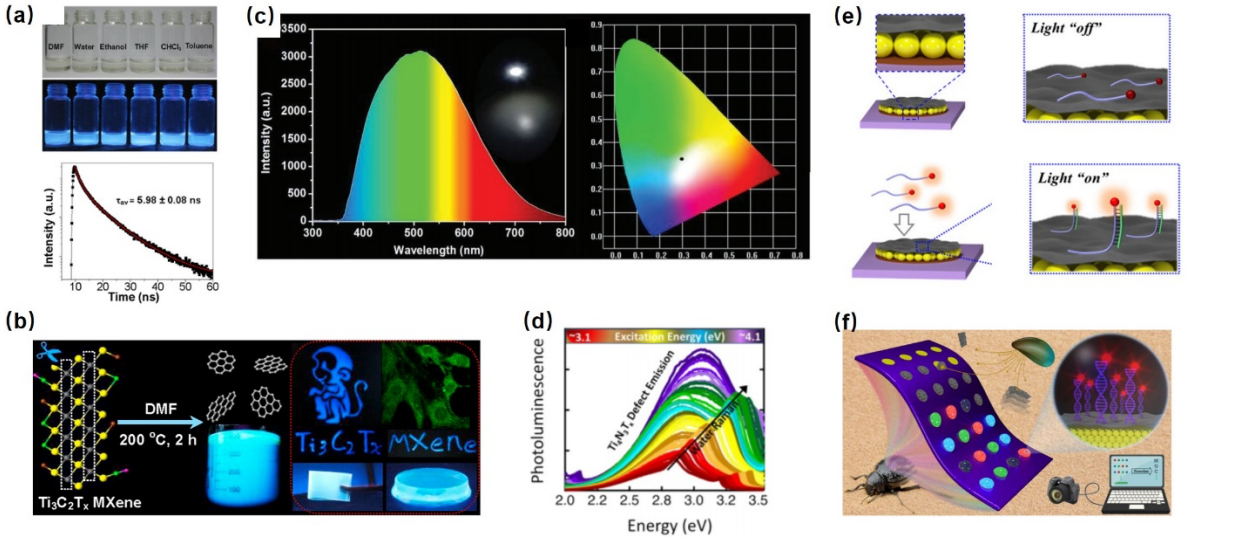

Fig. 9. (a) The images of GQDs in various solvents under daylight and 365 nm UV lamp, and a typical fluorescence lifetime decay curve of GQDs tested at 405 nm under the excitation of 322 nm [190]. (b) A schematic shows the MXene derived GQDs for fluorescent ink and cellular imaging [190]. (c) Emission spectrum of Ti_3C_2 MXene QDs shows a white light feature (right), and the corresponding CIE chromaticity diagram (0.30, 0.34) (left) [184]. (d) Photoluminescence intensity shifts of exfoliated $Ti_4N_3T_x$ MXene in water as the excitation energy varies from ~4.1 to ~3.1 eV [183]. (e) Schematic illustration of the MXene-integrated PhC arrays, and the fluorescence signal from "off" to "on" when the target is present [191]. Copyright (2020) National Academy of Sciences (f) Schematic illustration of bioinspired MXene-integrated colloidal crystal arrays for multichannel bioinformation coding [191]. Copyright (2020) National Academy of Sciences

4.3. Nonlinear optics

As the intensity of illumination light increases, multiple nonlinear optical responses have been achieved in MXenes. Saturable absorption depicts the negative third-order of dielectric susceptibility ($\chi^{(3)}$) has been characterized using a Z-scan approach (see **Fig. 10**a). Jiang *et al.* [192] found broadband saturable absorption responses from 800 to 1800 nm can be observed in $Ti_3C_2T_x$ nanosheets. The determined modulation depth can be as high as 40%, which can be applied for efficient passive optical switching. They also noticed that the nonlinear optical absorption may increase as the incident laser intensity, indicating the emergence of multi-

photon absorption processes. Indeed, reverse saturable absorption (RSA) behavior has been recently observed, which is ascribed to the two-photon absorption in $Ti_3C_2T_x$ MXene nanosheets (**Fig. 10**e-f) [193]. Similar to graphene, the fast recovery time of MXene is detected, varies from < 1 ps to a few pico-seconds covering visible to terahertz region (**Fig. 10**g) [193-195]. The broadband saturable absorption and fast recovery time of MXene can be utilized to ultrafast laser generations. Carefully adjust the rheological properties of MXene ink, diverse MXene thin film patterns have been inkjet-printed on side-polished fibers, gold mirrors and silica glass, which can be integrated with fiber or solid state resonators (**Fig. 10**h) [196]. The operation wavelengths cover near-infrared to mid-infrared regimes with pulse duration going down to ~100 femtoseconds. Combining the RSA of C_{60} and SA of MXene, an integrated $Ti_3C_2T_x/C_{60}$ device has shown non-reciprocal optical transmission properties, that can be used as a photonic diode (**Fig. 10**b) [197]. The nonreciprocity factor for these devices can be achieved to 4.13 dB as the MXene film thickness goes up to 100 nm. Taking advantage of the large third-order optical nonlinearities of MXene, a fiber-based four-wave-mixing with a high modulation speed of 10 GHz has been realized, suggests the potential application of integrated all-light signal modulations (**Fig. 10**c-d) [198].

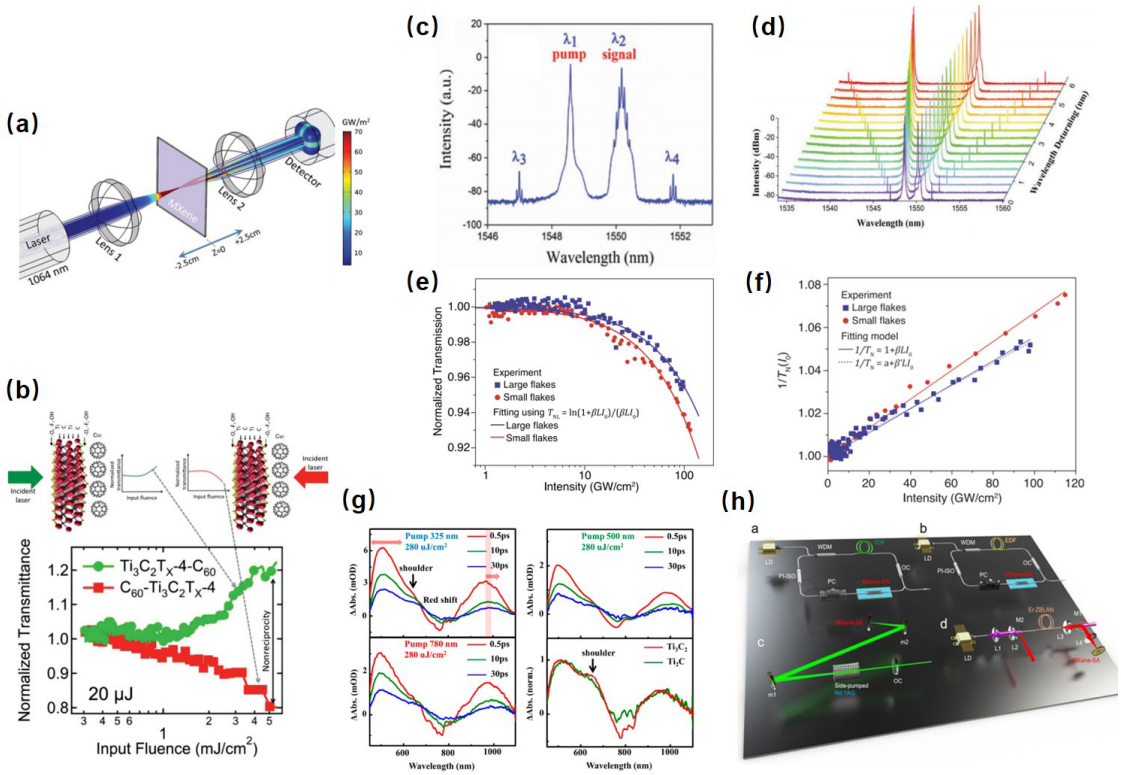

Fig. 10. (a) Schematical illustration of z-scan characterization [197]. (b) Integrated $Ti_3C_2T_x$-MXene/C_{60} optical diode shows forward and reverse bias optical transmission [197]. (c) Optical spectrum of wavelength conversion using a MXene-decorated microfiber [198]. (d) Four-wave

mixing effect for different wavelength spacing and pump powers [198]. (e) Normalized optical transmission of MXene monolayers changes as the incident intensity shows a reverse saturable absorption behavior [193]. (f) The inverted normalized optical transmission of the MXene monolayers as a function of incident intensity [193]. (g) Transient absorption spectra of MXene in solution with various pump wavelengths and intensities [194]. (h) Schematic diagrams of four laser resonators using inkjet-printed MXene saturable absorbers for pulsed laser generations [196].

4.4. Plasmonics

Plasmons are quasiparticles that describe collective electron oscillations under the drive of the incident light, and can be deployed for broad applications ranging from biomedical sensing to enhanced light absorption or harvesting [199]. The metallic feature of MXene with large DOS at the Fermi surface suggests an excellent platform for photon-electron coupling. Combining high-resolution transmission electron energy-loss spectroscopy and *ab initio* calculations to investigate the plasmons response in Ti_3C_2, it was revealed that strong surface plasmons dominated the oscillations, and the bulk plasmons can be neglected as the MXene stacking thickness below 45 nm (see **Fig. 11**a) [200], or 45 layers assuming the thickness of monolayer to be 1 nm [201]. This domination originates from the combination of efficient free-electron dynamics, begrenzungs effect, and reduced interband damping. These characteristics are different from noble metals, in which surface plasmons vanish for thickness larger than 30 nm [202]. Therefore, surface plasmons can be significantly modified by the surface morphologies, e.g. functionalizations, defects, and thickness. Mauchamp *et al.* [200] found the surface plasmon frequency of Ti_3C_2 MXene sheets can be tuned in the mid-infrared region, from 0.2 to 0.7 eV, by adjusting the surface termination and MXene thickness. The coexistence of both edge and central longitudinal modes and transversal mode in $Ti_3C_2T_x$ flakes have been confirmed via ultra-high-resolution electron energy-loss spectroscopy (EELS) [171]. However, different from the transverse mode and interband transition, the longitudinal modes exhibited high sensitivity to the surface morphologies and MXene thickness. Taking leverage of the strong surface plasmonic oscillations, an enhancement factor of 10^6 have been demonstrated in a MXene-based surface-enhanced Raman spectroscopy (SERS) for the detecting of rhodamine 6G, methylene blue, crystal violet, and acid blue [203]. A metasurface comprising a $Ti_3C_2T_x$ nanodisk array on an Au/Al_2O_3 substrate was fabricated that exhibit a high optical absorption (~90%) overing 1.55 μm from visible to near-infrared, which suggested the applications of light energy harvesting, biomedical imaging, and sensing (**Fig. 11**b) [172]. Metallic TiN and ZrN has been used to construct a one-dimensional photon spin Hall metasurface, in which the incident light can be separated based on circular polarizations and optical frequencies [204].

Utilizing the surface plasmons induced hot carriers, Mo_2CT_x MXene thin films that deposited on paper substrates have shown broadband photodetecting characteristic in the visible frequencies (400-800 nm) with high responsivity (up to 9 A/W) and sensitivity (~5×10^{11} Jones) (see **Fig. 11**f)

[205]. A MXene-based Kretschmann configuration surface plasmon resonance (SPR) sensor has been proposed and awaits for experimental confirmations (**Fig. 11**c) [206, 207].

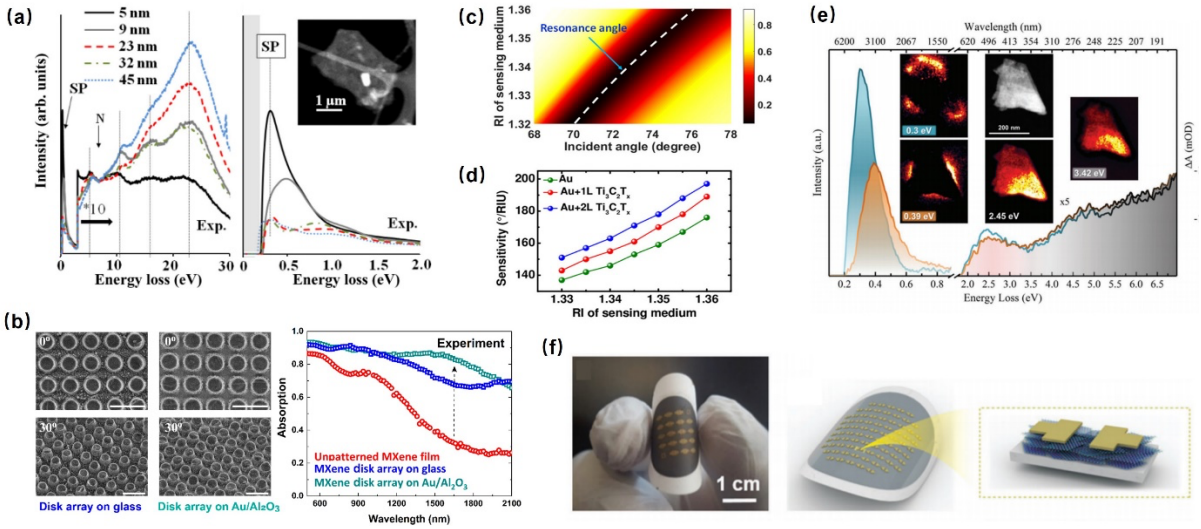

Fig. 11. (a) Experimental energy loss spectra recorded for $Ti_3C_2T_2$ with different thicknesses (right). Detailed spectra of the low energy surface plasmon (left) [200]. (b) SEM images of MXene disk array on glass and Au/alumina substrates (right). Measured absorption spectra of the two types of disk arrays and unpatterned MXene film [172]. (c) Resonance angle as a function of the incident angle for the proposed Au-$Ti_3C_2T_x$ SPR biosensor [206]. (d) The sensitivity of the Au-based biosensor with different layers of Ti3C2Tx changes as the refractive index of sensing medium [206]. (e) EEL spectra acquired on a truncated triangular nanosheet of Mo_2CT_x (≈58 nm±1 at the center). Insets: annular dark field-STEM micrograph of the Mo_2CT_x nanosheet on a Si_3N_4 supporting membrane (black area), and the EEL intensity maps of the corresponding longitudinal SP modes [205]. (f) Photograph and schematic illustration of an array of two-terminal, parallel-type thin film Mo_2CT_x-based flexible photodetectors [205].

4.5. Photothermal conversion

As discussed previously, MXene materials absorb light via interband transition in the UV and visible frequencies, while absorbing light energy via plasmonics at a lower photon energy regime. Therefore, the photothermal effects highly depend on the incident light parameters (e.g. wavelength, pulse duration, intensity), the material morphologies, device configurations (e.g. metamaterial substrates), and environments (e.g. pH value, temperature, solvents, metamaterial substrates). Generally, the photothermal conversion mechanisms can be categorized into three types: i) localized surface plasmon resonance (LSPR) effect, ii) electron–hole generation and relaxation, and iii) conjugation or hyperconjugation effect [208, 209]. Additionally, the characterizations of experimental photothermal efficiency can be significantly influenced by the phonon dissipation properties and environments. Yet, the photothermal conversion processes and mechanisms in MXene materials remain elusive [210].

Recently, bio-compatible MXenes have found wide applications for medical treats, such as photothermal therapy (PTT) for tumor ablations, and along with photoacoustic imaging, photodynamic treatment (PDT), photo-controlled drug release for synergistic treatments [211-214] (see **Fig. 12**). The photothermal induced local solution evaporation can be used for fast reversible nanofluidic transport controlling on the time scale of 0.34s [215]. Self-healable, wearable and transparent photothermal device has been demonstrated by using MXene nanosheets and silver nanoparticles as the photothermal convertor [216]. The self-healing of the composite coating can be achieved via the local temperature increase that can cure the mechanical damages. Smart light-driven object motions in water have been demonstrated using a superhydrophobic MXene flakes with a high photothermal conversion [217] (see **Fig. 12**d). The impetus of the motion originates from the local thermal effects induced recoil force. Therefore, the object motion can be highly controllable by adjusting the laser irradiation position and the object structures. Vertically aligned Janus MXene aerogel with hydrophobic upper layer and hydrophilic bottom layer has been designed and fabricated [218]. This Janus structure forms pump channels for the water transport and promote the evaporate rate upon light irradiations (**Fig. 12**e). All light signal manipulation has also been realized by decorating MXene nanosheets on one-arm of a Michelson interferometer (**Fig. 12**f-g). The achieved modulation depth is up to 27 dB with a free spectrum range of 16.8 nm and phase shift slope of 0.043 π/mW [219].

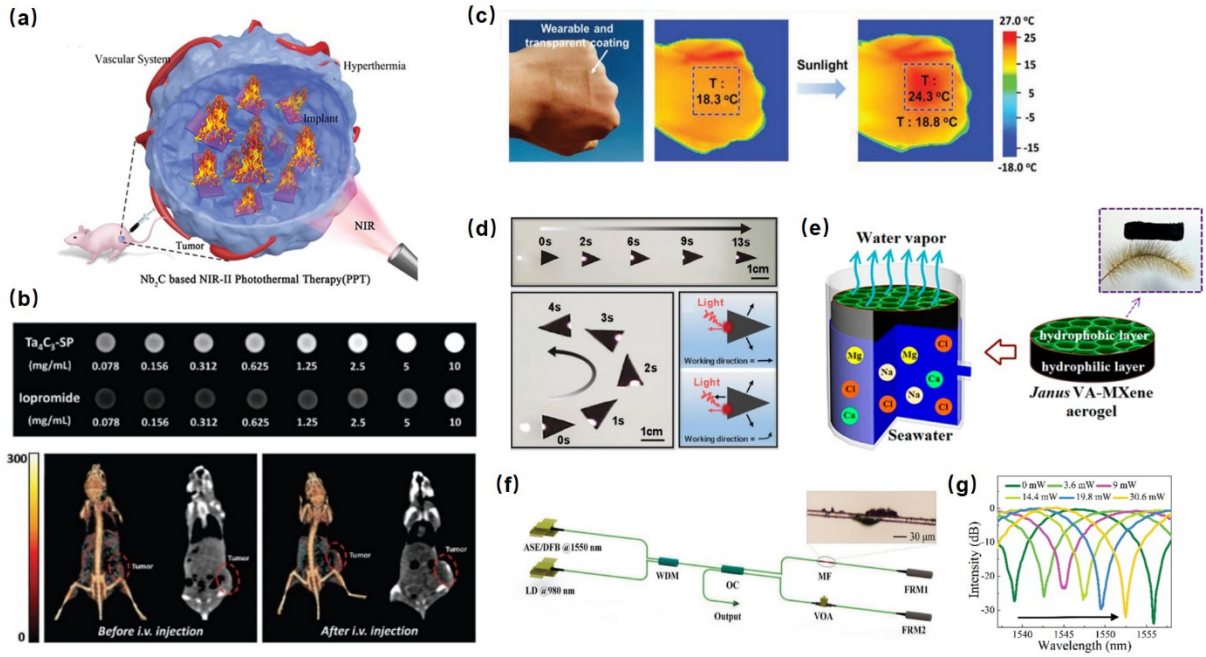

Fig. 12. (a) Schematic illustration of the *in-situ* formation of Nb_2C/zein bio-implant for photothermal tumor ablation. Adapted from Ref. [212] Copyright 2017. (b) *in-vitro* and *in-vivo* photoacoustic image over time using Ta_4C_3 nanosheets as the agent [213]. (c) Photograph of a ~100 μm thick 0.08 wt.% AgNP@MXene-PU composite transparent film attached on a hand. Left

shows the IR thermal images of the hand with the film before and after solar irradiation for 1 min [216]. (d) The trajectories of a light-driven a MXene coated filter paper. Adapted from Ref. [217] Copyright 2017. (e) Schematic illustration of a high-efficiency solar steam generation system using a Janus MXene film [218]. (f) Experimental diagram of a Michaelson all-optical modulator with one arm decorated with MXene nanosheets. and (g) the interferometric fringings as a function of pump power [219].

4.6. Photodetection

Compared to other 2D materials, the reports on 2D MXene-based photodetectors are few and far between [220]. Yet, the progress over the past decade is nontrivial, and MXene-based photoconductors [221], self-driven photodetectors [222], and plasmon enhanced photodetectors [205], have been explored. Since the work-function of MXenes can be adjusted via the modification of surface terminations and chemical compositions, it is possible to fabricate MXene-based photodetectors in large scale. Deposition of $Ti_3C_2T_x$ on the n-type silicon (n-Si) substrate forms a vertical van der Waals heterostructures, where $Ti_3C_2T_x$ has a work function of 4.37 eV, and can form a good Schottky contact with n-Si at room temperature (**Fig. 13**a-c) [222]. The photo-generated carries can be efficiently separated and transported through the transparent $Ti_3C_2T_x$ electrode. An open circuit voltage of 0.34 V and a short circuit current density of 12.9 mA/cm^2 can be obtained in the $Ti_3C_2T_x$/n-Si Schottky junction under 100 mW/cm^2 irradiation. More importantly, the $Ti_3C_2T_x$/n-Si photodetector is a self-driven one that can realize a I_{ph}/I_{dark} ratio of 10^5 and responsivity of 26.95 mA/W (**Fig. 13**d-g). MXene has been investigated as the transparent electrodes for metal–semiconductor–metal (MSM) photodetectors [223]. Spin-coating $Ti_3C_2T_x$ on III–V semiconductor GaAs realize a $Ti_3C_2T_x$-GaAs-$Ti_3C_2T_x$ (MX-S-MX) photodetector, which outperformed the standard Au-GaAs-Au photodetectors with higher responsivities and quantum efficiencies in the VIS–NIR spectral range. Thanks to the large bandgap of TiO_2, the *in-situ* formed $Ti_3C_2T_x/TiO_2$ composites show a significant photoresponse in the UV regime, yet imperceptible photocurrent has been characterized in the visible frequencies [224]. Furthermore, the parameters of photoresponse are highly sensitive to the environment, thus can be used as both UV light and humidity sensors. Integrating MXene with perovskite that take advantage of the large absorption of perovskite, high conductivity of MXene, economical solution-processing of both materials, low-cost, large-area, and flexible photodetectors can be achieved (see **Fig. 13**h-j) [225-227]. The spectral response range covers X-ray and visible frequencies. A highly sensitive photodetector for broadband frequencies is recently fabricated consisting of CVD grown molybdenum carbide (Mo_2C) and molybdenum disulfide (MoS_2) (**Fig. 13**k-n) [228]. The up-layer metallic Mo_2C is grating patterned, thus producing plasmonic resonances and providing hot carriers to the bottom MoS_2 channel. The low Schottky barrier between MoS_2 and Mo_2C significantly enhanced the inter-junction hot-carrier transfer efficiency. By adjusting the grating period of Mo_2C (400–1000 nm), a high responsivity ($R > 10^3$ A /W) and light-to-dark current ratio

(>10^2) from visible to NIR (405–1310 nm) can be achieved in these photodetectors. Other optical related properties and applications of MXene include efficient electromagnetic interference (EMI) shielding and absorption [229, 230], and solar cells [231, 232].

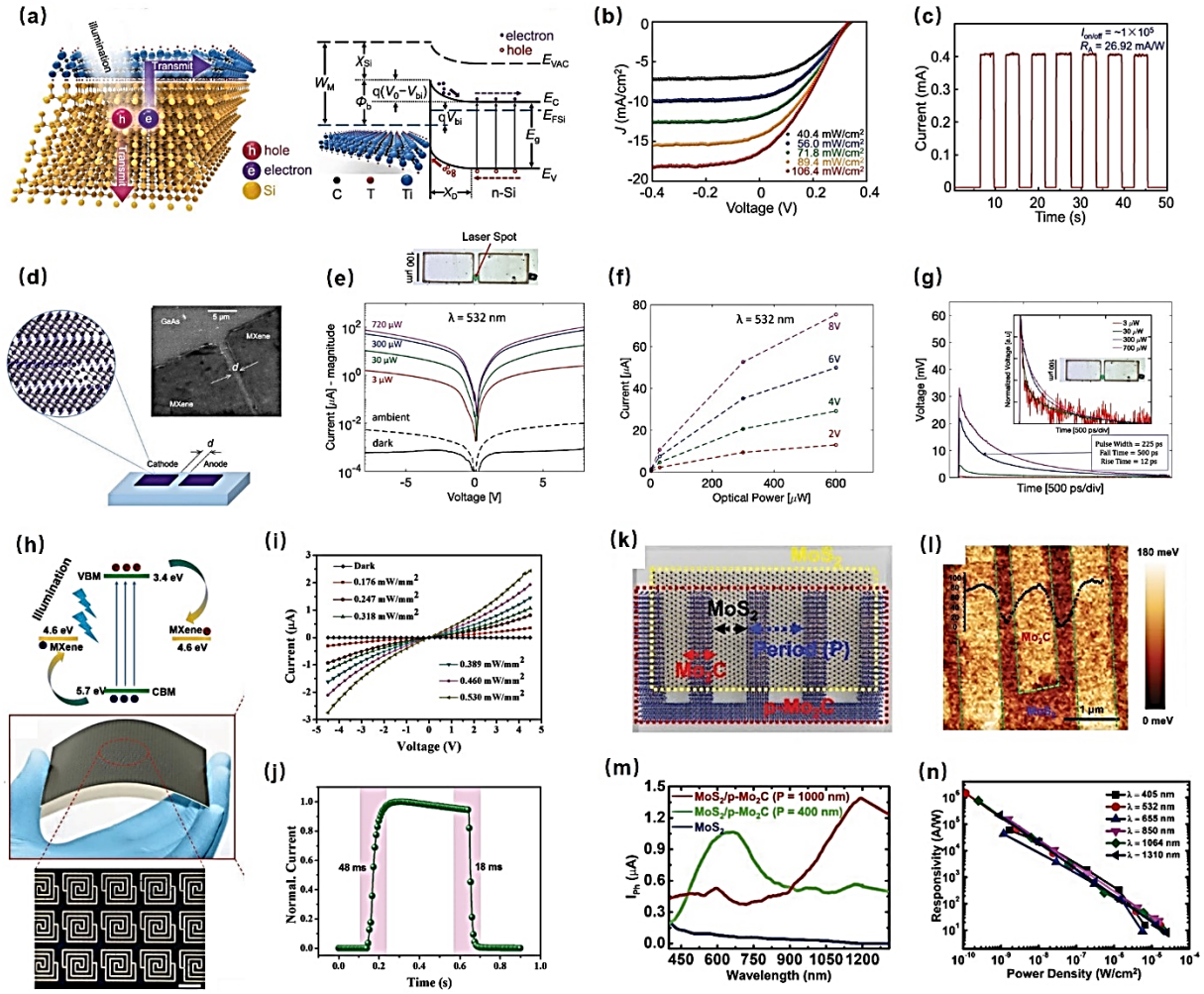

Fig. 13. (a-c) MXene-silicon heterostructures for self-driven photodetecting [222]. (a) Schematic illustration of $Ti_3C_2T_x$/n-Si heterostructure, and the corresponding energy band diagram. (b) J–V curves for the $Ti_3C_2T_x$/n-Si heterostructure device under various light intensity illuminations. (c) A typical photoresponse of the $Ti_3C_2T_x$/n-Si heterostructure device. (d-g) Spin-coated Ti_3C_2-based MXene photodetectors [223]. (d) Structure and SEM (inset) images of the spin-coated MXene photodetector. (e) Microscopy image of the fabricated MX-S-MX photodetector, and current–voltage responses of the MX–S–MX to 532 nm light illumination. (f) Photocurrent of the MX-S-MX detector under various optical intensities at 532 nm and at different biases. (g) Temporal response of MX-S-MX detector to excitation of 100 fs, 830 nm light at 8 V bias under various incident intensities. Inset shows the normalized spectra. (h-j) Flexible MXene/perovskite-based photodetector arrays [225]. (h) Energy level diagram of MXene/perovskite electrode. And the

images of the large-area MXene electrode arrays. (i) Typical I-V curves of the photodetectors response to a 405 nm light irradiation with varies intensities. (j) Normalized high-resolution temporal photoresponses. (k-n) MXene-based multiperiod grating for broad-spectrum photodetection [228]. (k) Schematical illustration of MoS_2/p-Mo_2C hybrid grating structure. (l) $\Delta\Phi$ mapping image of MoS_2/p-Mo_2C grating structure and line profile curve. (m) Spectral photoresponse of MoS_2/p-Mo_2C hybrid structure with different grating period, compared to pure MoS_2 photodetector. (n) Responsivity of the MoS_2/p-Mo_2C hybrid device at different wavelengths as a function of illumination intensities.

5. Magnetic features

Compared to other properties of MXenes, the magnetic properties are less investigated due to the intrinsic lack of ferromagnetic ordering in 2D materials. Nevertheless, a great number of theorical predictions have revealed the potential magnetism in the multifunctional MXenes. In this section, we comprehensively review the theoretical analysis for the exploration of excellent magnetic performance in MXenes, thanks to their richness of stoichiometry and surface function groups. Besides, the influence of doping, defects, external fields (e.g. strains and E-field) on magnetism in MXenes are thoroughly discussed. Since the experimental validations are limited, a short summary of current research progress, as well as a perspective are also presented.

5.1 Theory predictions

According to the Mermin–Wagner theorem, there is no long-range ordering in two-dimensional materials above zero temperature with continuous spin symmetry for the realization of magnets [233]. Therefore, most of the presented 2D materials are nonmagnetic. Recently, the demonstration of ferromagnetic ordering in ultrathin CrI_3, $Cr_2Ge_2Te_6$, and Fe_3GeTe_2 has invigorated the search for novel 2D magnets due to their promising applications in spintronics, quantum computation, as well as logic and memory devices [234-237]. The necessity to achieve 2D magnets is the exploration of systems with large magnetic anisotropy to break the symmetry of Heisenberg moments [238]. Varies calculation methods have been carried out to screen the magnetical properties of MXenes. Thanks to the large tunability of crystal structures, chemical components, and surface terminations, it has been revealed that the realization of magnetic anisotropy in MXenes can be expected. Generally, the magnetism in MXene originates from the itinerate electron of transition metals, surface terminations, lattice defects, doping, and external fields (e.g. mechanical strains and E-field).

Half-metals and spin gapless semiconductors are promising candidates for the spintronic applications due to the complete (100%) spin polarization of electrons around the Fermi level, as shown in **Fig. 14**a [239]. Most of the predicted magnetic MXenes normally contain magnetic transition metal elements, e.g. Fe, Co, and Ni Cr, V, Mn, and Mo. Pristine Cr_2C is found to be ferromagnetism due to the itinerant d electrons of Cr, which results in an intrinsic half-metallic

configuration with a half-metallic gap of 2.85 eV [25]. However, the itinerant electrons can be localized by the surface terminations F, OH, H, or Cl groups, leading to the ferromagnetic (FM) to antiferromagnetic (AFM) and accompanied metal to insulator transitions. However, functionalized Cr_2CF_2, $Cr_2C(OH)_2$, Cr_2NF_2 , $Cr_2N(OH)_2$, and Cr_2NO_2 are found to be magnetic at low temperatures using first-principles calculations, among carbides M_2C (M = Sc, Ti, V, Cr, Zr, Nb, Ta) and nitrides M_2N (M = Ti, Cr, Zr) [240]. Fluoride terminated MXene Mn_2CF_2 is isolated to be ferromagnetic with intrinsic half-metal configuration and high Curie temperature, compared to other surface terminations (Cl, OH, O, and H). [241], wherein magnetic property mainly originates from Mn^{3+} atoms. Similarly, $Mo_3N_2F_2$ is suggested to be half-metallic ferrimagnet, due to the itinerant d electrons of Mo layers [242]. Monolayer Fe_2C is found to feature an intrinsic metallic ferromagnetic ground state with a high Curie temperature of 861 K. Besides, large magnetic anisotropy energy (MAE) is determined to be -22.8 μeV per unit cell in Fe_2C, allows the potential use in magnetic storage [243]. Out of 319 i-MXenes that with the formula of $(M_{2/3}M'_{1/3})_2X$, where M is substituted with a 1/3 different transition metal, most of them are non-magnetic (257) and the remaining 62 compounds are found show magnetic moments greater than 0.2 μ_B/f.u. in the ferromagnetic spin configuration [244]. Besides, there are 15 i-MXenes with AFM intralayer exchange coupling between the moments on the M′ sites, suggesting possible 2D noncollinear magnetic states. Achieving multiferroics in the same phase of a 2D material enables numerous functionalities in nanoscale devices [245, 246]. Room-temperature stable, tightly coupled type-II multiferroic is predicted in monolayer $Hf_2VC_2F_2$. [247]. The ferroelectricity originates from the noncollinear 120° Y-type spin order that generates a polarization order perpendicular to the spin helical plane, as shown in **Fig. 14**c.

Compared to TMCs, TMNs contain an extra electron are expected to have robust ferromagnetic ground states due to the excess density of states at the Fermi level. Nitride MXene Mn_2NT_x (T = O, OH, and F), Ti_2NO_2 and Cr_2NO_2 are calculated to be half-metallic ferromagnets with high magnetic moments and Curie temperatures [248]. The magnetic feature originates from the nonbonding d-orbitals of transition metals that are located between bonding (σ) and antibonding (σ*) states of M-X and M-T bonds. In the equilibrium structure, each transition-metal ion is subjected to an octahedral crystal field from the nearest-neighbor N and T (O, OH, F) atoms/groups, thus further splits the d-orbitals into the lower energy t_{2g} (d_{xy}, d_{yz}, and d_{xz}) states and higher energy e_g ($d_{x^2-y^2}$ and d_{z^2}), as shown in **Fig. 14**b.

It is found that surface termination can induce a change from continuous spin symmetry in an XY ferromagnet to anisotropic Ising ferromagnetism, and increasing the atomic number of the transition metal leads to a similarly pronounced transition from a continuous Heisenberg magnet to Ising ferromagnetism, as shown in **Fig. 14**d [249]. For instance, Ti_2NO_2 and Mn_2NF_2 MXenes have continuous spin symmetries, while Cr_2NO_2 and Mn_2NO_2 are intrinsic Ising ferromagnets. Bare Cr_2N is identified as an antiferromagnetic metal, while the oxygen passivated Cr_2NO_2 is half-metallic ferromagnetic [250].

Ti-based M_2X MXene was found to exhibit nearly half-metallic ferromagnetism and can be turned to truly half-metal under small biaxial strains. While V-based M_2X is intrinsic nonmagnetic, and induce large magnetic moments via suitable biaxial strain [251]. The influence of extensile strain on the magnetic properties of Cr-based MXenes ($Cr_2M_2C_3T_2$, M=Ti, V, Nb and Ta) are systematically investigated using density functional theory [252]. The ground state of $Cr_2Ti_2C_3O_2$ and $Cr_2V_2C_3O_2$ is energetically favorable for ferromagnetic architectures, while the other MXenes are anti-ferromagnetic. However, FM to AFM (or AFM to FM) phase transition can be realized in all the Cr-based MXenes by applying an extensive strain of less than 5%. The influence of biaxial strains on non-terminated M_2C (M=Hf, Nb, Sc, Ta, Ti, V, Zr) is analyzed via density functional theory [253]. It is revealed that all these MXenes exhibit no intrinsic magnetism at the strain-free state, except for Ti_2C and Zr_2C which show a magnetic moment of 1.92 and 1.25 μ_B/unit, respectively.

The magnetic moments of these MXenes can be significantly enhanced as the tensile strain increases, leading to a nonmagnetic to ferromagnetism transition (see **Fig. 14**f). Among all the systems, Hf_2C stands for the most dramatic transition from near zero to 1.5 μ_B/unit at a strain of 1.8%. MXene Cr_3C_2 is an intrinsic robust ferromagnetic with a magnetic moment of 3.9 μ_B/unit [254]. This ferromagnetic coupling can also be modified by external tensile strains. As the strain rise to 3%, the Cr_3C_2 experience a metallic ferromagnet to half-metallic ferromagnet transition accompanied by the magnetic moment increase to 4.0 μ_B/unit.

Electrical control of spin polarization is much desirable in spintronics since electric fields can be easily applied locally, in contrast to magnetic fields. Bipolar magnetic semiconductors (BMSs) [255], in which completely spin-polarized currents with reversible spin polarization can be created and controlled simply by applying a gate voltage, and it identified from a mixed surface terminations MXene $Sc_2C(OH)_xO_{2-x}$, where x is in the range of $0.188 \leq x \leq 0.812$ [256]. The passivation of different terminations species on the top and bottom surfaces of $M_2XO_xF_{2-x}$ (M=Mn, Cr, Ti, V; X=C and N, x=0.5, 1, 1.5) breaks the composition and structural symmetry, leading to the formation of Janus MXene. The magnetic ordering in these systems is nonmagnetic or weakly magnetic in their pristine form [257]. However, the antiferromagnetic ground states can be robustly switched to ferromagnetic ordering and stabilized by tuning the interlayer exchange couplings with small applied electric fields (see **Fig. 14**e). Janus MXene Cr_2TiC_2FCl with F and Cl asymmetrically passivated on the two surfaces also behave as antiferromagnetic, while the applied gate voltage can manipulate the spin orientation of the antiferromagnetic Cr_2TiC_2FCl and lead to a transition from bipolar antiferromagnetic semiconductor to half-metal antiferromagnets [258].

The influence on magnetic of vacancy defects in Ti_2XT_2, (X=C, N; T=O, F, and OH) has been examined via extensive first-principles based simulations [259]. Except for single vacancies of C in Ti_2CO_2, all the other systems with C and N vacancies are magnetic due to the presence of unpaired electrons in the spin split d-orbitals. Cr and Mn-doped semiconductive Sc_2CT_2 MXenes

were found to be magnetic [260]. MXene analogies such as Zr_2Si and MnBene are predicted to show distinct magnetic properties [261, 262].

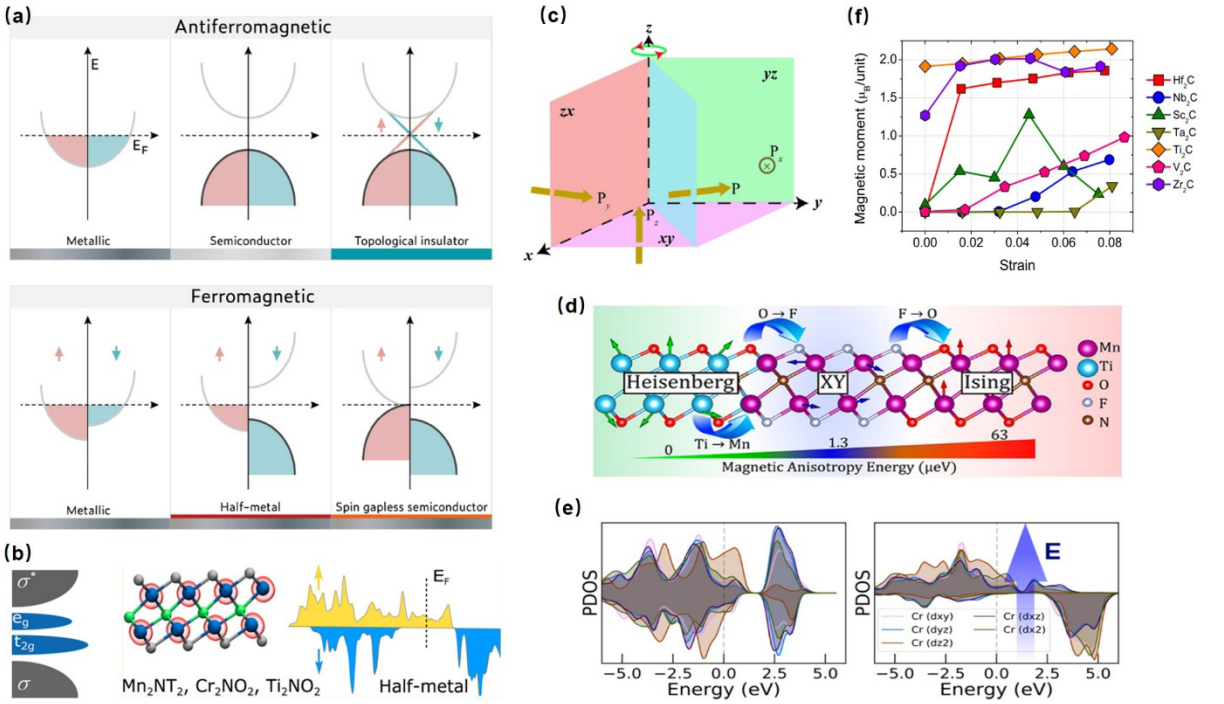

Fig. 14. (a) Schematic density of state (DOS) electronic band structure and the possible ground-state magnetic configurations [239]. (b) Schematic of d-orbitals around the Fermi level of nitride MXene Mneme inducing the half-metallic magnetism [248]. (c) Schematic of type-II helical Y-antiferromagnetic induced ferroelectric polarization [247]. (d) Tunable noncollinear spin structure and magnetic anisotropy via the alternation of transition metal elements and surface terminations [249]. (e) Electric field-induced change of density of states and magnetic anisotropy [257]. (f) Manipulation of magnetic moments by applying mechanical strains [253].

5.2 Experimental validation and applications

As discussed in the theoretical part, it is a challenge to realize significant magnetic moments in 2D materials. Although extensively studied computationally, there are only a few experimental reports that have revealed the magnetic properties in pristine MXenes. The first experimental magnetic property of MXene is observed in reduced $Ti_3C_2T_x$ MXene, which is obtained by immersing of $Ti_3C_2T_x$ in the reducing agent Li-ethylenediamine (Li-EDA) [263]. It has been found the magnetic susceptibilities (χ) are independent of temperature above 10 K, suggesting the reduced $Ti_3C_2T_x$ is Pauli paramagnetic. The magnetism was confirmed to be originated from the 2D flakes rather than the defects of TiO_2 via a Curie-like transition of χ below temperature 10 K. The influence of surface terminations species and concentration on the magnetic properties of $Ti_3C_2T_x$ MXenes have been investigated [264]. The alternation of surface termination is realized via

using different etching acid procedures during the MXene synthesis, including (1) hydrofluoric acid, (2) chlorosulfonic acid, and (3) hydrofluoric acid followed by chlorosulfonic acid. The MXenes synthesized via the previous two individual approaches only show paramagnetic behavior, while the samples prepared by the third approach exhibit two different types of radicals and/or defects in the electron paramagnetic spectrum and mixed antiferromagnetic/paramagnetic behavior under an external magnetic field of 100 Oe. The appearance of magnetic ordering was attributed to sulfur-based functional groups (-S_2 and -SO_3H) introduced by chlorosulfonic acid. Recently, $Cr_2TiC_2T_x$, an ordered double TMC MXene was synthesized via the selective etching of the Al layers from its precursor Cr_2TiAlC_2. Clear evidence of a magnetic transition in $Cr_2TiC_2T_x$ from a local-moment paramagnet to a state with a collective magnetic response is observed at approximately 30 K (T_f) (see **Fig. 15**a-c) [265]. The magnetic transition is evidenced by a divergence in zero-field-cooled (ZFC) and field-cooled (FC) dc magnetization and a maximum in the ac susceptibility. Magnetometry reveals a clear bifurcation in the macroscopic magnetization as measured under ZFC and FC conditions, along with the presence of glassy dynamics in the low-temperature state. A large negative linear magnetoresistance and a change of angular-dependent magnetoresistance behavior have been observed below T_f.

Giant magnetoresistance effect (GMR) realized in ultra-thin magnetic heterostructures, where two ferromagnetic layers sandwiched a thin conducting paramagnetic separator, can be desirable for magnetic sensors and high-density data storage. However, it is difficult to obtain a high magnetoresistance in small size devices. The recent progress in the exploration of magnetic MXenes posed to provide a feasible solution. Three types of Au–MXene–Au sandwich structures were designed and simulated, including Au-Cr_2CF_2-Au, Au-$Cr_2Ti_2C_3F_2$-Au, and Au-$Cr_2TiC_2F_2$-Au, to show high magnetoresistance [266]. The predicted magnetoresistance values are higher than 400% with 1.0 V for all the structures and are sensitive to the thickness and bandgap of the MXene materials (**Fig. 15**d). A full MXene magnetic tunneling junction (MTJ) is proposed via using half-metallic Mn_2CF_2 as the magnetic electrode and Ti_2CO_2 as the tunneling barrier [267]. The lattice mismatch and bandgap difference between these two types of MXene are negligible. The tunneling magnetoresistance ratio can reach up to 10^6 and remains higher than 10^3 under the bias voltages up to 1 V. The tunneling-based transmission acts reversely to the tunneling barrier width. The spin injection into graphene is promising for graphene spintronics that can be realized by interfacial proximity of half-metallic Cr_2C ferromagnet-graphene heterostructure (see **Fig. 15**e-f) [268]. The average spin polarization in the graphene can reach 74%, which is much larger than the graphene/magnetic metal or graphene/magnetic insulator heterostructures. The observed spin splitting comes from the interaction between C-p_z and Cr-3d states. The induced spin filtering and gap opening in graphene are sensitive to strains, thus can be used to design a strain modulated spin filter.

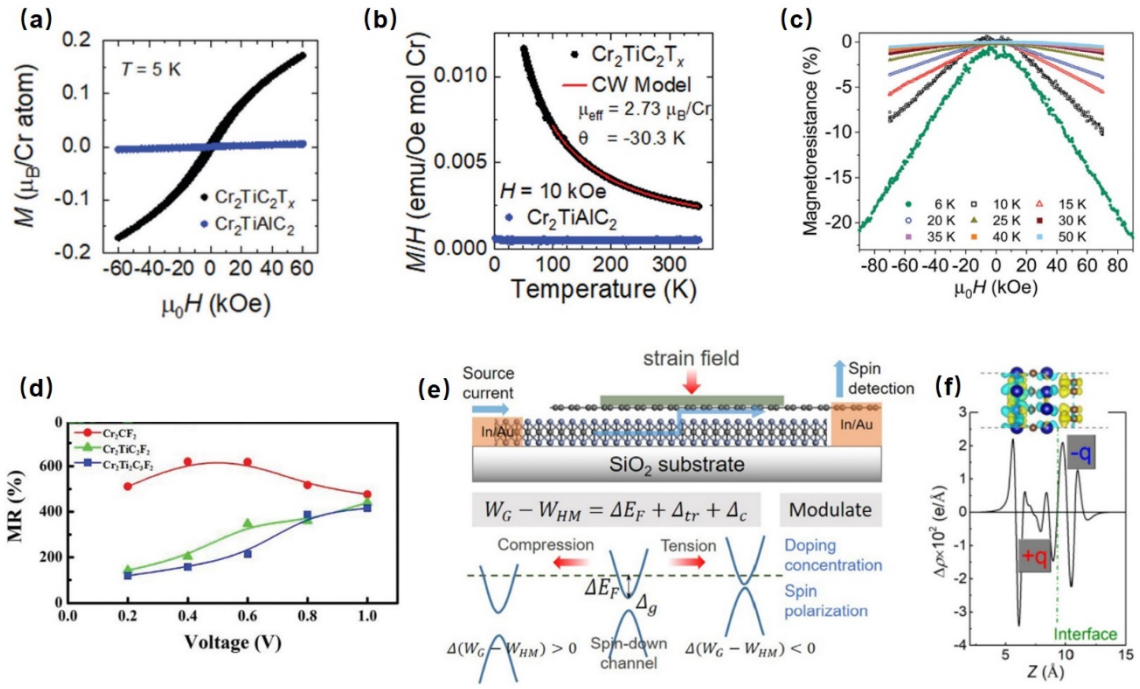

Fig. 15. (a) Field-dependent magnetization of $Cr_2TiC_2T_x$ MXene and its precursor Cr_2TiAlC_2 MAX measured at 5 K. (b) Field-cooled magnetization of $Cr_2TiC_2T_x$ MXene and Cr_2TiAlC_2 MAX measured using 10 kOe external magnetic field. (c) Field-dependent magnetoresistance of the free-standing film measured at different temperature. (a) to (c) are adapted from Ref. [265]. Copyright 2020, Royal Society of Chemistry (d) Measured MR value as a function of bias voltage for different Cr-based MXenes. Adapted from Ref. [266]. Copyright 2018, Royal Society of Chemistry (e) Schematic of proposed graphene/Cr_2C heterostructure spin filter via applying strains. (f) The plane-averaged DOS distribution along the vertical direction of the graphene/Cr_2C heterostructure. (e) and (f) are adapted from [268].

6. Electrical and energy storage

Electric vehicles (EVs) are being developed to mitigate CO_2 emissions by reducing our dependence on fossil fuels [269-271]. Unlike gasoline or diesel-based internal combustion engines that power most present-day vehicles, EVs are fully powered by the energy stored in a large onboard battery pack with projected efficiencies up to 70%. The performance of EVs ultimately hinges on the power and energy capacity of its battery pack. The automotive and electronic industries have embraced rechargeable lithium-ion battery (LIB) as "the component" for their battery packs because they provide the highest energy density of all commercially available battery chemistries [269, 272, 273]. The U.S. Advanced Battery Consortium (USABC) developed a set of goals for EV battery packs, which require that the specific energy be increased beyond 275 Wh/kg at the pack level (with a concomitant volumetric energy density of 550 Wh/l at C/3 discharge rate) at peak specific power ~700 W/kg while reducing the cost to below $75 /kWh [274].

In this section, we focus on the use of MXenes in Li-based batteries. While burgeoning applications of MXenes in batteries are described, it is worth noting that MXenes have also been widely used in supercapacitor applications and beyond Li batteries (Na+, K+), as described in other reviews. However, from EV applications standpoint, only LIBs and LSBs can deliver practical energy and power densities needed for transportation.

6.1. MXenes for Li-ion batteries (LIBs)

MXenes display wide chemical and structural variety, which makes them ideally suited for LIB anodes [275, 276]. Like graphite, in-plane bonds between M and X are very strong leading to Li+ intercalation between MXene layers. Based on density functional theory calculations, Naguib *et al.* [2] first suggested that the formation of $Ti_3C_2Li_2$ as a result of the intercalation of Li into the space vacated by the Al atoms in Ti_3C_2Tx MXenes. Despite the positive enthalpy change for such intercalation, they predicted a capacity of 320 mAh g^{-1}, which is comparable to the 372 mAh g^{-1} of graphite for LiC_6. Considering that M_2X MXenes (e.g., Ti_2C, Nb_2C, V_2C, Sc_2C) have lower formula weight than higher order MXenes (e.g., M_3X_2, M_4X_3), they are ideally suited for higher specific capacity battery electrodes. Indeed, it has been found that the gravimetric capacity of Ti_2CT_x for Li+ uptake is ~1.5 times higher than that of $Ti_3C_2T_x$ prepared in the same way [277, 278]. Unlike Ti_2CT_x, $Ti_3C_2T_x$ has an extra inactive layer of TiC that reduces the overall capacity. Similarly, V_2CT_x and Nb_2CT_x have been found to show significantly higher Li^+ capacity compared to Ti_2CT_x despite higher formula weight (280 mAh g^{-1} for V_2CT_x, 180 mAh g^{-1} for Nb_2CT_x, and 110 mAh g^{-1} of Ti_2CT_x at 1C). Theoretical investigations have revealed that the nature of T_x plays an important role in Li+ storage [279-281]. Specifically, Xie *et al.* [281] and Tang *et al.* [282] observed that oxygen terminations support a higher capacity compared to hydroxyls and fluorines that impede lithium-ion transport. In the last decade, many MXenes have been used as LIB anodes, as summarized in **Table 4**.

Table 4. MXenes in Li-ion batteries

Material	Capacity (mAh/g)	Cycle	Current density or C-rate	Year	Ref.
Nb_2CT_x	170	100	1C	2013	[283]
	110	150	10C		
V_2CT_x	260	150	1C	2013	[283]
	125	150	10C		
$Nb_4C_3T_x/C/Nb_2O_5$	192	400	50mA.g^{-1}	2016	[284]
$Ti_3C_2T_x/Co_3O_4$	540	800	640mA.g^{-1}	2016	[285]
$Hf_3C_2T_z$	146	200	200mA.g^{-1}	2017	[286]
$Ti_3C_2T_x$/PEDOT	255	100	200mA.g^{-1}	2017	[287]
$Ti_3C_2T_x/SnO_2$	810	200	100mA.g^{-1}	2018	[288]

$Ti_3C_2T_x/TiO_2$	209	200	500mA.g^{-1}	2018	[289]
$Ti_3C_2T_x$/rGO	212	1000	1000mA.g^{-1}	2018	[290]
Si/$Ti_3C_2T_x$	558	500	1C	2019	[291]
Si/$Ti_3C_2T_x$	1280	275	1500mA.g^{-1}	2019	[292]
Si/$Ti_3C_2T_x$	2118	100	200mA.g^{-1}	2019	[293]
Sandwich-like silicon/$Ti_3C_2T_x$	643.8	100	300mA.g^{-1}	2020	[294]
Co_3O_4/MXene composite	1005	300	1C	2020	[295]
SiO_2/MXene microspheres	635	200	1000mA.g^{-1}	2020	[296]

When the mechanism of lithium-ion charge storage in $Ti_3C_2T_x$ is studied using *in-situ* X-ray absorption spectroscopy (XAS), it is found that there is a continuous change in the transition metal (that is, titanium) oxidation state during charge and discharge up to 0.5 V versus Li/Li$^+$ [281]. Interestingly, a further decrease in potential does not translate into a change in oxidation state. Instead, due to the 2D nature and conductivity of MXenes, lithium atoms can reversibly form an additional layer. This provides a two-fold increase in the capacity, and this mechanism is also expected to be applicable to other MXenes [279, 297]. A further increase in capacity has been achieved by optimization of the electrode architecture, hybridizing porous MXene flakes with CNTs, resulting in a lithium-ion capacity in excess of 750 mAh g^{-1} [298].

6.2. MXenes for Li-Sulfur batteries (LSBs)

Li-S batteries (LSBs) are fundamentally different from LIBs. While LSB cathode consists of insulating sulfur (present as cyclo-S8 rings) embedded into a conducting host, a thin Li metal strip serves as the anode. In a LSB, the Li+ ions from the Li anode migrate through the electrolyte to combine with the electrons passed via the external circuit [278, 283]. The sulfur in the cathode is reduced to Li_2S (two Li+ per one sulfur), which is insulating in nature. The overall reaction in a LSB cell (S8 + 16 Li ↔ 8 Li_2S) is highly reversible with a potential of ~2.15 V versus Li/Li+. Although the voltage of LSBs is relatively lower than LIBs (3.4 - 3.8 V vs. Li/Li+), sulfur has the highest specific capacity for a solid electrode material at 1675 mAh g–1. Notwithstanding its lower voltage, a LSB cell has a theoretical energy density of 2,500 Wh kg–1 which is an order of magnitude higher than that of LIBs. Thus, LSBs are more practical for enabling a longer driving range for EVs. For surpassing traditional LIBs, the areal capacity of LSB pouch cells should be at least 5 mAh/cm2. Elemental octasulfur (cyclo-S8), which is the most stable allotrope of sulfur at room temperature, undergoes a series of structural and morphological changes during a charge–discharge cycle leading to the formation of soluble lithium polysulfides or LiPS (Li_2S_x, where $8 \leq x \leq 3$) and insoluble LiPS (Li_2S_2/Li_2S) in the liquid electrolyte. The high resistances of sulfur and the LiPS intermediates along with their structural changes result in an unstable electrochemical contact within the sulfur cathode. In addition, the dissolved LiPS shuttle between the anode and cathode during the charge process involving side

reduction reactions with the lithium anode and reoxidation reactions at the cathode (leading to a volume expansion of the cathode). Many carbon networks (graphene, reduced graphene oxide or rGO, carbon nanotubes or CNTs, activated carbon etc.) have been used both as a conductive host and a framework for trapping LiPS. Despite their success, carbon networks are non-polar and absorb high amounts of electrolytes ultimately dwarfing the overall capacity.

Compared with the nonpolar carbon-based materials, transition metal compounds exhibit strong interactions with polar LiPSs and have been shown to act as activation catalysts to facilitate oxidation of discharge product Li_2S back to charge products[32]. Building on this, as shown in **Table 5**, many researchers have used MXenes for better LSB performance. In addition to the presence of transition metals, MXene functional groups play an important role in mitigating LiPS. For example, Liang *et al*. [299] showed that LiPS are mitigated in a highly uniform positive electrode comprised of 70 wt. % S in Ti_2C synthesized by reacting sulfur with the hydroxlated surface of the Ti_2C nanosheets. Using detailed XPS analyses, they showed the presence of S-Ti-C bonding at the interface indicating a strong interaction and chemisorption of LiPS onto the "acid" Ti sites and hydroxy surface groups. In their study, they observed that such sites act as active species. In S/Ti_2C cells, initially sorbed LiPS undergo conversion to Li_2S, either by electron transfer via the Ti_2C or by disproportionation, to form multiple Li_2S nucleation sites on the surface. Subsequent LiPS generated during cycling are reduced to sulfide, which preferentially deposit epitaxially on the existing Li_2S nuclei on Ti2C network. Liang *et al.* [299] showed that such a mechanism effectively mitigates the dissolution of LiPS into the electrolyte and provides very good cycling performance with a capacity fade rate of 0.05 % per cycle.

Bao *et al*. [300] enhanced the acidic adsorption capability of MXene nanosheets using nitrogen doping. More importantly, they were able to achieve a high sulfur loading of 5.1 mg cm^{-2} necessary for practical pouch cells. They found that nitrogen-doped MXene nanosheets/sulfur cathodes exhibit a high reversible capacity (1144 mA h g^{-1} at 0.2C rate), a good high-rate capability, and an extended cycling stability (610 mA h g^{-1} at 2C after 1000 cycles). Tang *et al*. [301] achieved *in-situ* formation of a thick sulfate complex layer as the protective barrier for retarding the Li_2S_x migration from S@$Ti_3C_2T_x$ electrodes. They decorated the 2D $Ti_3C_2T_x$ nanosheets with nanoscale S *in-situ* to form a viscous aqueous ink for fabricating freestanding, binder-free, and flexible S@$Ti_3C_2T_x$ electrodes. Unlike traditional carbon hosts, the use of polar $Ti_3C_2T_x$ conductive mediator in their work resulted in high electrical conductivity, mechanical robustness, and a thick sulfate complex layer on the electrode surface. Such properties have been shown to enable fast electron transfer kinetics across the liquid–solid interface and suppressing the migration of Li_2S_x. Beyond traditional coin cells, Tang *et al*. [301] fabricated LSB pouch cell based on the S@$Ti_3C_2T_x$ film and Li ribbon with high capacities (1350 mAh g^{-1} and 1244 mAh g^{-1} in 50% S and 70% S, respectively), excellent rate handling, and ultralow capacity

decay rate (0.035% per cycle in 50% S after 175 cycles and 0.048% per cycle in 70% S after 800 cycles). An exhaustive list of MXene based cathodes for LSBs is provided in **Table 5**.

Table 5. MXenes in Li-Sulfur batteries

Material	Capacity (mAh/g)	Cycle	Current density or C-rate	Year	Ref.
S- Ti_3C_2/C	530	500	1C	2020	[302]
S-Ti_3C_2@CF	626	1000	1C	2020	[303]
Co-CNT@MXene/S composites	900	840	1C	2020	[304]
S@$Ti_3C_2T_x$	1477.2	100	0.2C	2020	[305]
S- CNTs/ $Ti_3C_2T_x$	614	600	1C	2019	[306]
S- $Ti_3C_2O_x$	662	1000	1C	2019	[307]
S-MNSs@d-Ti_3C_2	474	500	1C	2019	[308]
$Ti_3C_2T_x$-S	970	1500	1C	2019	[309]
S@TiO_2/Ti_2C	464	200	2C	2019	[310]
N–$Ti_3C_2T_x$-S	950	200	0.2C	2018	[300]
Li_2S-$Ti_3C_2T_x$	528	100	0.1C	2018	[311]
S@$Ti_3C_2T_x$	724	800	0.2C	2018	[301]
$Ti_3C_2T_x$-S	689.7	1000	1C	2018	[312]
S- CNT- $Ti_3C_2T_x$	450	1200	0.5C	2017	[299]
S- $Ti_3C_2T_x$-RGO	878.4	300	0.5C	2017	[313]

In addition to being used as an exclusive S host, different MXenes hybrids that combine carbon, metal oxides, and polymers have also been realized for LSB cathodes. Wang *et al.* developed a $Ti_3C_2T_x$@mesoporous carbon architecture with metal organic framework (MOF) precursor [314]. Their porous carbon architecture combined with the polar nature of $Ti_3C_2T_x$ confines both active materials and LiPS to reduce loss of S. As a result, they achieved a high discharge capacity of 1225.8 mA h g^{-1} and more than 300 cycles at 0.5C. Nazar *et al.* used CNT/MXene composites for improving the conductivity and preventing restacking of the delaminated MXene nanosheets, which results in excellent long-term cycling performance and fading rates as low as 0.043% per cycle for up to 1200 cycles. Wang *et al.* synthesized freestanding $Ti_3C_2T_x$/rGO hybrid aerogel electrode using a liquid Li_2S_6 catholyte as the active material [315]. Unlike elemental octa-sulfur precursors, the Li_2S_6-based cathode facilitates homogeneous distribution of active materials within the $Ti_3C_2T_x$/rGO conductive backbone. The robust aerogel electrode allows high areal sulfur loading up to 6 mg cm^{-2} with a high-capacity of 1270 mA h g^{-1} at 0.1C and good cycling stability at 1C for 500 cycles with a low-capacity decay rate of 0.07% per cycle.

Wang *et al.* [316] wrapped S@ $Ti_3C_2T_x$ in a thin layer of polydopamine (PDA) to achieve dual polysulfide confinement strategy. In their cathodes, $Ti_3C_2T_x$ acts as both a highly conductive

skeleton and an active adsorption site for LiPS. The outer PDA layer further prevents S/LiPS dissolution by serving as a barrier to reduce direct contact of active materials with the liquid electrolyte. Such S@$Ti_3C_2T_x$/PDA cathodes displayed an initial discharge capacity of 1001 mA h g^{-1} with a capacity retention of 65% over 1000 cycles at 0.2C. Gao *et al*. [317] embedded TiO_2 quantum dots (QDs) into ultrathin $Ti_3C_2T_x$ MXene nanosheets through cetyltrimethylammonium bromide (CTAB)-assisted solvothermal synthesis. TiO_2 QDs provide extra active sites for LiPS entrapment in addition to mitigating restacking of MXene layers. They showed that TiO_2 QDs@MXene/S cathode is superior to the MXene/S cathode in terms of long-term cyclability and rate capability with a high capacity of 680 mA h g^{-1} at 2C after 500 cycles. Pan *et al.* fabricated an accordion-like TiO_2–$Ti_3C_2T_x$ MXene heterostructure by annealing $Ti_3C_2T_x$ MXene in air [307]. Following heat treatment, -O functional groups become the dominant surface termination on the $Ti_3C_2T_x$ MXene. Pan *et al.* found that such -O groups contribute to extra Li storage to the sulfur cathode resulting in a reversible capacity of 367 mA h g^{-1} at a high rate of 10C. Du *et al*. [310] synthesized a S@TiO_2/Ti_2C nanoarchitecture by embedding sulfur encapsulated TiO_2 hollow nanospheres into MXene Ti_2C interlayers. Their S@TiO_2/Ti_2C composites exhibited an excellent electrochemical performance with an initial discharge specific capacity was 1408.6 mAh g−1 at 0.2C with a high sulfur content of 78.4 wt.%. At higher current rates of 2C and 5C, LSBs with S@TiO_2/Ti_2C showed a capacity up to 464.0 and 227.3 $mAhg^{-1}$ after 200 cycles, respectively. Similar to Pan *et al.* [307], the improved performance of S@TiO_2/Ti_2C composites was attributed mainly to the active chemical adsorption sites on TiO_2 for LiPS entrapment in addition to improved physical stability to reduce MXene restacking.

Other 2D heterostructures combining MoS_2, C, N-doped C, and MXenes have been used to further improve the performance of LSBs [318]. By combining the excellent electrical conductivity of octahedral 1T phase MoS_2 with the strong interactions between positively charged S-vacancy and negatively charged LiPS, Zhang *et al.* demonstrated a new hybrid material by confining $Ti_3C_2T_x$ MXene into 1T-2H MoS_2-nitrogen-doped carbon composites (denoted as MXene/1T-2H MoS_2-C) for developing high-performance LSBs. Such composites showed a three-fold advantage: (1) the sulfur vacancies in MoS_2 provide an effective way both trap LiPS and dynamically enhance LiPS redox reaction; (2) the high electrical conductivity of $Ti_3C_2T_x$ and N-doped carbon facilitate several low resistance percolating paths for charge transfer, particularly at high rates; (3) 3D hierarchical porous structure can effectively buffer the volume expansion and avoid the rapid capacity fading. Consequently, the MXene/1T-2H MoS_2-C cathode achieved cyclic stability with a negligible capacity fading rate of 0.07% per cycle, excellent rate capability of 677.2 mAh g^{-1} under 0.5 C, and reliable operation in soft-package batteries. Xiao *et al.* [319] interspersed $Ti_3C_2T_x$ MXene nanodots between $Ti_3C_2T_x$ MXene nanosheets (TCD-TCS) to achieve a high sulfur loading up to 13.8 mg cm^{-2}. Considering that these architectures do not use any carbon additives, the TDS-TCS cathodes exhibited an ultrahigh

volumetric capacity (1957 mA h cm^{-3}) and high areal capacity (13.7 mA h cm^{-2}). However, the electrode was only stable up to 50 cycles.

6.3 MXenes in electrocatalysis

Naturally abundant sources such as H_2O, H_2, O_2, CO_2, and N_2 can be converted into renewable electrochemical energy using electrocatalysts [320-322]. Although hydrogen production from water splitting by electrolysis and energy conversion in fuel cells with water as a by-product have been known for a long time, conventional electrocatalysts (e.g., Pt, Ir, and Ru based-oxides) for oxygen evolution reaction (OER), hydrogen evolution reaction (HER) and oxygen reduction reaction (ORR) are neither economically viable nor sustainable [323]. The overall water splitting reaction can occur through multiple pathways based on the pH of the surrounding medium.

In electrocatalytic processes, the electrochemical properties of a catalyst are determined by its ability to adsorb or desorb the key reaction intermediates involved in the electrocatalytic reaction. In case of HER, all pathways involve the adsorption of H* onto the electrode surface. Accordingly, the free energy of H adsorption (ΔG_{H^*}) is often used as a descriptor of the H_2 evolution kinetics of the catalyst. While $\Delta G_{H^*} \ll 0$ suggests weak interactions between H and the electrode surface, $\Delta G_{H^*} \gg 0$ values indicate strong bonding. An optimal HER catalyst has $\Delta G_{H^*} \sim 0$ (e.g., Pt) allowing H to adsorb/desorb with ease. The OER is a multielectron reaction involving three major intermediate species viz., HO*, O*, and HOO* [324]. In acidic electrolytes, H_2O initially adsorbs onto the catalyst via single-electron transfer to form HO*, which leads to O* upon the removal H^+ and e^- [324]. Subsequently, O* reacts with another H_2O molecule to form HOO*, which is oxidized to O_2 by an electron transfer process. In alkaline media, initially adsorbed OH^- is oxidized to form HO*, which later combines with another OH^- to generate O* and a H_2O molecule. Then O* combines with another OH^- to form HOO*, which reacts with an OH− to form O_2 and H_2O. Among all these intermediates (in both acidic and alkaline media), the absorption of HO* on catalyst and the production of adsorbed HOO* are most important steps in the OER. Accordingly, the binding energy of O* ($\Delta G_{O^*} - \Delta G_{HO^*}$) is widely accepted for evaluating the OER activity of the catalyst [324]. In case of ORR, the $O_2 \rightarrow$ HOO* $\rightarrow$ O* $\rightarrow$ HO* $\rightarrow$ H_2O (i.e., the O* mechanism) is now the most generally recognized mechanism [325]. An alternative mechanism involves: $O_2 \rightarrow$ HOO* $\rightarrow$ 2OH* $\rightarrow$ OH* $\rightarrow$ H_2O (i.e., the 2OH* mechanism), where 2OH* replaces the intermediary O* in the O* mechanism [325]. Because two OH* may bind to distinct active sites, the free energy of 2OH* is roughly equal to that of O*. According to the well-known scaling equation $\Delta G_{O^*}=2\Delta G_{OH^*}$, these two pathways are thermodynamically comparable for catalysts with near continuous active sites.

Any nanostructured material is expected to exhibit high catalytic activity due to the high specific surface area. In electrocatalysis, the catalytic activity also relies on surface electronic

states arising from defects and specific crystal structure of the edge sites. Considering that MXene electronic properties can be modulated by surface functionalization, they have been demonstrated to be promising candidates for electrocatalysts [326-328]. In addition to providing high specific surface area and rich edges for the catalytic activity, the facets of the MXene layers can be altered using several methods like functionalization, defect engineering, edge control, and doping have been assigned to improve the catalytic performance. Theoretical and experimental investigations demonstrated that many MXenes show favorable ΔG values for acting as catalysts in HER, OER, and ORR (see Table 1). For example, in case of $W_{1.33}C$ nanosheets, HER activity was found to increase by using defects [324]. Under high cathodic potentials, H^+ ion adsorbed inside vacancy is transformed into a chemically bound H atom, which resulted in thermoneutral ΔG_{H^*} ensuing in an onset potential shift inthe anodic direction. At anodic conditions, H^+ was observed to leave the vacancy, which led to a less thermoneutral ΔG_{H^*} and consequently a shift in the cathodic direction of the onset potential. Therefore, the increased HER activity was found for $W_{1.33}C$ nanosheets. Similarly, inserting or intercalacting transition metal (TM) atoms into MXenes or combining them with other metal/2D material catalysts (e.g., MoS_2) has been shown significantly improve the OER activity while maintaining or even increasing the HER performance. **Table 6** shows the electrocatalytic HER and/or OER performance of recently reported pristine/doped MXenes-based electrocatalysts along with various composites. Researchers have studies multiple types of composites using other 2D materials such as MoS_2, Pt, Ru, and other Fe/Co/Ni compounds. Among these, some MXenes-composite catalysts such as $Mo_2TiC_2T_x$-PtSA 66], Ru-$NTi_3C_2T_x$ [329], and Pt-SA/$Ti_3C_2T_x$ [327] exhibit satisfactory catalytic performances comparable to those of Pt-based catalysts. Even so, we believe that there remains substantial scope for improvement in terms of electrocatalytic activity and stability

Table 6. MXenes/MXene composites for HER and OER

Material	Electrolyte	Mass loading (mg/cm^2)	Overpotential (mV)	Tafel Slope (mV/dec)	Stability	Ref
Pristine/doped MXenes for HER						
O-terminated $Ti_3C_2T_x$	0.5 M H_2SO_4	204	190	60.7	24 h	[330]
F-terminated Ti_2CT_x	0.5 M H_2SO_4	0.175	170	100		[331]
$Ti_3C_2O_x$	0.5 M H_2SO_4	0.204	190	60.7	1000 cycles	[330]
$V_4C_3T_x$	0.5 M H_2SO_4	1	200	NA	NA	[332]
N-Ti_2CT_x	0.5 M	NA	215	NA	NA	[333]

	H_2SO_4					
$Ti_3C_2T_x$nanofibers	0.5 M H_2SO_4	NA	169	NA	NA	[334]
Co^{3+}-Ti_2CT_x	1.0 M KOH	NA	458	NA	NA	[335]
N-$Ti_3C_2T_x$@600	0.5 M H_2SO_4	0.276	198	92	30	[336]
Mo_2CT_x:Co	1 M H_2SO_4	1.00	180	59	3	[337]
Mo_2CT_x	0.5 M H_2SO_4	0.1	189	74	2 h	[328]
Co^{3+}-Cr_2CT_x	1.0 M KOH	NA	404	NA	NA	[335]
Co^{3+}-V_2CT_x	1.0 M KOH	NA	460	NA	NA	[335]
MXene composites with MoS_2 for HER						
o-MoS_2@Mo_2CT_x	1 M KOH	0.35	112	82	>18 h	[338]
MoS_2/Ti_3C_2	0.5 M H_2SO_4	0.35	~280	68	36 h	[339]
MoS_2/$Ti_3C_2T_x$	0.5 M H_2SO_4	0.27	152	70	12 h	[340]
MoS_2/Ti_3C_2-MXene@C	0.5 M H_2SO_4	0.4	135	45	>20 h	[341]
MoS_2/Ti_3C_2	0.5 M H_2SO_4	NA	110	NA	NA	[339]
MoS_2@Mo_2CT_x	1 M KOH	0.71	197	113	>8	[340]
MXene Pt/Ru composites for HER						
Pt_xNi NWs/Ti_3C_2	0.5 M H_2SO_4	0.127	18.55	13.37	<2 h	[342]
Pt_{SA}/$Mo_2TiC_2T_x$	0.5 M H_2SO_4	1	30	30	>100 h	[343]
Pt/ $Ti_3C_2T_x$ – 550	0.1 M $HClO_4$	NA	32.7	NA	NA	[344]
Pt/ $Ti_3C_2T_x$	0.5 M H_2SO_4	0.38	55	70	20 h	[327]
PtNPs/$Ti_3C_2T_x$	0.1 M H_2SO_4	NA	226	NA	NA	[345]
PtO_aPdO_bNPs@$Ti_3C_2T_x$	0.5 M H_2SO_4	NA	57	NA	NA	[346]
Pt@$Ti_3C_2T_x$	0.5 M H_2SO_4	NA	69.8	64.2	NA	[347]
Pt@$Ti_3C_2T_x$	0.5 M H_2SO_4	NA	43	80	NA	[348]
$Ti_3C_2T_x$ @Pt/carbon nanotubes	0.5 M H_2SO_4	NA	62	78	NA	[349]
Ru_{SA}-N-S-$Ti_3C_2T_x$	0.5 M H_2SO_4	1	76	90	>10 h	[329]
MXene and Fe/Co/Ni compound composites for HER						

$Ni_3S_2/Ti_3C_2T_x$	1.0 M KOH	4.9	72	45	>12 h	[350]
NiS_2/V_2CT_x	1.0 M KOH	NA	179	85	NA	[351]
$Ni_{0.9}Co_{0.1}$@Nb-$Ti_3C_2T_x$	1.0 M KOH	NA	43.4	NA	NA	[352]
NiFe-LDHs/Ti_3C_2/NF	1 M KOH	0.1	132	70	280 h	[353]
Ni0.9$Fe_{0.1}PS_3$@ $Ti_3C_2T_x$	1.0 M KOH	NA	196	NA	NA	[354]
CoP@3D $Ti_3C_2T_x$	1.0 M KOH	NA	168	NA	NA	[355]
$TiOF_2$@$Ti_3C_2T_x$	0.5 M H_2SO_4	0.177	197	56.2	24	[356]
MXenes/MXene composites for OER						
FeNi-LDH/$Ti_3C_2T_x$	1.0 M KOH		298 mV	43		[353]
CoNi-ZIF-67@$Ti_3C_2T_x$	1.0 M KOH		323 mV	65.1		[357]
$Ti_3C_2T_x$-CoBDC	0.1 M KOH		410 mV	48.2		[358]
g-C_3N_4/$Ti_3C_2T_x$film	0.1 M KOH		420 mV	74.6		[326]
Co-Bi/$Ti_3C_2T_x$	1.0 M KOH		250 mV	53		[357]
S-$NiFe_2O_4$@Ti_3C_2@NF	1.0 M KOH		270 Mv (at 20 mA cm^{-2})	46.8		[359]
NiCoS/$Ti_3C_2T_x$	1.0 M KOH		365 mV	58.2		[360]
Co^{3+}-Cr_2CT_x	1.0 M KOH		420 mV	NA		[335]
Co^{3+}-V_2CT_x	1.0 M KOH		420 mV	NA		[335]
Co^{3+}-Ti_2CT_x	1.0 M KOH		420 mV	NA		[335]
PtO_aPdO_bNPs@$Ti_3C_2T_x$	0.1 M KOH		310 mV	NA		[346]
$Ni_{0.7}Fe_{0.3}PS_3$@ $Ti_3C_2T_x$	1.0 M KOH		282 mV	NA		[354]
Co/N-CNTs@$Ti_3C_2T_x$	0.1 M KOH		411	NA		[361]
CoP@3D $Ti_3C_2T_x$	1.0 M KOH		280	NA		[355]
Black Phosphorous dots/$Ti_3C_2T_x$	1.0 M KOH		360	64.3		[362]
FeOOH sheets/$Ti_3C_2T_x$	1.0 M KOH		400	95		[363]
Co_3O_4/$Ti_3C_2T_x$	1.0 M KOH		340	63.97		[364]
$Ti_3C_{1.6}N_{0.4}$	1.0 M KOH		245.8 (at 1 mA cm^{-2})	216.4		[324]
$Ti_3C_2T_x$/TiO_2/NiFeCo-LDH	0.1 M KOH		320	98.4		[365]
Co-LDH@$Ti_3C_2T_x$	1 M KOH		340	82		[366]
CoFe-LDH@$Ti_3C_2T_x$	1 M KOH		319	50		[367]
FeCo-LDH/$Ti_3C_2T_x$	1 M KOH		268	85		[368]
NiCo-LDH/$Ti_3C_2T_x$/NF	1 M KOH		223 (at 100 mA cm^{-2})	47.2		[369]
CoP/MXene	1 M KOH		280	95.4		[370]
NiCo-LDH/MXene/NF	1 M KOH		257.4 (at 100 mA cm^{-2})	68		[371]
NiFeCe-LDH/MXene	1 M KOH		260	42.8		[372]

NiFeP-LDH/MXene	1 M KOH	286	35	[373]
NiFe LDH/NiTe/NF	1 M KOH	228 (at 50 mA cm^{-2})	51.04	[374]
Co_3O_4/MXene	1 M KOH	300	118	[375]

7. Sensing and biosensing

With the development of MXene intercalation methodology and chemical functionalization techniques, its potential capability for sensing and biosensing have been extensively explored. Its high electric conductivity (up to 10^4 S cm^{-1}) and negatively charged surface environment enables the controlled combination of MXene with other functional materials to offer various technological solutions for the development of electronic/photonics devices capable of expressing multiple functionalities for smart sensing, such as chemical sensors, biosensors and pressure/strain sensors.

7.1 MXene as chemical sensor

MXene possesses two chemically tunable properties for chemical sensing. The first characteristic is its capability to adsorb and intercalate molecules, representing which alters its surface potential or interlayer spacing resulting in resistance changes. The latter feature is the complex oxidation states of transition metal ions (*e.g.* Ti in $Ti_3C_2T_x$) which determines the unavoidable aerobic oxidation during the processing of MXenes. If one considers $Ti_3C_2T_x$ as exemplary system, a variety of Ti atoms from Ti (I) (Ti-C) to electron-deficient Ti (IV) are present, as well as intermediate oxidation states of Ti (II) and Ti (III). This allows charge transfer between electroactive molecules and MXene, yielding to changes in electric signals. It noteworthy that key factors in chemical sensing include sensitivity, limit of detection (LOD), selectivity, response speed and recovery time. Chemical functionalization of the device's interfaces as well as the optimization of device architecture are aimed at improving such parameters towards high-performance chemical sensors.

7.1.1 MXene as humidity sensors

Commonly, current nanomaterial-based sensors display lesser sensitivity in low relative humidity range (<40% RH). By interface functionalizations of $Ti_3C_2T_x$, its humidity sensitivity can be amplified. In this framework, Li *et al.* have developed a Schottky junction of TiO_2 grown on partially oxidized Ti_3C_2 (**Fig. 16**a).[376] Water molecules donate electrons to this hybrid, thus lowering the barrier height and leading to lower resistance, as displayed in **Fig. 16**b. Smart textile loaded with $Ti_3C_2T_x$ and silver nanowires (NWs) is reported to be moisture sensitive .[377] Such a Ti_3C_2/TiO_2 hybrid was characterized by capacitance changes (**Fig. 16**c–e), yielding ~280 pF/% RH under low RH. Its enhanced sensitivity is attributed to high specific surface area from TiO_2 and Schottky barrier between Ti_3C_2/TiO_2. With the abundant exposed reactive termination sites on MXene surface, water molecules are more prone to undergo charge transfer with the MXene skeleton to induce a resistance change or to be adsorbed among MXene's interlayers.

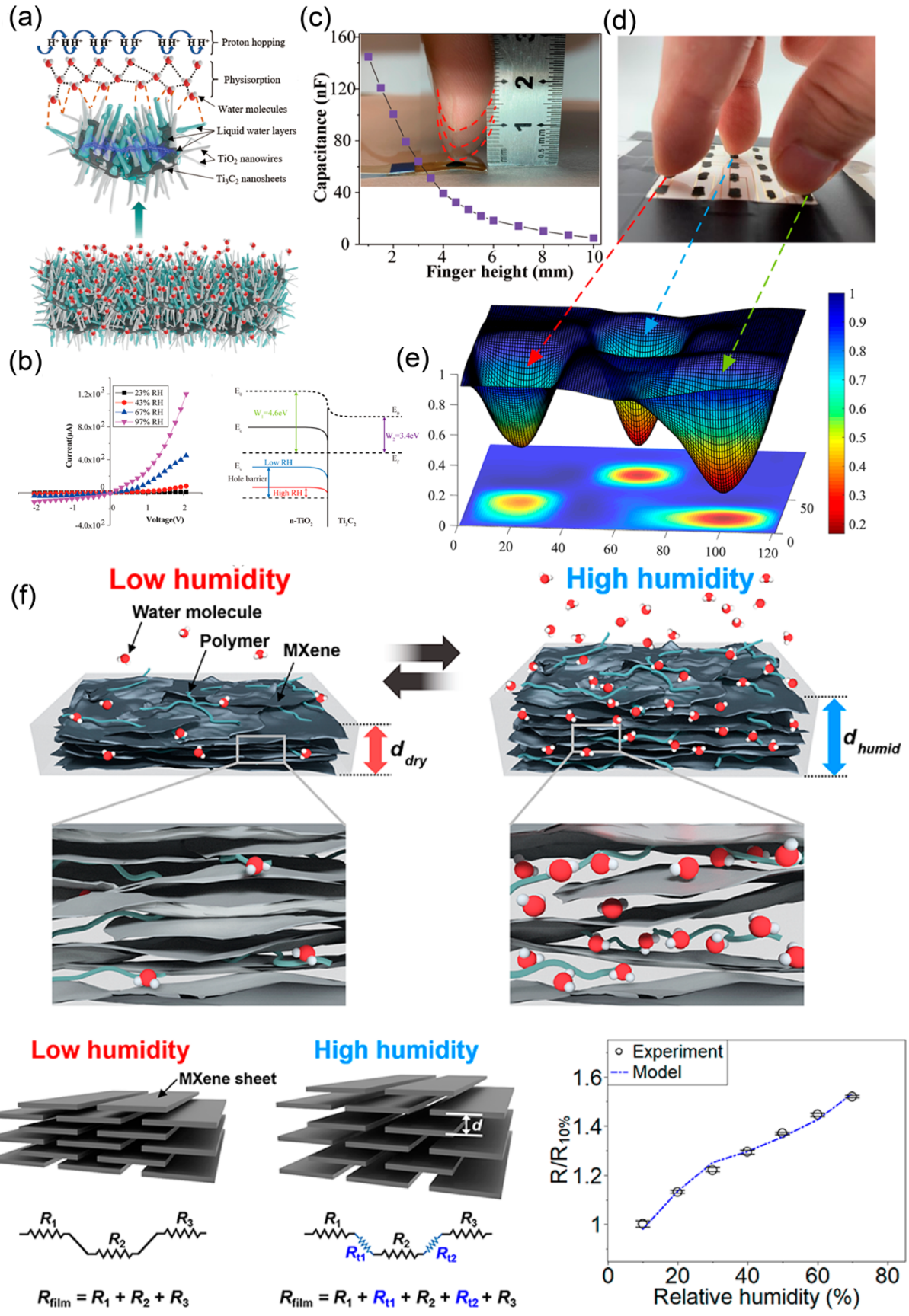
(a)
Proton hopping
Physisorption
Water molecules
Liquid water layers
TiO2 nanowires
Ti3C2 nanosheets
(b)
23% RH
43% RH
67% RH
97% RH
Current(μA)
Voltage(V)
Low RH
High RH
Hole barrier
n-TiO2
Ti3C2
(c)
Capacitance (nF)
Finger height (mm)
(d)
(e)
(f)
Low humidity
High humidity
Water molecule
Polymer
MXene
d dry
d humid
(g)
Low humidity
High humidity
MXene sheet
d
R1
R2
R3
Rt1
Rt2
Rfilm = R1 + R2 + R3
Rfilm = R1 + Rt1 + R2 + Rt2 + R3
Experiment
Model
R/R10%
Relative humidity (%)

Fig. 16. Humidity sensors based on MXene chemiresistors. (a) Schematic of the interaction of water molecules with the surface of Ti_3C_2/TiO_2. (b) Left panel: I–V curves of the Ti_3C_2/TiO_2 composite film with respect to RH levels. These curves are attributed to the Schottky junction formed by the Ti_3C_2/TiO_2 interface. Right panel: Energy-band diagram of the Ti_3C_2/TiO_2 composite. (c) Measured device capacitance as a function of its distance with a human fingertip. Due to the water molecules from the fingertip, the Ti_3C_2/TiO_2 could produce a capacitive response. (d) Photograph of the positions of three fingertips above the 5 × 5 matrix. (e) 3D mapping of the position approaching of three fingertips. Reprinted with permission from ref. [376] Copyright 2019 American Chemical Society. (f) Schematic showing the proposed humidity response mechanism of the MXene/polyelectrolyte multilayers. Schematic diagrams of MXene/polyelectrolyte multilayers and the corresponding electrical circuit models under (left) low and (right) high humidity, which alters the interlayer distance between adjacent MXenes. (g) R_1, R_2, and R_3 are MXene nanosheet resistance, and R_{t1} and R_{t2} are tunneling resistances at the junctions. (f) Left and middle: Model showing the resistance change of MXene/polyelectrolyte under humidity. Right: Response of the MXene/polyelectrolyte to the varying relative humidity by experimental measurements and numerical modeling. Reprinted with permission from ref. [378] Copyright 2019 American Chemical Society.

A recent work reported responsive MXene within a wide range of water vapor pressure (20 mTorr – 20 Torr), corresponding to a RH range of 0.1%–95%.[379] Below a low RH level of 1%, quartz crystal microbalance (QCM) of $Ti_3C_2T_x$ revealed downshifted frequency and increased resistance in $Ti_3C_2T_x$ film. This clearly demonstrates trace amount of water molecules adsorb on $Ti_3C_2T_x$ could be detected by electrical characterizations.

Density Functional Theory (DFT) calculations provided evidence that the oxygen terminations on MXene surface rules its gas sensitivity and separation/capture capability critically.[380] Oxygen terminations on MXene surface renders MXene semiconducting, mainly *p*-type, thereby making its electron-deficient and sensitive to electron-rich molecules.[328] Absorption of various gas molecules to the surface of a multiple types of MXenes have been predicted and confirmed to be greatly affected by oxygen terminations on MXene. This feature provides possibility of integrating functional materials with MXene for specific gas molecule sensing.

The surface of $Ti_3C_2T_x$ is negatively charged due to the abundant hydroxyl groups. This feature makes layer-by-layer assembly of $Ti_3C_2T_x$ and cationic polyelectrolytesfor humidity sensors possible. Such a combination utilizes the hydrophilicity of polyelectrolyte and electron conductivity from MXene towards fast response down to hundreds of milliseconds.[378] When water molecules were adsorbed by polyelectrolyte, the interlayer spacing of $Ti_3C_2T_x$ expands, thus increasing the tunneling resistance (**Fig. 16**f, g). With this design, a real-time monitoring of human breath is demonstrated with a fast recovery time down to several seconds. Taking

advantage of hydrogen bonding interactions in $Ti_3C_2T_x$-cellulose, a MXene fabric for reversible humidity response is demonstrated.[381]

7.1.2 MXene for ammonia detection

NH_3 is one among the most widely employed gases for various applications, including its use as refrigerant in diverse industries and as fertilizer in agriculture. However, ammonia is health hazard, even at low concentrations. Moreover, the precise quantification of NH_3 concentration in patient's breath is instrumental to diagnose kidney and digestive diseases. Aforementioned applications requires detection of NH_3 down to ppm level; hence, it is imperative to develop highly sensitive NH_3 sensors.

DFT calculations have been used to quantify the interaction between NH_3 and O-terminated semiconducting MXenes.[382] It has been revealed that NH_3 molecules adsorb on M_2CO_2 undergo a charge transfer process, making MXenes an electric platform for NH_3 sensing. In line with theoretical predictions, it is experimentally demonstrated that at a 100 ppm level, $Ti_3C_2T_x$ exhibits higher response to NH_3 compared to other molecules.[383] Moreover, termination groups on MXene's surface plays a dominant role in in its interaction with NH_3, with oxygen containing groups displaying higher charge transfer with NH_3 compared to fluorine. Along the same lines, first principle calculations revealed electron-deficient surface of $Ti_3C_2T_x$ is more sensitive to NH_3 than other inorganic gas molecules. This is due to the charge transfer (−0.098 e) from NH_3 to the oxygen functionalization of $Ti_3C_2T_x$ and an adsorption energy of −0.36 eV.[384] Especially, charge transfer from NH_3 to fluorine terminations turns out to be weaker than that to oxygen terminations, in line with previous findings,[382] confirming the paramount role played by oxygen atoms in $Ti_3C_2T_x$'s ammonia sensing capability.

NH_3 sensing performance of a MXene-based device have been further experimentally investigated.[385] To realize flexible gas sensors, $Ti_3C_2T_x$ MXene/graphene hybrid fibers are fabricated. This hybrid combined the high sensitivity of MXene's for NH_3 with the graphene's mechanical robustness. The hybrid fiber displayed an NH_3 response of 7% at room temperature with a NH_3 sensitivity being higher than that from single component of MXene or graphene.

Alongside the humidity sensing by MXene/polyelectrolyte hybrid,[378] devices with similar composition (MXene/cationic polyacrylamide) have been reported.[386] Thanks to the hydrogen bonding between NH_3 and polyacrylamide, this composite displayed better adsorption/capturing capability for NH_3.

Another versatile route towards the chemical functionalization of MXenes relies on intercalation chemistry. Insertion of functional molecules into MXene's interlayer might deliver unprecedented changes to its electric characteristics and gas sensitivity. Yang et al. described an alkaline treated $Ti_3C_2T_x$ towards high performing NH_3 and humidity sensors.[387] Na^+ cations are intercalated into $Ti_3C_2T_x$'s interlayer to increase the interlayer spacing and oxygen-to-fluorine

termination ratio. This might increase the density of analyte molecule adsorption sites on $Ti_3C_2T_x$'s surface. This finding has been further investigated by *in-situ* X-ray diffraction[388]; gas-induced interlayer swelling of $Ti_3C_2T_x$ MXene thin films and its influence on gas sensing performance are correlated.

7.1.3 MXene for volatile organic compounds detection

In addition to H_2O and NH_3, volatile organic compounds (VOCs) are common both in domestic life and chemical industry. Some of the VOCs are hazardous to human and environmentally unfriendly. Therefore, the monitoring of VOCs concentration is critical for the public health and safety. Pazniak et al. investigated the sensing performance of $Ti_3C_2T_x$ towards a variety of VOCs with simple structure.[389] Partially oxidized $Ti_3C_2T_x$ has been found to display higher sensitivity to these molecules, thanks to its *p*-type properties. As a result, the device can be responsive to ppm levels of VOCs. Pristine $Ti_3C_2T_x$ display a decreased conductance upon exposure to ethanol. However, the opposite trend is observed with partially oxidized $Ti_3C_2T_x$. Due to TiO_2, the device conductance decreased by orders of magnitude, converting from metallic type to semiconducting, thereby enhancing its detection limit to ppm concentrations.

The reactivity of $Ti_3C_2T_x$ with ambient oxygen yielding to the gradual generation of a TiO_2 coating layer affects the gas sensing device stability. To address this limitation, Chen described a superhydrophobic passivation for $Ti_3C_2T_x$.[390] After fluoroalkylsilane treatment, $Ti_3C_2T_x$'s surface became hydrophobicand exhibited higher response towards common VOCs when compared to $Ti_3C_2T_x$, including methanol, ethanol, acetone, benzene and toluene (**Fig. 17**a). Fluoroalkylsilane expanded the interlayer distance of $Ti_3C_2T_x$, as schematically displayed in **Fig. 17**b, thus facilitating the gas diffusion within the layers to enhance the device sensitivity.

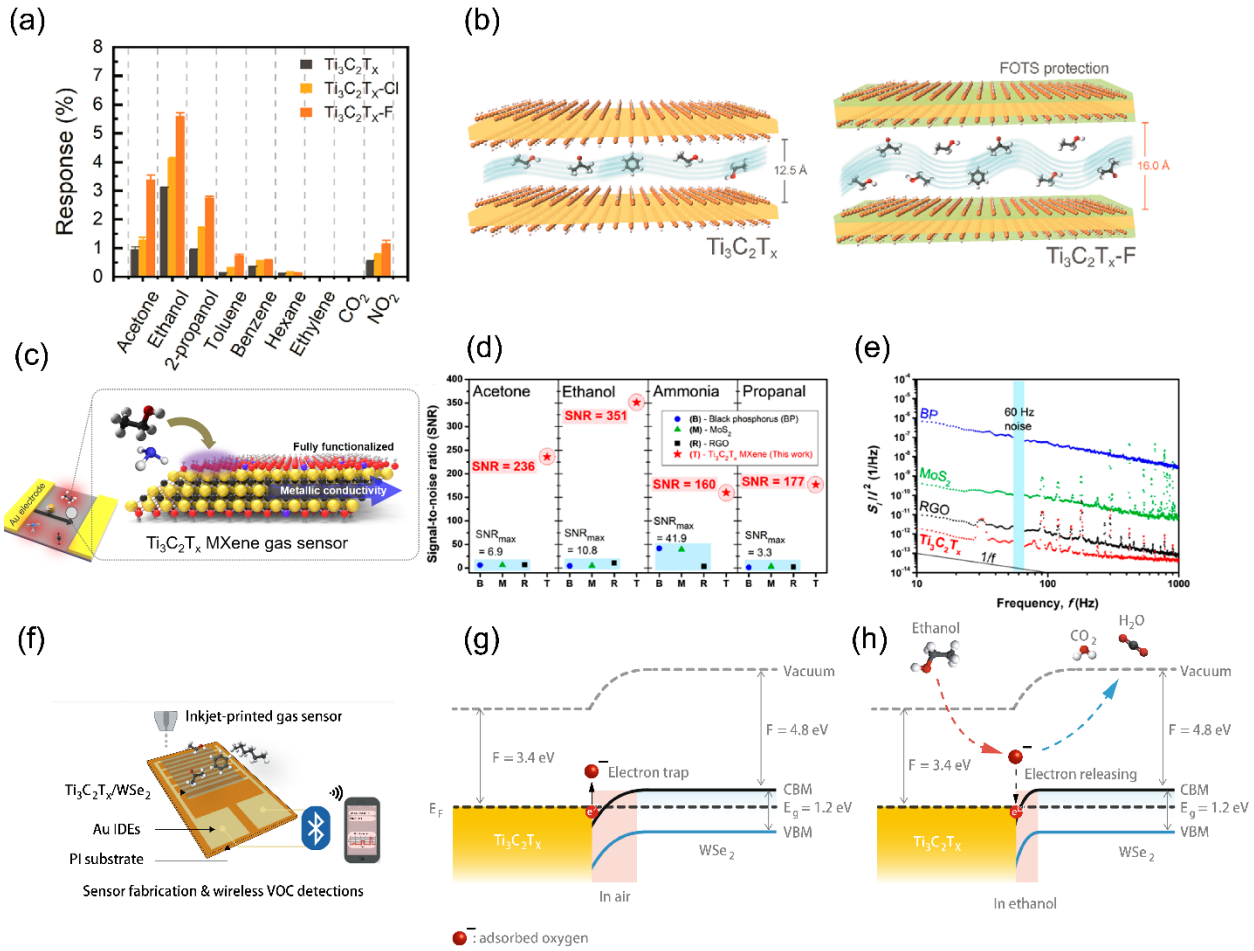

Fig. 17. VOC sensing examples of MXene-based chemiresistors. (a) Maximal response changes upon exposure to various gases. (b) Schematics of $Ti_3C_2T_x$ and $Ti_3C_2T_x$-F upon exposure to VOCs. FOTS passivation of $Ti_3C_2T_x$ MXene prevents it from oxidation, enabling a longer shelf-life. Reprinted with permission from ref. [390]. Copyright 2020 American Chemical Society. (c) Schematic illustration of the $Ti_3C_2T_x$ films and its atomic structure. (d) Maximal SNR values of sensors upon exposure to 100 ppm of acetone, ethanol, ammonia, and propanal. (e) Flicker noise measured by normalized noise power spectral density (SI/I2) as a function of frequency. Reprinted with permission from ref. [391]. Copyright 2018 American Chemical Society. (f) Schematic illustration of inkjet-printed gas sensors based on $Ti_3C_2T_x/WSe_2$ in detection of volatile organic compounds with a wireless monitoring system. Enhanced sensing mechanism of $Ti_3C_2T_x/WSe_2$ heterostructure. Energy-band diagram of the $Ti_3C_2T_x/WSe_2$ in (g) air and (h) ethanol, showing the variation of the depletion layer with interaction between adsorbed oxygen species and ethanol molecules. Reprinted with permission from ref. [392]. Copyright 2020 Nature.

In addition to analyte selectivity of MXene gas sensors, signal-to-noise ratio (SNR) represents a critical parameter. Determination of such a parameter allows the precise detection of molecules with a low LOD. In particular, detection of VOCs at ppb level is critical for the early diagnosis

of diseases and as alert for hazardous compound leakage. Kim *et al.* reported metallic $Ti_3C_2T_x$ exhibiting higher SNR compared to any other 2D material based device (**Fig. 17**c).[393] SNR was obtained by dividing the gas response by the device noise (**Fig. 17**d, e). Due to the high conductivity of $Ti_3C_2T_x$, its noise level is low. Combined with $Ti_3C_2T_x$'s abundant surface terminations, responses with sufficient magnitude were obtained with ppb level sensing of acetone, ethanol and ammonia.

In some cases, gas sensors need to be mechanically flexible, for example, on clothes as wearable systems. Yuan *et al.* reported a $Ti_3C_2T_x$ functionalized polymer fiber.[394] Such a device architecture yielded a large adsorption surface area for the sensing element while at the same time retaining the flexibility from fibers. The resulting gas sensor displayed a higher response range from 1% to 2% under 10 ppm level of acetone, methanol and ethanol.

V_2CT_x was found to be esponsive to nonpolar gas molecules compared to $Ti_3C_2T_x$. Lee *et al.* fabricated chemiresistive devices from tetrabutyl ammonium hydroxide treated V_2CT_x.[395] The V_2CT_x sensor was able to detect 100 ppm ethanol and acetone with a gas response of 0.08 and 0.02, respectively.

Integration of MXenes with electroactive materials might bring better sensing performance. Zhao *et al.* performed the *in-situ* polymerization of aniline on $Ti_3C_2T_x$ to afford a polyaniline/$Ti_3C_2T_x$ nanocomposite that display high gas sensitivity and fast operation.[396] The response (i.e. $\Delta R/R_0$) reached up to 40% for 200 ppm ethanol and ~20% for same level of methanol, acetone and ammonia.

Also the blend of PEDOT:PSS and $Ti_3C_2T_x$ was employed for gas sensing.[397]The resulting device exhibited a gas selectivity to methanol (0.7%) and relatively lower response (0.1%) to ethanol and acetone.

Alongside MXene's combination with conducting polymers, MXene hybrids with 2D materials were also exploited. Chen *et al.* developed an inkjet-printed $Ti_3C_2T_x/WSe_2$ hybrid sensor with a high sensitivity to alcohol molecules, benzene and acetone (**Fig. 17**f).[392] A working mechanism was proposed based on the oxygen-containing VOC molecules filling the electron-traps in the $Ti_3C_2T_x$, thereby eliminating the depletion layer between $Ti_3C_2T_x/WSe_2$ interfaces and forming n-type current to increase its conductivity, as depicted in **Fig. 17**g, h.

In addition to VOCs, aromatic molecules are widely utilized in cosmetics and pharmaceutical industry. For example, benzene and its derivatives are cancerogenic. Therefore, selective sensing of aromatic VOC is highly sought after. Shuvo *et al.* demonstrated that $Ti_3C_2T_x$ exhibits a selective sensing of toluene. Moreover, selectivity to this analyte could be further enhanced by 3-fold via sulfur-doping, attaining a response of −11.9% under 1 ppm of toluene [398]. At the same time, pristine $Ti_3C_2T_x$ revealed notably inferior response to hexyl acetate, hexane and ethanol.

CuO is a well-established component for a wide spectral of gas sensing yet featuring a low response. Hermawan *et al.* described a CuO nanoparticle/$Ti_3C_2T_x$ hybrid composite for precise monitoring of toluene.[399] This hybrid demonstrated improved toluene response of 11.4, being

higher than individual CuO and $Ti_3C_2T_x$. This improvement was attributed to the Schottky junction formed in CuO/$Ti_3C_2T_x$ interface.

Guo *et al.* reported a toluene-selective gas sensor based on Mo_2CT_x.[400] The device response to a variety of VOCs, including toluene, benzene, ethanol and methanol were tested. This device display a high sensitivity towards aromatic molecules over alcohols. A higher electric response and a lower detection limit of 220 ppb was observed for toluene when compared to benzene, thus making the Mo_2CT_x device a good sensor for aromatic molecules. Olfactory sensing or electronic noses is critical for flavor and odor recognition, which is vital for the realization of biomimetic devices and artificial intelligence. Generally, an olfactory sensor is required to be responsive to a specific molecule and can be resettable after sensing operations. Such a proof-of-concept was reported by Ciou et al.[401] In particular, phenethyl alcohol was found to increase the interlayer spacing of $Ti_3C_2T_x$ due to intercalation. By electric-heating, $Ti_3C_2T_x$ would release the intercalated phenethyl alcohol to regain its initial interlayer distance. By and large, gas sensing process of MXene does not only occur solely on its outmost surface, but it also involves the intercalation/deintercalation step, which might deliver more substantial resistance change than that ensuing from the mere surface adsorption, due to the highest surface area available for interaction with the gas analyte molecules.

7.1.4 MXene for H_2O_2, NO_x and other common chemical sensing

The potential of MXenes for being integrated in chemiresistors is not limited to common inorganic gas molecules and VOCs. Its performance for oxidative or reductive chemicals such as H_2O_2, NO_x and ionic chemicals was the subject of in-depth studies. Due to the intermediate oxidation states of Ti atoms in $Ti_3C_2T_x$, they can be readily oxidized to form TiO_2 layer under application of an anodic potential in the electrochemical cell.[402] As-synthesized TiO_2 layer displayed to be electrochemically active because of its semiconductor characteristics and it could be utilized to modify the glass carbon electrode (GCE) for electrochemical oxidation of NADH or reduction of H_2O_2. Thus, $Ti_3C_2T_x$ modified electrodes are expected to be employed for in oxidase-based biosensing. The same group further investigated the $Ti_3C_2T_x$ MXene/Pt nanoparticles (NPs) hybrid modified GCE for electrochemical reduction of H_2O_2.[403] $Ti_3C_2T_x$ /Pt NPs functionalized GCE displayed higher redox stability in cyclovoltametric (CV) cycles and higher (CV) current when compared to pristine $Ti_3C_2T_x$ treated GCE. As H_2O_2 sensors, $Ti_3C_2T_x$/Pt NPs treated GCE displayed 3 orders of magnitude lower LOD compared to pristine $Ti_3C_2T_x$.

A NO_2 sensor based on ZnO functionalized, crumpled MXene sphere is developed.[404] Below 100 ppm NO_2, the sensitivity of ZnO/$Ti_3C_2T_x$ sphere is enhanced from 27.27%–41.93% over pristine $Ti_3C_2T_x$ due to higher specific surface area. Choi *et al.* reported a partially oxidized MXene system, TiO_2/Ti_3C_2 for high sensitive NO_2 detector.[405] The gas-sensing mechanisms of such a system is ascribed to charge transfer between NO_2 and MXene surface. Due to the

semiconducting property of TiO_2 and metallic behavior of Ti_3C_2, a Schottky barrier is established at their interfaceand it could be modulated to give distinctive resistance change as response to a specific gas thereby offering a good selectivity. The gas sensor based on TiO_2/Ti_3C_2 displayed 13.7 times higher NO_2 sensitivity than pristine Ti_3C_2 MXene, affording a response of 16.02% below 5 ppm level of NO_2.

Besides the detection of gaseous chemicals, sensing of ions and ionic compounds in aqueous environment using MXene would be of interest to the human health monitoring and biochemistry fields. A field-effect transistor (FET) based on $Ti_3C_2T_x$ nanosheets as channel is reported by Liu *et al*.[406] The device exhibited *n*-type characteristics on SiO_2/Si substrates. Interestingly, the $Ti_3C_2T_x$ nanosheet transistor show substantial response to basic ions, such as hydroxide and carbonate. For less basic ions, such as chloride, sulfate, nitrate and slightly basic acetate, a negligible response is observed. This unique selectivity rendered the device operational without being interfered even in high-salinity solution.

7.2 MXene and its hybrid composite for Pressure Sensors and Strain Sensors

Pressure changes are ubiquitous as they result from mechanical forces or mass transport. Accurate monitoring and measurement of such a parameter is crucial for actuators and human health care devices of everyday applications. As a highly conductive and dispersible 2D materials, MXenes can potentially be used to form percolation pathways for charge transport in hybrid films. Therefore, a general protocol for the development of MXene-based pressure or strain sensors relies on the combination of conductive MXenes with elastic but insulating elastomers. Such a blend behaves as insulators when no external mechanical forces is applied. However, when it is subjected to a pressure change, it produces an increase of its conductance due to the formation of MXene percolative network. By this principle, MXene/elastomer formulation can be utilized to construct piezoresistive devices. Moreover, by taking advantage of the elastic nature of polymeric binders, MXene-based pressure and strain sensors could be manufactured into desired geometry configuration, opening the door towards their use for the realization of health monitoring system, acoustic sensors and soft-material robotics. Another merit brought by this technology is ambient operational stability due to the encapsulation effect of elastomer, hindering MXene from ambient oxidation [407-428]. To construct such sensors, MXene flakes can serve as conductive components, while insulting, elastomeric binders comprise polydimethylsiloxane (PDMS), polyurethane (PU) or natural rubber. State-of-the-art pressure sensors based on MXene can be classified into the following classes by virtue of their device architecture; (1) MXene film deposited onto elastic substrates; (2) MXene nanosheets functionalized polymer fibers; (3) 3D microstructured MXene with high elasticity; (4) Aerogel and hydrogel based on MXene nanosheets.

The sensitivity of MXene piezoresistors is defined by:

$$S = (\Delta I/I_0)/\Delta P$$

Where ΔI is relative current change under pressure, I_0 is the initial current before pressure application and ΔP represents the pressure change. It should be noted MXene/elastic polymer systems would deform its shape by compression or elongation under the effect of external pressure or strain change, which in turn tune the density of MXene conducting percolation pathways as a response. For strain sensors, gauge factor, a parameter to quantify resistance change of piezoresistor under strain change, can be described by[429]:

$$GF = (\Delta R/ R_0)/\varepsilon = (1+2\upsilon)+ (\Delta\varrho/\varrho_0)/\varepsilon$$

Where ΔR is resistance change, R_0 is initial resistance without application of pressure, ε represents the strain. Meanwhile, υ refers to the poisson's ratio of the piezoresistive material, $\Delta\varrho$ is the resistivity change under strain and ϱ_0 is the initial resistivity of the piezoresistive material without strain. For high sensitivity and gauge factor, it is apparent that the device model based on MXene conductive nanosheets distributed in an elastic network of polymers are well in line with these equations.

7.2.1 MXene and MXene hybrid film for pressure sensors

The controlled modification of the structure and morphology of a MXene hybrid is therefore key for the development of piezoresistive pressure sensors. **Fig. 18**a–c displays the *in-situ* transmission electron microscopy (TEM) image revealing the reduced interlayer spacing of $Ti_3C_2T_x$ under external pressure.[407] The gauge factor in such a device can reach 180.1 when the strain was below 1%. Subsequently, a general methodology for the realization of MXene pressure sensors relies on the deposition of MXene nanosheets onto elastic substrates. As the system deforms under pressure, the density of MXene percolations as well as the distance between MXene nanosheets gets altered yielding to changes in its resistance (**Fig. 18**a). For example, Guo *et al.* presented a pressure sensor made of porous MXene-loaded tissue paper sandwiched between two layers of biodegradable polylactic acid (PLA) thin sheets.[408]

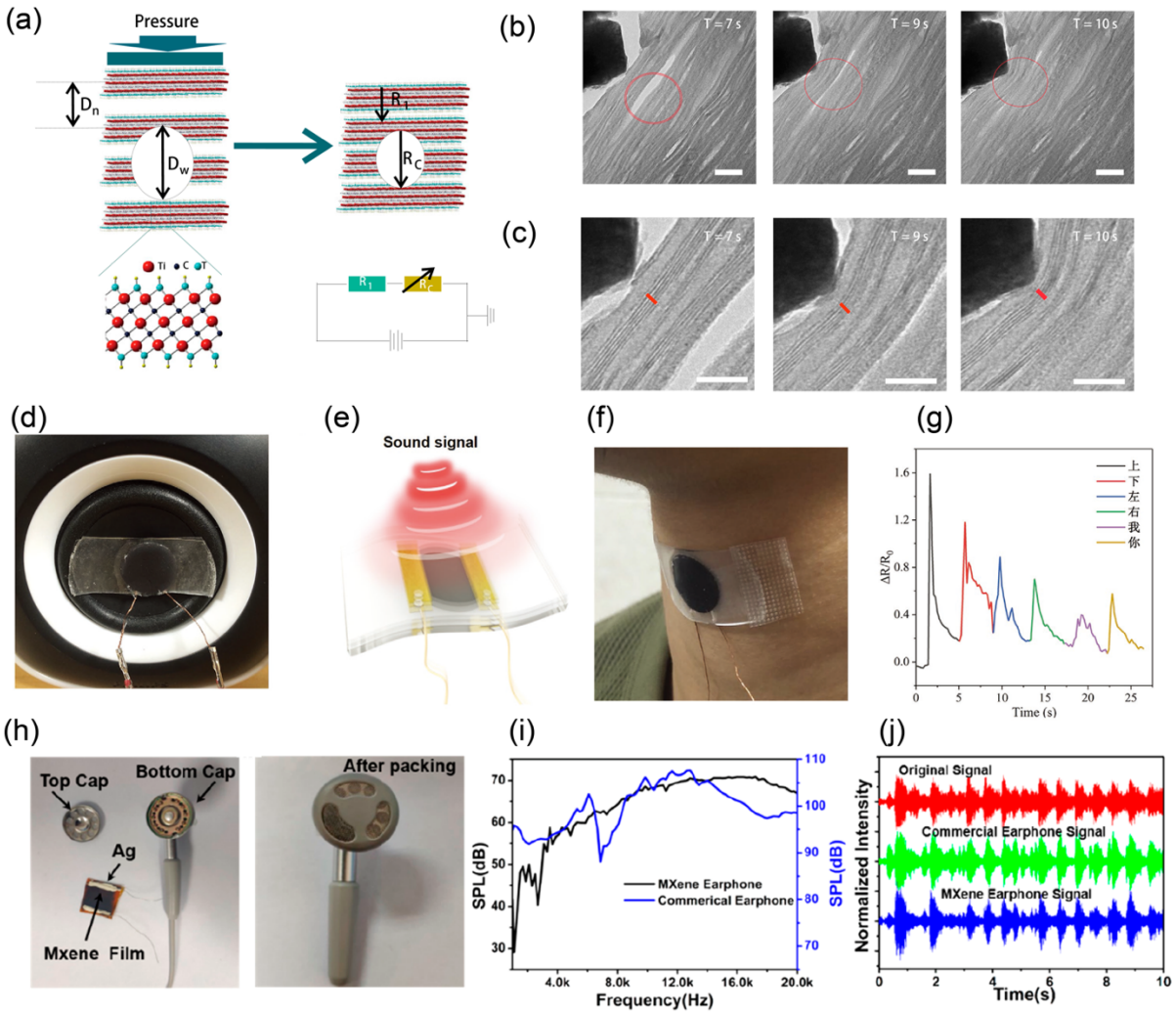

Fig. 18. MXene-based pressure sensors and acoustic sensors. (a) Working mechanism of a MXene-based piezoresistive sensor. Distances between two neighboring interlayers of the MXenes in the sensor decrease under an external pressure. The wider distance (D_w) between two interlayers is easier to be compressed, while the narrower distance (D_n) between two lattices has a smaller compress ratio. Right bottom: The equivalent circuit diagram of MXene-based piezoresistive sensor, where the total resistance falls due to the distance decrease. (b) From left to right, the wider distance in the MXene suffers a rapidly decrease under the external force, from ~12 nm, via ~3 nm to ~0 nm at 7, 9 and 10 s in sequence. (c) From left to right, the narrower distance (4 spacings) labeled by red line ranges from 5.23 nm, via 4.98 nm then to 4.81 nm at 7, 9 and 10 s in sequence. Reprinted with permission from ref. [407]. Copyright 2017 Nature. Detection of vibrations generated by sound signals at different frequencies and intensities: (d) Photograph of the MXene sound detector attached to the loudspeaker. (e) Schematic of the sound signal acting on the MXene sound detector. (f) Photograph of the MXene sound detector attached to the volunteer's throat. (g) Device resistance variation waveform toward the human

throat vibrations of pronunciation of Chinese characters. Reprinted with permission from ref. [409]. Copyright 2020 Wiley. Flexible MXene earphone. (h) Packing the MXene device in a commercial earphone case. (i) The SPL curves of an MXene earphone compared with those of a commercial earphone. (j) The sound waves of the original audio signal, commercial earphone audio signal, and MXene earphone audio signal. Reprinted with permission from ref. [410]. Copyright 2019 American Chemical Society.

A highly porous, MXene hybrid film based MXene/carbon nanotube/polyvinylpyrrolidone has been proposed.[411] This structure features macroscopic lamellar MXene sheets interconnected by dendritic carbon nanotube/polyvinylpyrrolidone bundles. As a result, tactile sensors with such a structure displayed a detection limit of 0.69 Pa and a short response time of 48 ms.

To address the need for portable human healthcare monitoring, $Ti_3C_2T_x$ MXene pressure sensors are integrated in the form of a tattoo.[412] This device features laser-patterned $Ti_3C_2T_x$ zigzags sandwiched between PDMS elastomers. Pulse rate, respiration rate and surface electromyography could be monitored with high accuracy. In addition to human movement pressure measuring, real-time monitoring of sound wave is demonstrated by a microchannel-confined $Ti_3C_2T_x$ sandwich-type sensor.[413] By controlling the trench height of the fingerprint microchannel, pressure sensitivity of 99.5 kPa^{-1} can be achieved.

As an advanced form of pressure sensors, Jin *et al.* developed highly sensitive $Ti_3C_2T_x$ film as sound detectors and speech recognition (**Fig. 18**d, e).[409] Once an external force or sound waves hit the surface of the film, the MXene sheets slip to produce cracks and gaps between the sheets, leading to a change in the contact area between the MXene sheets or resistance change. Interestingly, the detector could respond to frequency and decibel of sound waves. Long or short vowels and characters of human speech could in this way be recognized (**Fig. 18**f, g).

Gou *et al.* proceeded further to sound source sensing devices comprising $Ti_3C_2T_x$. $Ti_3C_2T_x$ nanoflakes that are deposited onto anodic aluminum oxide and flexible polyimide substrate.[410] The device displayed a high sound pressure level (SPL) of 68.2 dB (f = 15 kHz) and has a very stable sound spectrum output with frequency varying from 100 Hz to 20 kHz. As a demonstration, the MXene film has been integrated into a commercial earphone operating at high frequency (**Fig. 18**h–j). Pristine MXene film is brittle and might break up under harsh mechanical force, thereby limiting MXene's potential for real-life wearable electronics. As a solution, through electrostatic- force-induced layer-by-layer assembly of $Ti_3C_2T_x$ and cationic polyelectrolyte, PDAC, a stable $Ti_3C_2T_x$ multilayer film is obtained.[414] Such a coating can withstand harsh mechanical stress with good reversibility, still retaining a conductivity of 2000 S/m.

7.2.2 Stretchable MXene hybrid for strain sensing

By placing MXene film on elastic substrates, early stage MXene piezoresistors gained a degree of flexibility. Therefore, they can be bended or twisted to be adaptive for deformed sensing environments. However, these devices might not be applicable for stretchable sensors, which is common in extreme working circumstances with large strain. To address this point, interpenetrating network based on MXene functionalized fibers, as well as MXene nanoparticles interconnected nanosheets were developed. Such hybrid sensors can display high stretchability also upon retaining their electrical function under large strain.

The realization of strain sensors with a high gauge factor (i.e. exceeding 100) and a broad strain range remains a difficult task. To solve this issue, a strain sensor made of $Ti_3C_2T_x$ nanoparticle percolated $Ti_3C_2T_x$ nanosheet network has been developed.[415] In such a system, the propagation of strain-induced microcracks has been limited by the interpenetrating network. As a result, the device could be conductive thus operational even under large strain. In absence of strain, $Ti_3C_2T_x$ nanosheets were well connected by the $Ti_3C_2T_x$ particles to form a highly conductive system. Under strain, SEM images revealed newly formed microcracks within the network, which in turn determined huge resistance changes within a wide strain region of 53%.

For strain sensors, a major challenge emerges when both high sensitivity and stretchability are required. Especially, the realization of strain sensors with large strain range and gauge factor remains a difficult task. By employing highly stretchable polyurethane fibers as support, layer-by-layer deposition of silver nanowires MXene layers enabled the fiber strain sensor with gauge factor exceeding 100 and strain range up to 100%.[416] Moreover, a stretchable $Ti_3C_2T_x$ MXene/carbon nanotube-based strain sensor has been devised.[430] This hybrid could be operational between tiny and large strain with a low detection level of 0.1% strain, meanwhile it can be stretched up to 130% and possessed a gauge factor up to 772.6.

Textile-based electronics combine electronic components with clothes to realize the critical functions such as sensing, energy harvesting and its storage. Uzun *et al.* reported knittable and washable $Ti_3C_2T_x$ MXene coated cellulose yarns [418]. Electrodes made from the yarns provided a high capacitance of 759.5 mF cm^{-1}. Seyedin *et al.* described $Ti_3C_2T_x$ MXene/polyurethane (PU) composite fibers exhibiting both the high conductivity and high stretchability with a strain range of 200%.[419] When it was used as a strain sensor, the MXene/PU composite fibers showed a high gauge factor of ≈ 12900. Strain sensor with similar composition based on $Ti_3C_2T_x$ nanosheets loaded PU mat has reported.[420] The device is characterized by high gauge factor up to 228, a low limit of detection down to 0.1% and wide strain range of 150%. Besides as strain sensors, pressure sensors using Ti_3C_2Tx-cotton textile has been demonstrated.[421] Due to the wavy surface of cotton textile, the pressure sensor displayed a sensitivity of 12.095 kPa^{-1} for the range from 29 to 40 kPa.

7.2.3 3D-microstructured MXene network for ultrasensitive pressure sensors

High-performance pressure sensors garner widespread attention due to the potential applications in human-machine interaction and wearable electronics. However, most of flexible pressure sensors need sophisticated nanostructure design, thus involving a cumbersome manufacturing process. Obviously, a large-scale and low-cost technology would be highly desirable for the fabrication flexible pressure sensitive materials with high sensitivity in a broad pressure range. To achieve a high-pressure sensitivity, an MXene-sponge has been fabricated by dip-coating sponge in $Ti_3C_2T_x$ suspension and drying.[422] The pressure sensor based on MXene-sponge displayed high sensitivity over a wide pressure range (147 kPa^{-1} for pressure below 5.37 kPa, and 442 kPa^{-1} within 5.37-18.56 kPa).

A MXene strain sensor with nacre-mimetic microscale "brick-and-mortar" architecture has reported.[423] The sensor is fabricated by screen-printing an ink formulation of four components, $Ti_3C_2T_x$, dopamine, nickel (II) and silver nanowires. The bioinspired sensor showed a gauge factor exceeding 200 and operational strain range up to 83%. Notably, the gauge factor is found to increase under large strain region, reaching a maximum of 8700 (77%-83%).

As an emulation of human skin, Wang *et al.* described a highly deformable pressure sensor.[424] It is made up of $Ti_3C_2T_x$/natural microcapsule (NMC) biocomposite films (**Fig. 20**a). The pressure sensors featured a multi-layered structure, bearing resemblance to epidermis, dermis and subcutaneous tissue to human skin (**Fig. 20**b). With the interlocking configuration of microcapsule, the device displayed an elastic modulus of 0.73 MPa, enabling to be operational even under harsh deformation. Such flexible sensor showed a sensitivity of 24.63 kPa^{-1}.

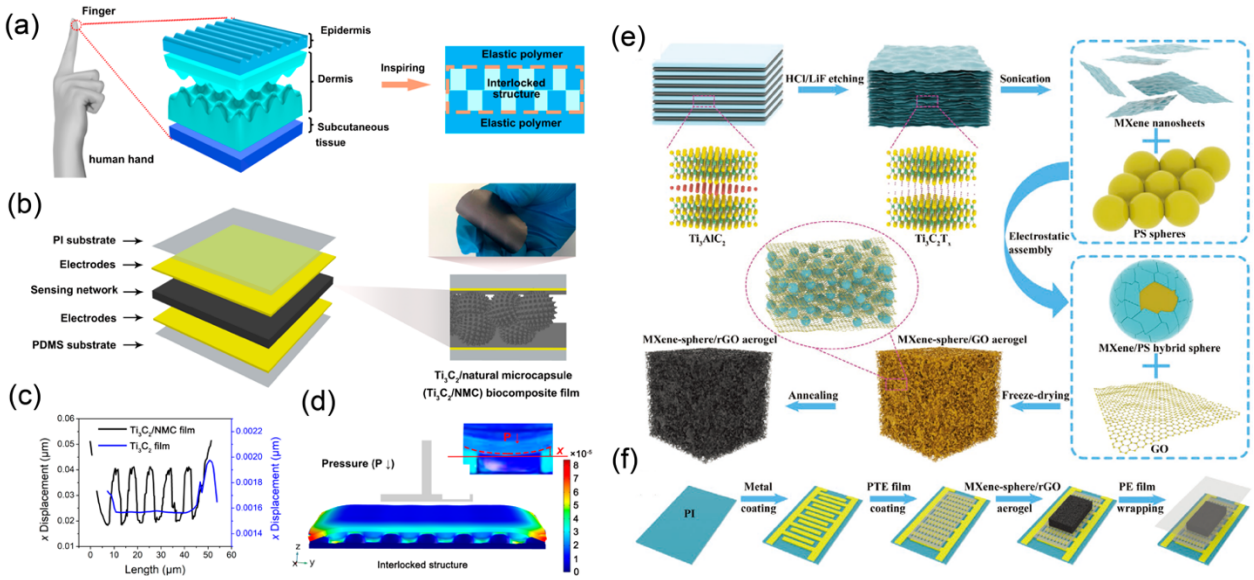

Fig. 19. Proposed concept of interlocking structure to simultaneously achieve high deformability. (a) Diagram illustrating the structure of human skin; inspired by it, sensing

materials are fabricated between the two elastic polymers to form the interlocking structure. (b) Schematic diagram of the flexible sensor. Inset shows an enlarged image of interlocking structure and optical image of flexible sensing biocomposite film. (c) Relationship of deformation distance (x) and applied force (P) performed by FEM analysis for the biocomposite film (black line) and flat film (blue line). (d) Cross-sectional view of FEM of the deformation distribution in biocomposite film with interlocking structure. Reprinted with permission from ref. [424]. Copyright 2019 American Chemical Society. (e) Schematic illustration of the preparation procedures of rGO/MXene-sphere aerogel. (f) Schematic illustration of the fabrication process of MXene sphere/rGO aerogel based piezoresistive sensor. Reprinted with permission from ref. [425]. Copyright 2020 Wiley.

Zhu *et al.* reported a piezoresistor based on a reduce graphene oxide (rGO), $Ti_3C_2T_x$ and polystyrene (PS) sphere hybrid (**Fig. 19**e).[425] Ultrahigh sensitivity of 609 kPa^{-1} and a low detection limit of 6 Pa could be achieved.

Inspired by the hydrogen bonding interactions of amino acids, a self-healable MXene-rubber composed of $Ti_3C_2T_x$ and epoxidized natural rubber (ENR) microspheres has been proposed.[426] The ensuing hybrid can endure strain up to 400% and display a gauge factor of 107.43, a low strain detection limit of 0.1%.

By mimicking human skin, a $Ti_3C_2T_x$ piezoresistor with a microspinous structure has been realized by abrasive paper stencil printing.[427] These $Ti_3C_2T_x$ microspines are used to mimic the microstructural mechano-receptors. The obtained pressure sensor displayed high sensitivity 151.4 kPa^{-1} and low detection limit of 4.4 Pa.

In addition to printed MXene microspines, a $Ti_3C_2T_x$ papillae array has been produced by deposition of MXene on thermally-deformable substrates with pre-patterned via-holes.[428] Resultant papillae-MXene/elastomer hybrid exhibited a sensitivity of 11.47 kPa^{-1} and it was able to monitor human motions such as breathing, heartbeats and pronunciation of words.

7.2.4 MXene-based hydrogel and aerogel for pressure and strain sensors

A hydrogel represents a network of cross-linkable hydrophilic polymers; since the polymers can absorb large amount of water as filler, a hydrogel is generally soft, elastic, and biocompatible with human body. Conductive components containing hydrogel are advantageous due to their large strain tolerance without undergoing mechanical break-down. As a matter of fact, MXene-hydrogel systems have emerged in recent literature for wearable strain and pressure sensors. Alongside, aerogel has also been explored for ultralightweight and ultrasensitive pressure sensors. Aerogel is distinctive from hydrogel: the former features a 3D network with a porous architecture, with the pores being occupied by air. Therefore, an aerogel is extremely lightweight and compressible. This property allows it to produce high magnitude of volume resistance change upon pressure, thus making it suitable for highly sensitive pressure sensors.

A hydrogel composites incorporating MXene ($Ti_3C_2T_x$) in polyvinyl alcohol (PVA) with unprecedented performance as strain sensor was described.[431] The hydrogel device showed high strain sensitivity with a gauge factor of 25 and a stretchability reach up to 3400%. Direction and speed of motions can be simultaneously monitored by the MXene hydrogel.

A piezoresistive sensor based on ultralight and superelastic aerogel has been reported.[432] The sensing component is made up of MXene/reduced graphene oxide (MX/rGO) with a hybrid 3D structure. This piezoresistive sensor based on the MX/rGO aerogel showed high sensitivity of 22.56 kPa^{-1} and it was able to detect pressure signals with amplitude below 10 Pa. Moreover, a $Ti_3C_2T_x$ MXene/polyimide aerogel has been proposed.[433] The resulting lightweight (8.9 mg cm^{-3}) aerogel displayed elasticity, stress-strain at 50% strain and compressive stress-strain up to 80%.

Zhang *et al.* reported a stretchable and self-healable MXene/PVA hydrogel for capacitive-type electronic skin.[434] The hydrogel can withstand a maximum of 1200% strain before undergoing break-down and a minimum of 0.15 s for self-healing. Capacitive sensors thereof output signals with high linearity with strain reaching 200%. showed high linearity, up to 200%, low hysteresis, a sensitivity of 0.40.

Poly(N-isopropyl acrylamide) has been employed to fabricate MXene hydrogels.[435] This composite hydrogels showed excellent mechanical properties with a maximum strain up to 1400% and a 0.4 MPa tensile strength.

An MXene-organhydrogel comprising $Ti_3C_2T_x$, polyacrylamide, PVA and crosslinkable borax has been reported.[436] Due to strong borate bonds and hydrogen bonding, the hydrogel can withstand a strain range up to 350% and a gauge factor of 44.85.

An aramid nanofiber/$Ti_3C_2T_x$ MXene aerogel has been demonstrated with high robustness.[437] This hybrid aerogel possessed a "mortar–brick" porous structure with a low density of 25 mg/cm^3. Moreover, it exhibited a wide compressive strain range from 2.0% to 80.0%, sensitivity up to 128 kPa^{-1} and low detection limit of 100 Pa.

Emulation of human skin requires mechanical robustness, fast response and high sensitivity under strain. A hydrogel composites incorporating MXene ($Ti_3C_2T_x$) with unprecedentedly performance as strain sensor has been described.[438] The hydrogel device showed high strain sensitivity with a gauge factor of 25 and a stretchability reach up to 2800%.

7.3 MXene for biosensing utilities, electrochemical sensors, fluorescence imaging and biosensing platforms.

As a simple but effective platform for chemical sensing, chemiresistors based on MXenes have been exploited for the sensing of gas molecules, as previously discussed Upon sensing more complicated chemical systems such as biomolecules, chemiresistors are expected to suffer from a poor selectivity. To overcome this problem, MXene-based electrochemical sensors have been developed. There are two major strategies: (1) by using MXene as electroactive working electrode (WE) for electrochemical process, and (2) by employing MXene as conductive channel

for electrochemical transistors (OETs). Since most electrochemical sensors are used under aqueous conditions, the analytes bearing ionic groups can be driven to adsorb on the MXene surface or intercalate in-between the MXene layers. Both processes alter the electronic properties of MXenes WE, such as work function and conductivity, and they will contribute to changes of current density. As an advanced technology, biomolecular aggregates such enzymes and DNA can be functionalized on the surface MXene, enabled chemically or bio-modified MXene electrodes as a powerful platform to detect traces amount of specific analytes. For electrochemical sensors, a general protocol relies on the functionalization of electrodes with MXene due to its high conductivity to transmit current flow. Taking advantage of the abundant surface terminations of MXene, functional materials can be anchored to MXene surface, thus enabling the occurrence of strong intermolecular interactions with the analytes of choice. More generally, the incorporation of MXene into electrochemical sensing substantially broadens the application range of MXene chemical and bio-sensing. Quantum dots (QDs) and nanoparticles are a class of nanomaterials with good optical properties. For example, due to the quantum confinement effect, the bandgap and absorption wavelengths of QDs can be tuned by particle size. Still, chemical functionalization of QDs can also alter their energy levels to change their light-emission properties. With these advantages, QDs made of MXene are investigated as fluorescent probes for chemical and biosensing systems. In the following section, MXene-based bioelectronics is surveyed.

7.3 MXene for electrochemical sensors.

7.3.1 MXene-based electrodes for electrochemical sensing of biomolecules

Dopamine sensing has emerged as a critical topic in biochemistry. It is a neurotransmitter that enables the communication in the nervous system and controls the human behavior. Therefore, the monitoring of dopamine concentration is key to probe neural activities. An electrochemical field-effect transistor with a $Ti_3C_2T_x$ channel has been exploited for dopamine sensing (**Fig. 20**a, b).[439] The pristine transistor displayed ambipolar transport properties and its drain current increased upon the addition of dopamine, indicating the *p*-doping effect of dopamine to give a linear dopamine detection range from 0.1 to 50 μM (**Fig. 20**c, d). Conventional electrochemical cell using MXene/DNA/Pd/Pt has been exploited as dopamine sensors.[440] As a result, electrochemical sensing of ascorbic acid, uric acid and glucose has been successfully carried out.

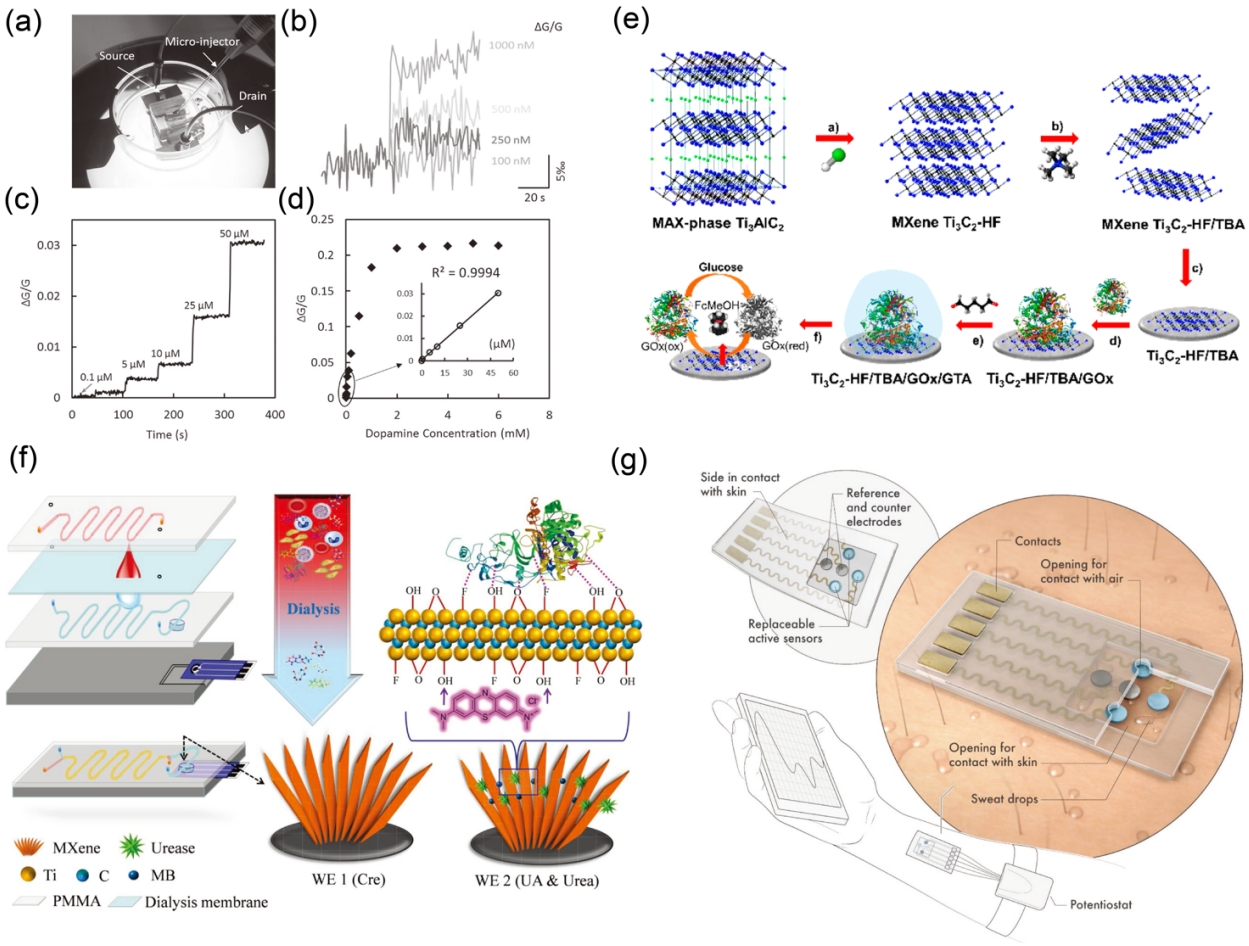

Fig. 20. Electrochemical sensors based on MXene electrode. Dopamine sensing with the MXene–FET: (a) Photograph showing the MXene–FET coupled with a micro-injector for precisely controlled pulsed releasing of dopamine in the biosensing chamber. (b) Recordings of the conductivity variation of the MXene device upon addition of dopamine. (c) Real-time monitoring of conductivity fluctuations of an MXene device under different dopamine concentrations. (d) Analysis of the dopamine detection range of the MXene–FET. The inset shows a highly linear modulation of the device conductivity under different dopamine concentrations. Reprinted with permission from ref. [441]. Copyright 2016 Wiley. (e) Schematic Illustration depicting the procedures of MXene electrodes for glucose sensing. Exfoliation of Ti_3AlC_2 to generate Ti_3C_2–HF. Then, Delamination of Ti_3C_2–HF with TBAOH to yield Ti_3C_2–HF/TBA; Construction of the proposed glucose sensing System by modifying the GCE with Ti_3C_2–HF/TBA. Followed by loading of Glucose Oxidase (GO_x) and subsequent cross-linking glutaraldehyde (GTA) with GO_x. Reprinted with permission from ref. [442]. Copyright 2020 American Chemical Society. (f) Schematic illustration of fabrication of MXene-enabled microfluidic chip. It consists of four layers. The channel in the top layer is set aside for blood flow and the second layer is a dialysis membrane that allows penetration of molecules smaller

than 1000 Da, like urea, UA, and Cre. The third layer possesses the flow channel for isotonic solutions and the detection chamber. The analytes in blood can be dialyzed into this channel and accumulated in the detection chamber, and the sensing electrode in the bottom layer can capture these targets and generate signals. Reprinted with permission from ref. [443]. Copyright 2019 Wiley. (g) Schematic diagram of the sensor system for in vitro perspiration analysis. It has a skin-conforming and stretchable design, which enables conformal contact with the skin for efficient sweat collection and high performance under physical deformation. All active sensors (glucose, lactate, and pH) along with the counter electrode and reference electrode are placed in independent and replaceable modules. Reprinted with permission from ref. [444]. Copyright 2019 Wiley.

Being an analogue to dopamine, adrenaline is a molecule associated with heart rate increase, stress and anxiety. A Ti_2C MXene/graphite composite paste electrode electrochemical sensor has been fabricated for the detection of adrenaline.[445] This sensor displayed a sensitive response to adrenaline, being much higher than the bare graphite electrode. Adrenaline from concentration of 0.02-100 μM could be detected, giving two linear regions.

Organophosphorus pesticide residual should be accurately monitored due to its toxicity even at low concentration. To solve this challenge, MXene nanosheets functionalized with Au-Pd bimetallic nanoparticles have been employed as enzymatic biosensor for paraoxon detection.[446] This biosensor exhibited a linear response to paraoxon with the concentration from 0.1 to 1000 μg L^{-1} and a low detection limit of 1.75 ng L^{-1}.

Detection of L-cysteine is critical for early diagnostics of cardiovascular diseases. An electrochemical sensor based on Pd/ $Ti_3C_2T_x$ MXene functionalized glass carbon electrodes has been fabricated [447] where $Ti_3C_2T_x$ performed as a conductive matrix. This sensor afforded a linear response within a L-cysteine concentration ranging from 0.5 μM to 10 μM.

In addition to simple amino acid sensing, electrochemical sensors based on MXene has also been applied to complex proteins. Osteopontin is a highly phosphorylated protein that is fundamental for the formation of mineralized extracellular matrices (ECMs) of bones and teeth. A substrate made of $Ti_3C_2T_x$ and phosphomolybdic acid is prepared, on which a conductive polymer such as polypyrrole is *in-situ* polymerized.[448] Due to its high sensitivity to osteopontin, the tri-component-based aptasensor displayed an ultralow detection limit of 0.98 fg mL^{-1}.

Zhang *et al.* put forward a novel ratiometric electrochemical platform based on MXene for piroxicam sensing.[449] Using the piroxicam as the detected molecules, the methylene blue/Cu nanoparticles/$Ti_3C_2T_x$ decorated GCE displayed enhanced repeatability over the non-reference device with the detection limit of as low as 0.1 μM.

7.3.2 MXene for electrochemical sensing of glucose

In absence of insulin, diabetes lead to high glucose concentration in the patients' blood. Therefore, sensitive and real-time monitoring of glucose concentration is vital for the limitation of diabetes. In common electrochemical sensing of glucose, glucose oxidase (GO_x) has been employed as enzymatic basis, which catalyzes the oxidation of glucose to gluconolactone in the presence of oxygen to yield H_2O_2. By measuring H_2O_2 concentration, glucose concentration can be stoichiometrically obtained.[450]

Due to its high specific surface area and high conductivity, MXene can serve as a conductive channel to anchor GOx to the electrode for sensing utilities. For example, an electrode based on Au/MXene nanocomposite is explored for glucose sensing.[451] The system displayed a linear amperometric response in the glucose concentration range from 0.1 mM to 18 mM with a high sensitivity of 4.2 μA mM^{-1} cm^{-2} and a detection limit of 5.9 μM. To further enhance the interaction between GO_x and GCE, a 3D porous network of $Ti_3C_2T_x$ /graphene has been developed.[452] Its glucose sensitivity and detection limit of this 3D porous system outperformed that of 3D graphene films.

In **Fig. 20**e, a glucose biosensor is depicted by deposition of $Ti_3C_2T_x$ on GCE, followed by coating of GO_x crosslinked by glutaraldehyde.[442] By chronoamperometric tests, as-fabricated biosensing system exhibited linear response in a wide range from 50 μM to 27750 μM and a low detection limit of 23 μM.

7.3.3 MXene electrochemical sensors for superoxide sensing

Hydrogen peroxide and superoxide radical anions are critical substances in biological functions, such as cell signaling and immune responses. Since these compounds oxidize other biomolecules, they can damage intracellular environments. Therefore, the real-time monitoring and elimination of these compounds is critical for ensuring a good health to humans. To detect the superoxide anions in HepG2 cells, a novel MXene-based biomimetic enzyme was synthesized.[453] The sensor displayed a sensing range from 2.5 nM to 14 μM and a low detection limit of 0.5 nM. Real-time monitoring of superoxide released from HepG2 cells is successfully accomplished.

To enable cost-effective superoxide sensors, noble metal nanoparticles (Au, Pd and Pt) have been functionalized on the surface of $Ti_3C_2T_x$ to perform as catalysts.[454] Upon stepwise increase of superoxide anion concentration, the current density in the electrochemical biosensor increased linearly within a concentration range from 0.4 to 9.5 μM and detection limit of 0.2 μM. Moreover, extracellular real-time monitoring of superoxide released from zymosan-stimulated HepG2 cells has been carried out.

7.4 MXene as blood and perspiration sensors

The human sweat is primarily composed of water with small amounts of sodium, potassium, calcium, and magnesium ions, metabolites (lactate, ammonia, and urea) and unmetabolized pharmaceutical drugs. Real-time monitor of human sweat is helpful to obtain the individual's health condition without invasive sampling.

Electrochemical immunoassay of prostate specific antigen has been performed by PEDOT modified 3D sodium titanate nanoribbons.[455] This PEDOT/titanate hybrid displayed a high specific surface area and fast electron transport capability as electrodes. Differential pulse voltammetry showed an antigen sensing range from 0.0001 μg ml^{-1} to 20 μg L^{-1} and an ultralow detection limit of 0.03 pg L^{-1}.

In **Fig. 20**f, $Ti_3C_2T_x$ displayed electrocatalytic property and is screen-printed as an electrode integrated with a dialysis microfluidic chip for the purpose of nalysis of whole blood.[443] This MXene based sensor has been applied as on-line continuous monitoring of uric acid, urea and creatine in human blood.

An aqueous MXene ink is developed for inkjet-print MXene films for on wearable electrocardiography recording and human sweat analysis.[456] As-proposed skin-conformal MXene electrodes detect electrocardiography signals with high signal-to-noise ratio and long shelf life. Furthermore, the inkjet-printed $Ti_3C_2T_x$ electrode can perform as a biosensor to on-line monitor the concentration of sodium ion with a sensitivity of 40 mV per decade and interferon gamma (as an immune biomarker) with a sensitivity of 3.9 mV per decade.

A MXene-based wearable biosensor system for in vitro perspiration analysis has been reported.[444] The key component is a hybrid of MXene/Prussian blue composite that is designed to detect concentration of bio-markers, such as glucose and lactate from sweat. A modular design allows a simple exchange of the specific sensing electrode to target the desired analytes, as demonstrated in **Fig. 20**g. Furthermore, the device is designed to be equipped openings for air supply, rendering unlimited oxygen for the active layer to facilitate its enzymatic activities. As a result, typical electrochemical sensitivities of 35.3 μA mM^{-1} cm^{-2} for glucose and 11.4 μA mM^{-1} cm^{-2} for lactate are obtained from artificial sweat.

7.5 MXene for inorganic chemical sensing

Besides the aforementioned biomolecular analytes, inorganic molecules sensing by means of MXene has been investigated where hemoglobin is immobilized on the surface of $Ti_3C_2T_x$ towards a mediator-free biosensor for nitrite.[457] $Ti_3C_2T_x$ proved to be an excellent immobilization matrix to be biocompatible hemoglobin, enabling the redox activity of hemoglobin. Due to the large surface area and the high conductivity of $Ti_3C_2T_x$, the electrocatalytic reduction of nitrite using hemoglobin is enhanced to afford a wide linear range of 0.5–11800 μM and a low detection limit of 0.12 μM.

$Ti_3C_2T_x$ MXene quantum dots have been studied as a fluorescence marker to detect the Fe^{3+} concentration.[458] As-synthesized quantum showed a fluorescence quantum yield value of 7.7%. Such fluorescence could be suppressed by Fe^{3+}. This is due to redox reaction of Fe^{3+} and Ti^{2+} from $Ti_3C_2T_x$. Based on this observation, a fluorescence method for Fe^{3+} detection based on MXene quantum dots has been developed with high sensitivity and selectivity over other metal cations.

7.6 MXene for fluorescence sensing and imaging

Photoluminescence $Ti_3C_2T_x$ quantum dots (QDs) have been synthesized for multicolor cellular imaging.[459] By controlling the hydrothermal temperature, the size of $Ti_3C_2T_x$ QDs can be tuned. Due to the strong quantum confinement effect, as-prepared QDs showed quantum yield of 10% from photoluminescence (PL) spectroscopy and low cytotoxicity to the cells. Hence, they are subjected to multicolor cellular imaging to label RAW264.7 cells. The fluorescence and biocompatibility of MXene QDs allow potential biochemical and optical utilities. MXene QDs are employed for metal ion sensing.[460] Nb_2C QDs displayed a quantum yield of 8.4% and intensified PL emission peaks under high pH region, allowing pH sensing. Moreover, significant fluorescence quenching is observed when Fe^{3+} ions are added to Nb_2C QDs, leading to a linear sensing range from 0 to 0.3 mM. It is the charge transfer from Nb_2C QDs to the Fe^{3+} that might be responsible for this quenching phenomenon.

Due to the low cytotoxicity of $Ti_3C_2T_x$ QDs, they have been investigated as ratiometric fluorescent sensors for intracellular pH sensing.[461] Functionalization of such QDs are performed by polyethylenimine coating and then coordination of $[Ru(dpp)_3]Cl_2$, leading to a quantum yield of 7.13%. The change of pH values leads to either protonation/deprotonation of the Ti_3C_2 QDs. With the deprotonation of Ti_3C_2 QDs, a part of valence electrons would be localized and they cannot participate in photoabsorption, leading to decreased absorption. Hence, the absorption intensity of Ti_3C_2 QDs depends on pH values and this phenomenon is applied to pH sensing.

A $Ti_3C_2T_x$ nanosheets based nanoprobe has been developed to fluorescently detect phospholipase D activity.[424] $Ti_3C_2T_x$ is modified with rhodamine B labelled phospholipid as a fluorophore. The molecular stacking of Rhodamine B and $Ti_3C_2T_x$ leads to efficient fluorescence quenching of rhodamine B by energy transfer. Due to the lipolysis of phosphodiester bond catalyzed by phospholipase D, rhodamine B is removed away from the $Ti_3C_2T_x$ surface to regain its fluorescence. By this methodology, phospholipase D can be determined with a detection limit of 0.10 U L^{-1}.

Exosomes present non-invasive biomarkers to diagnose diseases such as cancers. A $Ti_3C_2T_x$-based ratiometric fluorescent sensors have been proposed to detect exosomes level.[462] The MXene nanosheets are modified by a unique Cy3 labeled CD63 aptamer towards a ratiometric

fluorescence resonance energy transfer (FRET) nanoprobe. The Cy3-CD63 aptamer adsorbed onto the surface of $Ti_3C_2T_x$ underwent fluorescence quenching due to the FRET between the Cy3 and MXenes. Based on this fluorescent sensor, the detection limit of exosome reached 1.4×10^3 particles mL^{-1}.

Taking advantage of the inner filter effect, $Ti_3C_2T_x$ QDs have been studied as fluorescent probes for the alkaline phosphatase (ALP) assay and embryonic stem cell (ESC) identification.[463] The absorption spectra of *p*-nitrophenol is found to overlap with (p-NP) the emission spectrum of $Ti_3C_2T_x$ QDs. Being a product from ALP-catalyzed dephosphorylation of *p*-nitrophenyl phosphate (**Fig. 21**a), *p*-nitrophenol induced the fluorescence quenching of $Ti_3C_2T_x$ QDs through the inner filter effect (**Fig. 21**b, c). Hence, the concentration of ALP can be deduced from the PL spectra of $Ti_3C_2T_x$ QDs and its detection limit reached 0.02 U L^{-1} (**Fig. 21**d, e).[463]

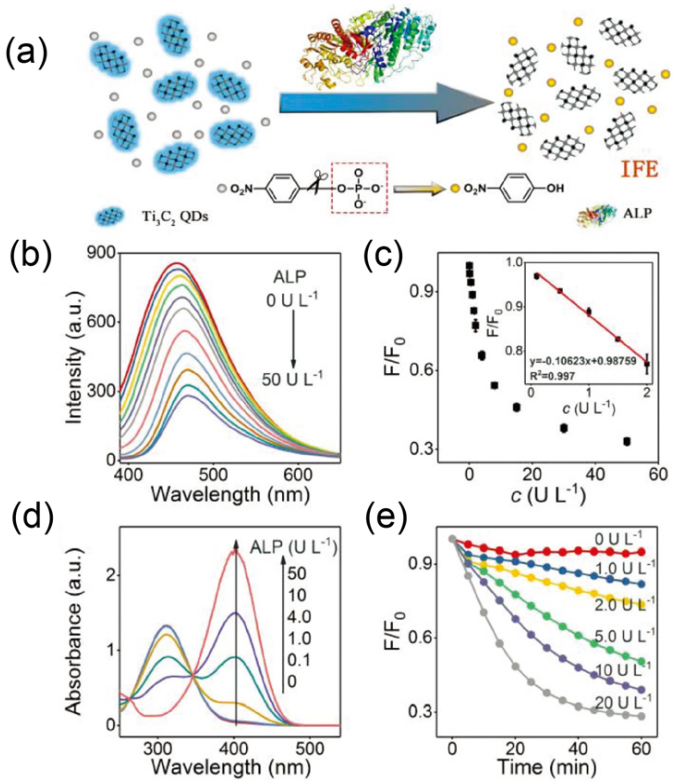

Fig. 21. (A) Schematic illustration of the Ti_3C_2 QD-based fluorescence assay for ALP activity. (B) Fluorescence emission spectrum of Ti_3C_2 QDs in the presence of different concentrations of ALP with 200 μM p-NPP. (C) Plots of fluorescence response (F/F0) versus ALP concentration (inset: the linear relationship from 0.1 to 2.0 U L^{-1}). F0 and F are the fluorescence intensities of Ti_3C_2 QDs in the absence and presence of ALP, respectively. (D) Absorbance spectrum of the enzymatic reaction solution upon addition of various concentrations of ALP from 0.1 U L^{-1} to 50 U L^{-1} with 200 μM p-NPP. (E) Time-dependent fluorescence response curves at 450 nm obtained

for ALP of different concentration. Reprinted with permission from ref. [463]. Copyright 2018 Royal Society of Chemistry.

A $Ti_3C_2T_x$ QD-encapsulated liposomes for photothermal immunoassays of prostate-specific antigen (PSA) has been reported. [464] $Ti_3C_2T_x$ QDs converted NIR photons into heat to upshift the system temperature, which is in proportion to the analyte concentration. When it is applied to PSA sensing, a linear range from 1.0 ng mL^{-1} to 50 ng mL^{-1} and a limit of detection of 0.4 ng mL^{-1} has been demonstrated. Herein, nitrogen-doped $Ti_3C_2T_x$ QDs have been synthesized for fluorescence detection of H_2O_2 and xanthines. As-prepared $Ti_3C_2T_x$ QDs are doped with 2,3-diaminophenazine as a form a hybrid nanoprobe. [465] Based on the photoinduced electron transfer effect, electrons would be extracted from $Ti_3C_2T_x$ QDs to be accepted by 2,3-diaminophenazine. The addition of H_2O_2 would quench the fluorescence of MXene QDs, meanwhile strengthen the fluorescence of 2,3-diaminophenazine, thereby forming a correlation of H2O2 concentration with change of fluorescence intensity. The interaction between $Ti_3C_2T_x$ MXene multilayers with fluorophore-tagged DNA are elucidated by fluorescence measurements.[466] Fluorophore-tagged DNA can be captured by MXene via electrostatic forces. however, due to the close proximity of DNA and MXene, fluorescence intensity is quenched. Due to the capture/release of DNA from MXene, the fluorescence intensity can be varied. This observation can be potentially utilized to quantitively detect DNA at picomole levels.

7.7 MXene for electrogenerated chemiluminescence (ECL) detection of biomolecules

In addition to direct measurement of fluorescence intensity of MXene-based biosensing system, electrogenerated chemiluminescence sensing of biomolecules have been investigated. In such a system, analytes formed contact with MXene-incorporated working electrodes. Upon the application of voltages, the electrode would generate chemiluminescence for the qualitative and quantitative analysis.

An aptamer modified $Ti_3C_2T_x$ nanosheets as the ECL nanoprobe has been demonstrated.[467] The exosomes can be highly efficiently adsorbed onto the electrode surface by the EpCAM-protein-recognizing aptamer modified on GCE. With the addition of Aptamer2 functionalized MXene, ECL is generated for quantitative detection of exosomes. Thus, sensitive ECL biosensor for MCF-7 exosomes detection is attained with a detection limit of 125 particles μL^{-1}.

With a similar strategy, gold nanoparticles (AuNPs) decorated $Ti_3C_2T_x$ MXene/aptamer hybrid have been modified on electrodes for ECL sensing of exosome. In such an electrochemical system, the exosomes can be readily captured by aptamer immobilized on the electrode.[468] *In-situ* formed AuNPs MXenes-Apt hybrid can enhance the ECL signal of luminol. The detection limit of exosomes from Hela cells is 30 particles μL^{-1}.

$Ti_3C_2T_x$ nanosheets have been integrated with carbon nitride nanosheet (CNNS) decorated amino-functional metal−organic frameworks for the assay of cardiac troponin I.[469] Due to the

reductive property of MXene, persulphate can be converted into sulfate anion radicals, which react with carbon nitride nanosheet to enhance the ECL signals. A low cardiac troponin I detection limit of 0.38 fg mL^{-1} is obtained by this system.

7.8 MXene as electrode array for recording of physiological signals

In the aforementioned electrochemical sensors, MXene and its hybrid composite can be used as electrodes to induce electrochemical redox reactions with analytes. Most recently, they are investigated as electrode array in the bio-interface to probe the physiological signals. Especially, due to the flexibility and low cytotoxicity of MXene scaffold, they can be conformal to both skin and organs for the real-time signal monitoring.[470, 471]

A high-throughput microfabrication process has been developed for $Ti_3C_2T_x$ electrode array.[470] Photolithography patterned $Ti_3C_2T_x$ electrodes displayed low interface impedance than conventional metal electrodes. Neuroelectronic devices made of $Ti_3C_2T_x$ have been applied to signal recording in contact with brains of anesthetized rats, showing lower noise and reduced susceptibility. Moreover, $Ti_3C_2T_x$ displayed a biocompatibility with neurons to extend neurites and facilitate the formation of their networks. To enable the monitor of electric signals from the human skin or surface electromyography (EMG), a gel-free $Ti_3C_2T_x$-Based electrode array has been proposed.[471] Conformal $Ti_3C_2T_x$ electrodes are photolithographically patterned to form intimate contact with the skin. Due to the high conductivity and conformity of MXene electrodes, they could record EMG signals with high-fidelity and low noise, being superior to conventional metal electrodes.

Summary and outlook

The present review dealt with the emerging challenges and opportunities from the technological viewpoint wherein physical properties with latest developments have been deliberated. The first section reviewed the state-of-art investigations on the MXene-based optics and nanophotonics, as well as the performance of their corresponding functional devices. The richness of chemical compositions and surface terminations, as well as the variation of stacking numbers *n*, warrants MXene materials with distinct and highly tailorable optical properties. The applications resulting from the MXene's optical properties have quickly spread from highly transparent optoelectronics, solution-processable white light emission ink, to femtosecond laser generations and highly efficient energy transformations. Despite the brilliant progress made, there are still multiple longstanding hurdles that need to be overcome.

There is a biggest discrepancy between the theoretically predictions and experimental confirmations. For example, while many MXenes can be expected to be semiconducting with direct bandgaps that feature characteristic absorption and emission, hitherto only a few have been demonstrated. The surface function species and their dangling bonds induced DOS redistribution, as well species the crystal parameter changes via ion catalations are present

during the wet acid etching synthesis, however, their influence on the optical properties is not fully understood. Many reports have shown ultra-high optical transmittance (~98%) of MXene films or nanosheets, while the linear optical transmission of monolayer MXenes is still under debate, especially if one considers that MXene has a thickness that is at least triple than monolayer graphene. Most of the experimental investigations requires the synthesis of large-scale monolayer MXenes without or with controllable surface functions that are still rarely been reported. The reports on the nonlinear optics in MXene are limited and are mainly concerning the saturable absorption (or reverse saturable absorption). The light-many-body complexes (trions, biexcitons) interactions in MXene, especially in heterostructures are barely been touched. MXenes are poised to be an excellent plasmonic nanoplatform due to their large DOS density at the Fermi surface contributing from the transition metals, are promising to manipulate light for optical communication, solar energy harvesting and biomedical/molecular sensing still in its infancy stage. The selective excitation and guiding plasmonics in MXene have been considered. MXene based photothermal conversion has attracted a big deal of attentions from water desalinations and medical treatments. However, the mechanisms and processes of photon-phonon transfer in MXene is still elusive. Thanks to the high electron conductivity and tunable work functions, MXenes have found broad applications in photocatalysis, photodetecting and solar cells. Nevertheless, the role of MXene in these applications is controversial.

Solving the above-mentioned challenges not only significantly promotes the standing explorations, but also opens many new opportunities. Here, we have listed a few foreseeable exciting directions that wish to provide a helpful guide for the future research explorations. As the synthesis of MXene via chemical vapor deposition (CVD) or chemical transformations have been demonstrated [71], high quality large scale MXene monolayer or few layer samples are tangible. Basic physical and chemical properties of monolayer MXene, e.g. linear optical transmission and superconductivity, are expected to be systematically investigated soon. MXene heterostructures are less investigated and the light-matter interactions (e.g. exciton-polaritons) in MXene cavity have not yet entered the viewfield of researchers. The richness of MXene members and surface terminations allow the formation of editable MXene heterostructures and Janus architectures. Furthermore, it has recently been reported that the optoelectronics can be large changed by stacking two monolayer graphenes at a magic angle to form 2D Moire patterns, and has quickly spread to TMDs materials. Stacking angle tuning optoelectronics in MXene materials has no report to date, and may trigger another research upsurge. Additional opportunity lies in the epsilon-near-zero (ENZ) optical frequency range, in which infinite large optical nonlinearities, decoupling of electricity and magnetism, and enhanced local electric field can be obtained. Several experimental results have revealed that the ENZ wavelength of MXenes located at 1100 to 1300 nm, which can be easily delivered by current laser sources. Though the optical related properties like photothermal conversion,

photoelectrochemistry, photodetecting have been wide and deeply explored, the opto-magnetic properties of MXenes still reside in theory. Bridging the theoretically predictions and practical optomagnetic performance may be beneficial for diverse applications ranging from optical manipulations, to high density data storage and magnetoencephalography. The synergistic performance of different merits, e.g. opto-electro-magnetical and opto-electro-mechanical, are preferable for integrated nanodevices and have not been investigated. Finally, the feasibility of solution processable MXene inks and composites warrants the utilization of additive manufactures, e.g. 3D printing, to realize complex and multifunctional MXene based devices that is coming on the stage.

Taking into consideration the above meagre research efforts, still a lot of investigations are beseeched in order to practically estimate the mechanical properties; the hindering hurdles such as the limitations of the present characterizing tools/facilities, the lack of control on the compositions and functionalization groups, nano- or micro-structural voids, vacancies or defects, unknown non-linear phenomena, and the weak MXene-matrix interfacial strength in MXene-based MMCs must be rigorously addressed. As mentioned, AFM nano-indentation has only been to date a practical characterization tool for a series of MXenes; however, still a lot of experimental techniques need to be explored for characterizing mechanical and tribological aspects. As a result, still new methods with more consistent, controllable and reliable outcomes should be developed. The elastic property of MXene sheets have been tested either through computational activities or experiments; however, still virtually nothing is reported regarding the plastic deformation behavior of MXenes, owing mostly to the lack of information, knowledge and understanding on the MXene flakes. It is believed that MXene sheets have different response under different loading conditions; moreover, those linear and non-linear underlying deformation mechanisms should be clarified. For instance, the effect of heat and temperature being the two important factors influencing the mechanical and tribological behavior has not yet been fully studied. There are also a lot of open questions regarding the deformation behavior under varied pressure levels or even under different environmental conditions. The stability and performance of MXenes under different loading and environmental conditions (such as corrosive environment) are almost unknown in industrial applications. Those issues such as degradation over the time, particle breakage, agglomerations, oxidation in different media, change under elaborated temperatures or pressures, possible reactions among MXene sheets, as well as those structural defects are yet to be characterized in real applications. Advanced material characterization setups should be developed and employed to study the dispersion and agglomeration state as they tend to change with time. Further investigation is demanded to further grasp the effect of flake size (lateral, thickness), termination group type(s), process parameters, etc. on the mechanical and tribological features of MXene-based systems. The interactions between MXene nanosheets within the composite systems need further investigations. Last but not least, it is obvious that the knowledge and

information in this field are insufficient and further research efforts, not only on computational studies but also on practical examinations must be conducted to delineate the effects of different playing role parameters such as thickness, temperature, loading conditions, materials variables, etc. on mechanical properties.

The search for 2D magnetic materials, which are desirable for nanosized spintronic devices, is a longstanding goal that has been significantly promoted via the demonstrations of ferromagnetic ordering in ultrathin CrI_3, $Cr_2Ge_2Te_6$, and Fe_3GeTe_2. The rich family members with large tunability of MXene have been posed to be a promising 2D magnetic candidate via various theoretical approaches, yet, the experimental verification of magnetic behaviors in them are relatively rare. The first obstacle lies in the synthesis of high-quality MXenes, for example, the reports on the preparation of magnetic elemental Cr- or Mn-based, as well as nitride-based MXenes is limited. Recently, the demonstrations of magnetic characteristics in surface and defects engineering in representative $Ti_3C_2T_x$ MXene, and ordered double TMC $Cr_2TiC_2T_x$ show a promising start. Janus MXenes with asymmetrical composition and surface terminations can be an effective architecture to attain high magnetic anisotropy and magnetic ordering await experimental confirmations. The proximity effect in MXene based heterostructure enables the capability of spin and energy structure manipulations pointing out another avenue for intrigue quantum effects. Full MXene-based spintronic devices with minor lattice mismatching and large compatibility are expected. Multiferroics in MXenes that tightly twist ferromagnetic, ferroelectrics, or ferroelectrics show great opportunities in multifunctional nanodevices, although has been considered theoretically, but maybe a challenge for experimental endorsement. Magnetic materials are also promising for the applications of medical diagnostics, therapy, bio-imaging, and sensing. However, there are barely any reports on the investigation of magnetic MXene for these applications.

As seen from **Table 4** to **Table 6**, many studies have reported energy capacities of MXenes at the coin cell level. However, for the practical applications more detailed studies are needed at the pouch/cylindrical cell level to ultimately translate any advantages of MXenes to EVs. Typically, at the coin cell level, most capacities are calculated at an active material level without considering all the components of cell with low capacity ~few mAh. For practical applications, it is important to evaluate materials in a pouch cell format with >0.5-1 Ah capacity. In a pouch cell, surface functional groups on MXenes could result in gas evolution leading to pouch inflation. While LIBs have an average voltage of ~3.5 V, LSBs operate at a lower voltage ~2.1 V. In order to surpass LIBs, practical LSBs for EVs should have an areal capacity ~6.7 mA h cm^{-2}. Unfortunately, most of the reported data based on MXene-engineered cathodes (Tables 1 and 2) is significantly below the discussed sulfur loading level and areal capacity. Accordingly, the future studies using MXenes should focus on sulfur loading > 5 mg cm^{-2} with a discharge capacity of sulfur being up to 1000 mA h g^{-1}.

The unique combination of the chemical, electrical, optical and mechanical properties have made MXenes ideal building blocks for the fabrication of (bio)chemical and physical sensors including pressure/strain sensors. The tunable chemistry of MXenes via surface functionalization, passivation and intercalations offers highest control over the sensitivity resulting both from chemical recognition events and from the modification of the work function of the 2D material by simple functionalization with electron-donating or –withdrawing molecule, thus modulation of the Schottky barrier height (SBH) between MXenes and metallic contacts. By taking full advantage of such strategies, the detection limit of analytes and noise level of sensors can be enhanced. From the perspective of electrochemical sensors, surface functionalization of MXene with functional biomolecules endows MXene GCE with a specific selectivity towards the analytes. Importantly, the passivation of MXene surface, to moderate its interaction with oxygen, is of paramount importance if one wants to obtain MXene device with prolonged shelf life and operational stability. Finally, besides expanding the interlayer spacing of adjacent MXene flakes, intercalation chemistry of MXenes changes their resistance significantly. Taking advantage of this property, sensors with high selectivity to some certain molecules can be realized. This is due to the fact that molecular size and dipole moments and ionic charges from intercalants affect the electrical characteristics of MXene flakes distinctively. On the other hand, these functionalization strategies (functionalization, passivation and intercalations) are also extremely useful to tune the mechanical properties of the MXenes based hybrids for applications in pressure and strain sensing.

As a future of this drastically fast-growing domain of nanoscience and nanotechnology, it is strongly believed that MXenes and their hybrids have excellent prospects in a wide variety of fields ranging from energy materials to environmental applications. Most of aspects with MXenes are still in their infancy stage needing further investigations by all experimental, computational, and theoretical studies.

Acknowledgement

The activity in Strasbourg on MXenes was financially supported by the MX-OSMOPED project funded by the FLAG-ERA programme, the European Union and the Agence Nationale de la Recherche (ANR) (GA No. ANR-17-GRF1-0006-04), the EC Graphene Flagship Core 3 project (GA- 881603), the ANR through the Labex projects CSC (ANR-10-LABX-0026 CSC) within the Investissement d'Avenir program (ANR-10-120 IDEX-0002-02) and the International Center for Frontier Research in Chemistry (icFRC). This work is partially supported by the State Key Research Development Program of China (Grant No. 2019YFB2203503), National Natural Science Fund (Grant Nos. 61805146 61875138, 61961136001, and U1801254), and Science and Technology Innovation Commission of Shenzhen (KQTD2015032416270385, JCYJ20210324094204012, JCYJ20170811093453105, JCYJ20180307164612205, GJHZ20180928160209731 and KQJSCX20180321164801762), Innovation Team Project of

Department of Education of Guangdong Province (No. 2018KCXTD026) , Science and Technology Innovation Leading Talents Program of Guangdong Province (No. 2019TX05C343), College teacher characteristic innovation research project of Foshan(No. 2020SWYY01). Authors also acknowledge the support from Instrumental Analysis Center of Shenzhen University (Xili Campus). Ramakrishna Podila would like to thank Shailendra Chiluwal for his help and insightful comments.

References

1. A. VahidMohammadi, J. Rosen and Y. Gogotsi, *Science*, 2021, **372**, eabf1581.
2. M. Naguib, M. Kurtoglu, V. Presser, J. Lu, J. Niu, M. Heon, L. Hultman, Y. Gogotsi and M. W. Barsoum, *Advanced Materials*, 2011, **23**, 4248-4253.
3. M. Naguib, O. Mashtalir, J. Carle, V. Presser, J. Lu, L. Hultman, Y. Gogotsi and M. W. Barsoum, *ACS nano*, 2012, **6**, 1322-1331.
4. M. Naguib, V. N. Mochalin, M. W. Barsoum and Y. Gogotsi, *Advanced Materials*, 2014, **26**, 992-1005.
5. O. Mashtalir, M. R. Lukatskaya, M. Q. Zhao, M. W. Barsoum and Y. Gogotsi, *Advanced Materials*, 2015, **27**, 3501-3506.
6. B. Anasori, M. R. Lukatskaya and Y. Gogotsi, *Nature Reviews Materials*, 2017, **2**, 16098.
7. D. Geng, X. Zhao, Z. Chen, W. Sun, W. Fu, J. Chen, W. Liu, W. Zhou and K. P. Loh, *Advanced Materials*, 2017, **29**, 1700072.
8. Q. Xue, H. Zhang, M. Zhu, Z. Pei, H. Li, Z. Wang, Y. Huang, Y. Huang, Q. Deng and J. Zhou, *Advanced Materials*, 2017, **29**, 1604847.
9. X. Xiao, H. Wang, P. Urbankowski and Y. Gogotsi, *Chemical Society Reviews*, 2018, **47**, 8744-8765.
10. M. Malaki, A. Maleki and R. S. Varma, *Journal of Materials Chemistry A*, 2019, **7**, 10843-10857.
11. J. L. Hart, K. Hantanasirisakul, A. C. Lang, B. Anasori, D. Pinto, Y. Pivak, J. T. van Omme, S. J. May, Y. Gogotsi and M. L. Taheri, *Nature Communications*, 2019, **10**, 1-10.
12. J. Yang, M. Naguib, M. Ghidiu, L.-M. Pan, J. Gu, J. Nanda, J. Halim, Y. Gogotsi and M. W. Barsoum, *J. Am. Ceram. Soc.*, 2016, **99**, 660-666.
13. B. Ahmed, A. E. Ghazaly and J. Rosen, *Adv. Funct. Mater.*, 2020, **30**, 2000894.
14. B. Anasori, Y. Xie, M. Beidaghi, J. Lu, B. C. Hosler, L. Hultman, P. R. C. Kent, Y. Gogotsi and M. W. Barsoum, *ACS Nano*, 2015, **9**, 9507-9516.
15. G. Deysher, C. E. Shuck, K. Hantanasirisakul, N. C. Frey, A. C. Foucher, K. Maleski, A. Sarycheva, V. B. Shenoy, E. A. Stach, B. Anasori and Y. Gogotsi, *ACS Nano*, 2020, **14**, 204-217.
16. P. Urbankowski, B. Anasori, T. Makaryan, D. Q. Er, S. Kota, P. L. Walsh, M. Q. Zhao, V. B. Shenoy, M. W. Barsoum and Y. Gogotsi, *Nanoscale*, 2016, **8**, 11385-11391.
17. S. Yang, P. P. Zhang, F. X. Wang, A. G. Ricciardulli, M. R. Lohe, P. W. M. Blom and X. L. Feng, *Angewandte Chemie-International Edition*, 2018, **57**, 15491-15495.
18. P. Urbankowski, B. Anasori, K. Hantanasirisakul, L. Yang, L. H. Zhang, B. Haines, S. J. May, S. J. L. Billinge and Y. Gogotsi, *Nanoscale*, 2017, **9**, 17722-17730.
19. J. Jeon, Y. Park, S. Choi, J. Lee, S. S. Lim, B. H. Lee, Y. J. Song, J. H. Cho, Y. H. Jang and S. Lee, *ACS Nano*, 2018, **12**, 338-346.
20. Z. Y. Lin, L. J. Cai, W. Lu and Y. Chai, *Small*, 2017, **13**, 9.
21. X. Xiao, P. Urbankowski, K. Hantanasirisakul, Y. Yang, S. Sasaki, L. Yang, C. Chen, H. Wang, L. Miao, S. H. Tolbert, S. J. L. Billinge, H. D. Abruña, S. J. May and Y. Gogotsi, **0**, 1809001.

22. Y. Li, H. Shao, Z. Lin, J. Lu, L. Liu, B. Duployer, P. O. Å. Persson, P. Eklund, L. Hultman, M. Li, K. Chen, X.-H. Zha, S. Du, P. Rozier, Z. Chai, E. Raymundo-Piñero, P.-L. Taberna, P. Simon and Q. Huang, *Nature Materials*, 2020, **19**, 894-899.
23. M. Naguib, V. N. Mochalin, M. W. Barsoum and Y. Gogotsi, *Adv. Mater.*, 2014, **26**, 992-1005.
24. B. Anasori, M. R. Lukatskaya and Y. Gogotsi, *Nature Reviews Materials*, 2017, **2**, 16098.
25. C. Si, J. Zhou and Z. M. Sun, *Acs Applied Materials & Interfaces*, 2015, **7**, 17510-17515.
26. B. Anasori, C. Y. Shi, E. J. Moon, Y. Xie, C. A. Voigt, P. R. C. Kent, S. J. May, S. J. L. Billinge, M. W. Barsoum and Y. Gogotsi, *Nanoscale Horizons*, 2016, **1**, 227-234.
27. V. Kamysbayev, A. S. Filatov, H. Hu, X. Rui, F. Lagunas, D. Wang, R. F. Klie and D. V. Talapin, *Science*, 2020, **369**, 979-983.
28. M. Shekhirev, C. E. Shuck, A. Sarycheva and Y. Gogotsi, *Prog. Mater. Sci.*, 2021, **120**, 100757.
29. D. Zhang, D. Shah, A. Boltasseva and Y. Gogotsi, *ACS Photonics*, 2022, **9**, 1108-1116.
30. M. Han, K. Maleski, C. E. Shuck, Y. Yang, J. T. Glazar, A. C. Foucher, K. Hantanasirisakul, A. Sarycheva, N. C. Frey, S. J. May, V. B. Shenoy, E. A. Stach and Y. Gogotsi, *Journal of the American Chemical Society*, 2020, **142**, 19110-19118.
31. L. Wang, M. Han, C. E. Shuck, X. Wang and Y. Gogotsi, *Nano Energy*, 2021, **88**, 106308.
32. A. C. Foucher, M. Han, C. E. Shuck, K. Maleski, Y. Gogotsi and E. A. Stach, *2D Mater.*, 2022, **9**, 025004.
33. A. Jawaid, A. Hassan, G. Neher, D. Nepal, R. Pachter, W. J. Kennedy, S. Ramakrishnan and R. A. Vaia, *ACS Nano*, 2021, **15**, 2771-2777.
34. H. Shi, P. Zhang, Z. Liu, S. Park, M. R. Lohe, Y. Wu, A. Shaygan Nia, S. Yang and X. Feng, *Angewandte Chemie International Edition*, 2021, **60**, 8689-8693.
35. M. Alhabeb, K. Maleski, B. Anasori, P. Lelyukh, L. Clark, S. Sin and Y. Gogotsi, *Chemistry of Materials*, 2017, **29**, 7633-7644.
36. V. Natu, R. Pai, M. Sokol, M. Carey, V. Kalra and M. W. Barsoum, *Chem*, 2020, **6**, 616-630.
37. Q. Tao, M. Dahlqvist, J. Lu, S. Kota, R. Meshkian, J. Halim, J. Palisaitis, L. Hultman, M. W. Barsoum, P. O. Å. Persson and J. Rosen, *Nature Communications*, 2017, **8**, 14949.
38. S. M. M. M. Gheisari, R. Gavagsaz-Ghoachani, M. Malaki, P. Safarpour and M. Zandi, *Ultrasonics Sonochemistry*, 2018, **52**, 88-105.
39. A. Abdullah, A. Pak, M. M. Abdullah, A. Shahidi and M. Malaki, *Electronic Materials Letters*, 2014, **10**, 37-42.
40. A. Abdullah and M. Malaki, *Aerospace Science and Technology*, 2013, **28**, 31-39.
41. A. Abdullah, M. Malaki and E. Baghizadeh, *Proceedings of the Institution of Mechanical Engineers, Part C: Journal of Mechanical Engineering Science*, 2012, **226**, 681-694.
42. M. Malaki and A. Abdullah, *UPB Sci. Bull. Ser. A Appl. Math. Phys.*, 2012, **74**, 183-194.
43. M. Malaki and H. Ding, *Materials & Design*, 2015, **87**, 1072-1086.
44. B. Anasori, C. Shi, E. J. Moon, Y. Xie, C. A. Voigt, P. R. Kent, S. J. May, S. J. Billinge, M. W. Barsoum and Y. Gogotsi, *Nanoscale Horizons*, 2016, **1**, 227-234.
45. M. Khazaei, A. Ranjbar, M. Arai and S. Yunoki, *Journal of Materials Chemistry C*, 2017, **5**, 2488-2503.

46. Q. Jiang, Y. Lei, H. Liang, K. Xi, C. Xia and H. N. Alshareef, *Energy Storage Materials*, 2020, **27**, 78-95.
47. D. Pinto, B. Anasori, H. Avireddy, C. E. Shuck, K. Hantanasirisakul, G. Deysher, J. R. Morante, W. Porzio, H. N. Alshareef and Y. Gogotsi, *Journal of Materials Chemistry A*, 2020, **8**, 8957-8968.
48. K. R. G. Lim, M. Shekhirev, B. C. Wyatt, B. Anasori, Y. Gogotsi and Z. W. Seh, *Nature Synthesis*, 2022, **1**, 1-14.
49. K. Maleski, C. E. Ren, M.-Q. Zhao, B. Anasori and Y. Gogotsi, *ACS Applied Materials & Interfaces*, 2018, **10**, 24491-24498.
50. M. Malaki and R. S. Varma, *Advanced Materials*, 2020, **32**, 2003154.
51. M. Soleymaniha, M. A. Shahbazi, A. R. Rafieerad, A. Maleki and A. Amiri, *Advanced Healthcare Materials*, 2018, **8**, 1801137.
52. F. Shahzad, M. Alhabeb, C. B. Hatter, B. Anasori, S. M. Hong, C. M. Koo and Y. Gogotsi, *Science*, 2016, **353**, 1137-1140.
53. A. Miranda, J. Halim, M. Barsoum and A. Lorke, *Applied Physics Letters*, 2016, **108**, 033102.
54. X.-H. Zha, Q. Huang, J. He, H. He, J. Zhai, J. S. Francisco and S. Du, *Scientific reports*, 2016, **6**, 1-10.
55. K. Rasool, R. P. Pandey, P. A. Rasheed, S. Buczek, Y. Gogotsi and K. A. Mahmoud, *Materials Today*, 2019, **30**, 80-102.
56. M. R. Lukatskaya, S. Kota, Z. Lin, M.-Q. Zhao, N. Shpigel, M. D. Levi, J. Halim, P.-L. Taberna, M. W. Barsoum and P. Simon, *Nature Energy*, 2017, **2**, 1-6.
57. K. Huang, C. Li, H. Li, G. Ren, L. Wang, W. Wang and X. Meng, *ACS Applied Nano Materials*, 2020, **3**, 9581-9603.
58. S. J. Kim and H.-T. Jung, in *2D Metal Carbides and Nitrides (MXenes)*, Springer, 2019, ch. 24, pp. 457-480.
59. M. Ghidiu, M. R. Lukatskaya, M.-Q. Zhao, Y. Gogotsi and M. W. Barsoum, *Nature*, 2014, **516**, 78.
60. Y. J. Mai, Y. G. Li, S. L. Li, L. Y. Zhang, C. S. Liu and X. H. Jie, *Journal of Alloys and Compounds*, 2019, **770**, 1-5.
61. Y. Yue, N. Liu, Y. Ma, S. Wang, W. Liu, C. Luo, H. Zhang, F. Cheng, J. Rao, X. Hu, J. Su and Y. Gao, *ACS Nano*, 2018, **12**, 4224-4232.
62. W.-T. Cao, F.-F. Chen, Y.-J. Zhu, Y.-G. Zhang, Y.-Y. Jiang, M.-G. Ma and F. Chen, *ACS nano*, 2018, **12**, 4583-4593.
63. I. Ihsanullah, *Chemical Engineering Journal*, 2020, **388**, 124340.
64. A. Szuplewska, D. Kulpińska, A. Dybko, M. Chudy, A. M. Jastrzębska, A. Olszyna and Z. Brzózka, *Trends in Biotechnology*, 2020, **38**, 264-279.
65. K. Rasool, M. Helal, A. Ali, C. E. Ren, Y. Gogotsi and K. A. Mahmoud, *ACS Nano*, 2016, **10**, 3674-3684.
66. W. Wang, H. Feng, J. Liu, M. Zhang, S. Liu, C. Feng and S. Chen, *Chemical Engineering Journal*, 2020, **386**, 124116.

67. V. H. Nguyen, R. Tabassian, S. Oh, S. Nam, M. Mahato, P. Thangasamy, A. Rajabi-Abhari, W.-J. Hwang, A. K. Taseer and I.-K. Oh, *Advanced Functional Materials*, 2020, DOI: 10.1002/adfm.201909504, 1909504.
68. B. Anasori and Y. Gogotsi, *2D metal carbides and nitrides (MXenes)*, Springer, 2019.
69. W.-T. Cao, H. Ouyang, W. Xin, S. Chao, C. Ma, Z. Li, F. Chen and M.-G. Ma, *Advanced Functional Materials*, 2020, **30**, 2004181.
70. W.-T. Cao, C. Ma, D.-S. Mao, J. Zhang, M.-G. Ma and F. Chen, *Advanced Functional Materials*, 2019, **29**, 1905898.
71. X. Jiang, A. V. Kuklin, A. Baev, Y. Ge, H. Ågren, H. Zhang and P. N. Prasad, *Physics Reports*, 2020, DOI: https://doi.org/10.1016/j.physrep.2019.12.006.
72. S. Luo, S. Patole, S. Anwer, B. Li, T. Delclos, O. Gogotsi, V. Zahorodna, V. Balitskyi and K. Liao, *Nanotechnology*, 2020, **31**, 395704.
73. X. Sang, Y. Xie, M.-W. Lin, M. Alhabeb, K. L. Van Aken, Y. Gogotsi, P. R. Kent, K. Xiao and R. R. Unocic, *ACS Nano*, 2016, **10**, 9193-9200.
74. G. Plummer, B. Anasori, Y. Gogotsi and G. J. Tucker, *Computational Materials Science*, 2019, **157**, 168-174.
75. P. Chakraborty, T. Das, D. Nafday, L. Boeri and T. Saha-Dasgupta, *Physical Review B*, 2017, **95**, 184106.
76. Y. Luo, C. Cheng, H.-J. Chen, K. Liu and X.-L. Zhou, *Journal of Physics: Condensed Matter*, 2019, **31**, 405703.
77. S. A. Kazemi and Y. Wang, *Journal of Physics: Condensed Matter*, 2019, **32**, 11LT01.
78. R. Khaledialidusti, B. Anasori and A. Barnoush, *Physical Chemistry Chemical Physics*, 2020, **22**, 3414-3424.
79. N. Zhang, Y. Hong, S. Yazdanparast and M. A. Zaeem, *2D Materials*, 2018, **5**, 045004.
80. V. N. Borysiuk, V. N. Mochalin and Y. Gogotsi, *Nanotechnology*, 2015, **26**, 265705.
81. U. Yorulmaz, A. Özden, N. K. Perkgöz, F. Ay and C. Sevik, *Nanotechnology*, 2016, **27**, 335702.
82. X.-H. Zha, J. Yin, Y. Zhou, Q. Huang, K. Luo, J. Lang, J. S. Francisco, J. He and S. Du, *The Journal of Physical Chemistry C*, 2016, **120**, 15082-15088.
83. Y. Zhang, J. Li, L. Zhou and S. Xiang, *Solid State Communications*, 2002, **121**, 411-416.
84. J. M. Simoes and J. Beauchamp, *Chemical Reviews*, 1990, **90**, 629-688.
85. J. Häglund, A. F. Guillermet, G. Grimvall and M. Körling, *Physical Review B*, 1993, **48**, 11685.
86. T. Yamabe, K. Hori, T. Minato and K. Fukui, *Inorganic Chemistry*, 1980, **19**, 2154-2159.
87. S. D. Wijeyesekera and R. Hoffmann, *Organometallics*, 1984, **3**, 949-961.
88. B. C. Wyatt, A. Rosenkranz and B. Anasori, *Advanced Materials*, **33**, 2007973.
89. C. Kral, W. Lengauer, D. Rafaja and P. Ettmayer, *Journal of Alloys and Compounds*, 1998, **265**, 215-233.
90. S.-H. Jhi, S. G. Louie, M. L. Cohen and J. Ihm, *Physical Review Letters*, 2001, **86**, 3348.
91. M. Khazaei, A. Ranjbar, K. Esfarjani, D. Bogdanovski, R. Dronskowski and S. Yunoki, *Physical Chemistry Chemical Physics*, 2018, **20**, 8579-8592.
92. T. Ziegler, V. Tschinke and A. Becke, *Polyhedron*, 1987, **6**, 685-693.
93. K. A. Moltved and K. P. Kepp, *The Journal of Physical Chemistry C*, 2019, **123**, 18432-18444.

94. T. F. Magnera, D. E. David and J. Michl, *Journal of the American Chemical Society*, 1989, **111**, 4100-4101.
95. A. Lipatov, H. Lu, M. Alhabeb, B. Anasori, A. Gruverman, Y. Gogotsi and A. Sinitskii, *Science Advances*, 2018, **4**, eaat0491.
96. A. Lipatov, M. Alhabeb, H. Lu, S. Zhao, M. J. Loes, N. S. Vorobeva, Y. Dall'Agnese, Y. Gao, A. Gruverman and Y. Gogotsi, *Advanced Electronic Materials*, 2020, **6**, 1901382.
97. T. Hu, J. Yang, W. Li, X. Wang and C. M. Li, *Physical Chemistry Chemical Physics*, 2020, **22**, 2115-2121.
98. K. L. Firestein, J. E. von Treifeldt, D. G. Kvashnin, J. F. Fernando, C. Zhang, A. G. Kvashnin, E. V. Podryabinkin, A. V. Shapeev, D. P. Siriwardena and P. B. Sorokin, *Nano Letters*, 2020, **20**, 5900-5908.
99. J. Zhang, N. Kong, S. Uzun, A. Levitt, S. Seyedin, P. A. Lynch, S. Qin, M. Han, W. Yang and J. Liu, *Advanced Materials*, 2020, **32**, 2001093.
100. S. Wang, J.-X. Li, Y.-L. Du and C. Cui, *Computational Materials Science*, 2014, **83**, 290-293.
101. Z. Guo, J. Zhou, C. Si and Z. Sun, *Physical Chemistry Chemical Physics*, 2015, **17**, 15348-15354.
102. M. Kurtoglu, M. Naguib, Y. Gogotsi and M. W. Barsoum, *MRS Communications*, 2012, **2**, 133-137.
103. D. Akinwande, C. J. Brennan, J. S. Bunch, P. Egberts, J. R. Felts, H. Gao, R. Huang, J.-S. Kim, T. Li and Y. Li, *Extreme Mechanics Letters*, 2017, **13**, 42-77.
104. M. Topsakal, S. Cahangirov and S. Ciraci, *Applied Physics Letters*, 2010, **96**, 091912.
105. K. N. Kudin, G. E. Scuseria and B. I. Yakobson, *Physical Review B*, 2001, **64**, 235406.
106. R. C. Andrew, R. E. Mapasha, A. M. Ukpong and N. Chetty, *Physical Review B*, 2012, **85**, 125428.
107. K. Michel and B. Verberck, *Physical Review B*, 2009, **80**, 224301.
108. J. Deng, I. Fampiou, J. Liu, A. Ramasubramaniam and N. Medhekar, *Applied Physics Letters*, 2012, **100**, 251906.
109. R. C. Cooper, C. Lee, C. A. Marianetti, X. Wei, J. Hone and J. W. Kysar, *Physical Review B*, 2013, **87**, 035423.
110. Q. Yue, J. Kang, Z. Shao, X. Zhang, S. Chang, G. Wang, S. Qin and J. Li, *Physics Letters A*, 2012, **376**, 1166-1170.
111. C. Ataca, M. Topsakal, E. Akturk and S. Ciraci, *The Journal of Physical Chemistry C*, 2011, **115**, 16354-16361.
112. E. Cadelano, P. L. Palla, S. Giordano and L. Colombo, *Physical Review Letters*, 2009, **102**, 235502.
113. R. Wang, S. Wang, X. Wu and X. Liang, *Physica B: Condensed Matter*, 2010, **405**, 3501-3506.
114. J. Zhou and R. Huang, *Journal of the Mechanics and Physics of Solids*, 2008, **56**, 1609-1623.
115. X. Wei, B. Fragneaud, C. A. Marianetti and J. W. Kysar, *Physical Review B*, 2009, **80**, 205407.
116. V. N. Borysiuk, V. N. Mochalin and Y. Gogotsi, *Computational Materials Science*, 2018, **143**, 418-424.
117. T. Zhou, C. Wu, Y. Wang, A. P. Tomsia, M. Li, E. Saiz, S. Fang, R. H. Baughman, L. Jiang and Q. Cheng, *Nature Communications*, 2020, **11**, 2077.

118. X.-H. Zha, K. Luo, Q. Li, Q. Huang, J. He, X. Wen and S. Du, *EPL (Europhysics Letters)*, 2015, **111**, 26007.
119. Z. Fu, Q. Zhang, D. Legut, C. Si, T. Germann, T. Lookman, S. Du, J. Francisco and R. Zhang, *Physical Review B*, 2016, **94**, 104103.
120. J. Zhou, X. Zha, F. Y. Chen, Q. Ye, P. Eklund, S. Du and Q. Huang, *Angewandte Chemie*, 2016, **128**, 5092-5097.
121. C. Li, S. Yan, F. Zhang, J. He and F. Yin, *Vacuum*, 2019, **161**, 14-20.
122. C. Hu, Y. Zhou, Y. Bao and D. Wan, *Journal of the American Ceramic Society*, 2006, **89**, 3456-3461.
123. J. Chen and W. Zhao, *Tribology International*, 2021, **153**, 106598.
124. M. Marian, S. Tremmel, S. Wartzack, G. Song, B. Wang, J. Yu and A. Rosenkranz, *Applied Surface Science*, 2020, **523**, 146503.
125. D. Zhang, M. Ashton, A. Ostadhossein, A. C. van Duin, R. G. Hennig and S. B. Sinnott, *ACS Applied Materials & Interfaces*, 2017, **9**, 34467-34479.
126. H. Zhang, Z. Fu, D. Legut, T. Germann and R. Zhang, *RSC Advances*, 2017, **7**, 55912-55919.
127. T. Hu, M. Hu, Z. Li, H. Zhang, C. Zhang, J. Wang and X. Wang, *Physical Chemistry Chemical Physics*, 2016, **18**, 20256-20260.
128. Y. Guo, X. Zhou, D. Wang, X. Xu and Q. Xu, *Langmuir*, 2019, **35**, 14481-14485.
129. C. Jiang, C. Wu, X. Li, Y. Yao, L. Lan, F. Zhao, Z. Ye, Y. Ying and J. Ping, *Nano Energy*, 2019, **59**, 268-276.
130. X. Zhang, M. Xue, X. Yang, Z. Wang, G. Luo, Z. Huang, X. Sui and C. Li, *RSC Advances*, 2015, **5**, 2762-2767.
131. Y. Liu, X. Zhang, S. Dong, Z. Ye and Y. Wei, *Journal of Materials Science*, 2016, **52**, 2200-2209.
132. X. Zhou, Y. Guo, D. Wang and Q. Xu, *Tribology International*, 2021, **153**, 106646.
133. X. Yin, J. Jin, X. Chen, A. Rosenkranz and J. Luo, *ACS Applied Materials & Interfaces*, 2019, **11**, 32569-32576.
134. M. Marian, G. C. Song, B. Wang, V. M. Fuenzalida, S. Krauß, B. Merle, S. Tremmel, S. Wartzack, J. Yu and A. Rosenkranz, *Applied Surface Science*, 2020, **531**, 147311.
135. H. Yan, M. Cai, W. Li, X. Fan and M. Zhu, *Journal of Materials Science & Technology*, 2020, **54**, 144-159.
136. M. Malaki, W. Xu, A. K. Kasar, P. L. Menezes, H. Dieringa, R. S. Varma and M. Gupta, *Metals*, 2019, **9**, 330.
137. J. Hu, S. Li, J. Zhang, Q. Chang, W. Yu and Y. Zhou, *Chinese Chemical Letters*, 2019, **31**, 996-999.
138. H. Yan, J. Wang, C. Meng, X. Wang, S. Song, X. Fan, L. Zhang, H. Li, W. Li and M. Zhu, *Corrosion Science*, 2020, **174**, 108813.
139. X. Yin, J. Jin, X. Chen, A. Rosenkranz and J. Luo, *Advanced Engineering Materials*, 2020, **22**, 1901369.
140. S. Huang, K. C. Mutyala, A. V. Sumant and V. N. Mochalin, *Materials Today Advances*, 2021, **9**, 100133.

141. A. Rosenkranz, P. G. Grützmacher, R. Espinoza, V. M. Fuenzalida, E. Blanco, N. Escalona, F. J. Gracia, R. Villarroel, L. Guo, R. Kang, F. Mücklich, S. Suarez and Z. Zhang, *Applied Surface Science*, 2019, **494**, 13-21.
142. M. Xue, Z. Wang, F. Yuan, X. Zhang, W. Wei, H. Tang and C. Li, *RSC Advances*, 2017, **7**, 4312-4319.
143. J. Yang, B. Chen, H. Song, H. Tang and C. Li, *Crystal Research and Technology*, 2014, **49**, 926-932.
144. X. Zhang, Y. Guo, Y. Li, Y. Liu and S. Dong, *Chinese Chemical Letters*, 2019, **30**, 502-504.
145. A. Loganathan, P. Nautiyal, B. Boesl and A. Agarwal, *Nanomaterials and Energy*, 2019, **8**, 84-95.
146. W. Lian, Y. Mai, C. Liu, L. Zhang, S. Li and X. Jie, *Ceramics International*, 2018, **44**, 20154-20162.
147. H. Lashgari, M. R. Abolhassani, A. Boochani, S. M. Elahi and J. Khodadadi, *Solid State Commun.*, 2014, **195**, 61-69.
148. Y. Bai, K. Zhou, N. Srikanth, J. H. L. Pang, X. He and R. Wang, *RSC Adv.*, 2016, **6**, 35731-35739.
149. H. Zhang, G. Yang, X. Zuo, H. Tang, Q. Yang and G. Li, *Journal of Materials Chemistry A*, 2016, **4**, 12913-12920.
150. A. N. Enyashin and A. L. Ivanovskii, *J. Solid State Chem.*, 2013, **207**, 42-48.
151. M. Khazaei, M. Arai, T. Sasaki, C.-Y. Chung, N. S. Venkataramanan, M. Estili, Y. Sakka and Y. Kawazoe, 2013, **23**, 2185-2192.
152. J. R. Schaibley, H. Yu, G. Clark, P. Rivera, J. S. Ross, K. L. Seyler, W. Yao and X. Xu, *Nature Reviews Materials*, 2016, **1**, 16055.
153. L. Zhou, Y. Zhang, Z. Zhuo, A. J. Neukirch and S. Tretiak, *The Journal of Physical Chemistry Letters*, 2018, **9**, 6915-6920.
154. Y. Zhang, X.-H. Zha, K. Luo, N. Qiu, Y. Zhou, J. He, Z. Chai, Z. Huang, Q. Huang, Y. Liang and S. Du, *The Journal of Physical Chemistry C*, 2019, **123**, 6802-6811.
155. D. Magne, V. Mauchamp, S. Celerier, P. Chartier and T. Cabioc'h, *Phys. Rev. B*, 2015, **91**, 5.
156. G. R. Berdiyorov, 2016, **6**, 055105.
157. Y. Zhang, W. Xia, Y. Wu and P. Zhang, *Nanoscale*, 2019, **11**, 3993-4000.
158. X.-L. Qi and S.-C. Zhang, *Reviews of Modern Physics*, 2011, **83**, 1057-1110.
159. J. E. Moore, *Nature*, 2010, **464**, 194.
160. L. Müchler, F. Casper, B. Yan, S. Chadov and C. Felser, 2013, **7**, 91-100.
161. Z. Zhu, Y. Cheng and U. Schwingenschlögl, *Phys. Rev. B*, 2012, **85**, 235401.
162. Y. Lee, S. B. Cho and Y.-C. Chung, *ACS Applied Materials & Interfaces*, 2014, **6**, 14724-14728.
163. Y. Zhang, X.-H. Zha, K. Luo, Y. Qin, X. Bai, J. Xu, C.-T. Lin, Q. Huang and S. Du, *Chem. Phys. Lett.*, 2020, **760**, 137997.
164. Y. Li, N. Li, S. Zhao, J. Fan and J.-J. Kai, *Journal of Materials Chemistry A*, 2020, **8**, 760-769.
165. E. Balci, U. O. Akkus and S. Berber, *Journal of Materials Chemistry C*, 2017, **5**, 5956-5961.
166. E. Balcı, Ü. Ö. Akkuş and S. Berber, *Journal of Physics: Condensed Matter*, 2018, **30**, 155501.

167. Y. Lee, Y. Hwang, S. B. Cho and Y.-C. Chung, *Phys. Chem. Chem. Phys.*, 2014, **16**, 26273-26278.
168. E. Balcı, Ü. Ö. Akkuş and S. Berber, 2018, **113**, 083107.
169. S. A. Khan, G. Rehman, I. Ahmad, M. Maqbool, C. Franchini and B. Amin, *Chem. Phys. Lett.*, 2019, **731**, 136614.
170. Y. Liang, M. Khazaei, A. Ranjbar, M. Arai, S. Yunoki, Y. Kawazoe, H. Weng and Z. Fang, *Phys. Rev. B*, 2017, **96**, 195414.
171. J. K. El-Demellawi, S. Lopatin, J. Yin, O. F. Mohammed and H. N. Alshareef, *Acs Nano*, 2018, **12**, 8485-8493.
172. K. Chaudhuri, M. Alhabeb, Z. X. Wang, V. M. Shalaev, Y. Gogotsi and A. Boltasseva, *Acs Photonics*, 2018, **5**, 1115-1122.
173. R. R. Nair, P. Blake, A. N. Grigorenko, K. S. Novoselov, T. J. Booth, T. Stauber, N. M. R. Peres and A. K. Geim, *Science*, 2008, **320**, 1308-1308.
174. M. Bernardi, C. Ataca, M. Palummo and J. C. Grossman, 2017, **6**, 479-493.
175. K. Hantanasirisakul, M. Q. Zhao, P. Urbankowski, J. Halim, B. Anasori, S. Kota, C. E. Ren, M. W. Barsoum and Y. Gogotsi, *Advanced Electronic Materials*, 2016, **2**, 7.
176. J. Halim, M. R. Lukatskaya, K. M. Cook, J. Lu, C. R. Smith, L.-Å. Näslund, S. J. May, L. Hultman, Y. Gogotsi, P. Eklund and M. W. Barsoum, *Chemistry of Materials*, 2014, **26**, 2374-2381.
177. C. F. Zhang, B. Anasori, A. Seral-Ascaso, S. H. Park, N. McEvoy, A. Shmeliov, G. S. Duesberg, J. N. Coleman, Y. Gogotsi and V. Nicolosi, *Adv. Mater.*, 2017, **29**, 9.
178. Y. I. Jhon, M. Seo and Y. M. Jhon, *Nanoscale*, 2018, **10**, 69-75.
179. W. Shui, J. Li, H. Wang, Y. Xing, Y. Li, Q. Yang, X. Xiao, Q. Wen and H. Zhang, 2020, **8**, 2001120.
180. Q. Xu, L. Ding, Y. Y. Wen, W. J. Yang, H. J. Zhou, X. Z. Chen, J. Street, A. G. Zhou, W. J. Ong and N. Li, *Journal of Materials Chemistry C*, 2018, **6**, 6360-6369.
181. Q. Xue, H. J. Zhang, M. S. Zhu, Z. X. Pei, H. F. Li, Z. F. Wang, Y. Huang, Y. Huang, Q. H. Deng, J. Zhou, S. Y. Du, Q. Huang and C. Y. Zhi, *Adv. Mater.*, 2017, **29**, 6.
182. X. Chen, X. K. Sun, W. Xu, G. C. Pan, D. L. Zhou, J. Y. Zhu, H. Wang, X. Bai, B. A. Dong and H. W. Song, *Nanoscale*, 2018, **10**, 1111-1118.
183. A. Djire, H. Zhang, J. Liu, E. M. Miller and N. R. Neale, *ACS Applied Materials & Interfaces*, 2019, **11**, 11812-11823.
184. S. Lu, L. Sui, Y. Liu, X. Yong, G. Xiao, K. Yuan, Z. Liu, B. Liu, B. Zou and B. Yang, 2019, **6**, 1801470.
185. D. Huang, Y. Xie, D. Lu, Z. Wang, J. Wang, H. Yu and H. Zhang, **0**, 1901117.
186. G. F. Xu, Y. S. Niu, X. C. Yang, Z. Y. Jin, Y. Wang, Y. H. Xu and H. T. Niu, *Advanced Optical Materials*, 2018, **6**, 9.
187. Y. L. Qin, Z. Q. Wang, N. Y. Liu, Y. Sun, D. X. Han, Y. Liu, L. Niu and Z. H. Kang, *Nanoscale*, 2018, **10**, 14000-14004.
188. X. H. Zhu, L. Fan, S. G. Wang, C. Y. Lei, Y. Huang, Z. Nie and S. Z. Yao, *Analytical Chemistry*, 2018, **90**, 6742-6748.
189. Q. X. Zhang, F. Wang, H. X. Zhang, Y. Y. Zhang, M. L. Liu and Y. Liu, *Analytical Chemistry*, 2018, **90**, 12737-12744.

190. L. Zhou, F. Wu, J. Yu, Q. Deng, F. Zhang and G. Wang, *Carbon*, 2017, **118**, 50-57.
191. F. Bian, L. Sun, L. Cai, Y. Wang and Y. Zhao, 2020, **117**, 22736-22742.
192. X. Jiang, S. Liu, W. Liang, S. Luo, Z. He, Y. Ge, H. Wang, R. Cao, F. Zhang, Q. Wen, J. Li, Q. Bao, D. Fan and H. Zhang, *Laser & Photonics Reviews*, 2018, **12**, 1700229.
193. G. Wang, D. Bennett, C. Zhang, C. Ó Coileáin, M. Liang, N. McEvoy, J. J. Wang, J. Wang, K. Wang, V. Nicolosi and W. J. Blau, 2020, **8**, 1902021.
194. Q. Zhang, L. Yan, M. Yang, G. Wu, M. Hu, J. Li, K. Yuan and X. Yang, *The Journal of Physical Chemistry C*, 2020, **124**, 6441-6447.
195. G. J. Li, K. Kushnir, Y. C. Dong, S. Chertopalov, A. M. Rao, V. N. Mochalin, R. Podila and L. V. Titova, *2D Mater.*, 2018, **5**, 8.
196. W. L. Xiantao Jiang, Ting Hai, Rui Yue, Zhangwei Chen, Changshi Lao,Yanqi Ge, Guoqiang Xie, Qiao Wen, Han Zhang, *npj 2d Materials and Applications*, 2019, **3**.
197. Y. C. Dong, S. Chertopalov, K. Maleski, B. Anasori, L. Y. Hu, S. Bhattacharya, A. M. Rao, Y. Gogotsi, V. N. Mochalin and R. Podila, *Adv. Mater.*, 2018, **30**, 8.
198. Y. Song, Y. Chen, X. Jiang, Y. Ge, Y. Wang, K. You, K. Wang, J. Zheng, J. Ji, Y. Zhang, J. Li and H. Zhang, **0**, 1801777.
199. S. Zeng, D. Baillargeat, H.-P. Ho and K.-T. Yong, *Chemical Society Reviews*, 2014, **43**, 3426-3452.
200. V. Mauchamp, M. Bugnet, E. P. Bellido, G. A. Botton, P. Moreau, D. Magne, M. Naguib, T. Cabioc'h and M. W. Barsoum, *Phys. Rev. B*, 2014, **89**.
201. C. Y. Shi, M. Beidaghi, M. Naguib, O. Mashtalir, Y. Gogotsi and S. J. L. Billinge, *Phys. Rev. Lett.*, 2014, **112**, 5.
202. L. Rast, T. J. Sullivan and V. K. Tewary, *Phys. Rev. B*, 2013, **87**, 045428.
203. A. Sarycheva, T. Makaryan, K. Maleski, E. Satheeshkumar, A. Melikyan, H. Minassian, M. Yoshimura and Y. Gogotsi, *Journal of Physical Chemistry C*, 2017, **121**, 19983-19988.
204. K. Chaudhuri, A. Shaltout, D. Shah, U. Guler, A. Dutta, V. M. Shalaev and A. Boltasseva, *ACS Photonics*, 2019, **6**, 99-106.
205. D. B. Velusamy, J. K. El-Demellawi, A. M. El-Zohry, A. Giugni, S. Lopatin, M. N. Hedhili, A. E. Mansour, E. D. Fabrizio, O. F. Mohammed and H. N. Alshareef, 2019, **31**, 1807658.
206. L. Wu, Q. You, Y. Shan, S. Gan, Y. Zhao, X. Dai and Y. Xiang, *Sensors and Actuators B: Chemical*, 2018, **277**, 210-215.
207. Y. Xu, Y. S. Ang, L. Wu and L. K. Ang, 2019, **9**, 165.
208. P. Yasaei, Z. Hemmat, C. J. Foss, S. J. Li, L. Hong, A. Behranginia, L. Majidi, R. F. Klie, M. W. Barsoum, Z. Aksamija and A. Salehi-Khojin, *Adv. Mater.*, 2018, **30**, 8.
209. J. Halim, E. J. Moon, P. Eklund, J. Rosen, M. W. Barsoum and T. Ouisse, *Phys. Rev. B*, 2018, **98**, 11.
210. D. Xu, Z. Li, L. Li and J. Wang, 2020, **30**, 2000712.
211. K. Huang, Z. J. Li, J. Lin, G. Han and P. Huang, *Chemical Society Reviews*, 2018, **47**, 5109-5124.
212. B. Zhou, Y. Pu, H. Lin, W. Yue, H. Yin, Y. Yin, W. Ren, C. Zhao, Y. Chen and H. Xu, *Journal of Materials Chemistry B*, 2020, **8**, 5257-5266.
213. H. Lin, Y. W. Wang, S. S. Gao, Y. Chen and J. L. Shi, *Adv. Mater.*, 2018, **30**, 11.

214. W. Feng, X. Han, H. Hu, M. Chang, L. Ding, H. Xiang, Y. Chen and Y. Li, *Nature Communications*, 2021, **12**, 2203.
215. J. C. Lao, R. J. Lv, J. Gao, A. X. Wang, J. S. Wu and J. Y. Luo, *Acs Nano*, 2018, **12**, 12464-12471.
216. X. Fan, Y. Ding, Y. Liu, J. Liang and Y. Chen, *ACS Nano*, 2019, **13**, 8124-8134.
217. W.-T. Cao, W. Feng, Y.-Y. Jiang, C. Ma, Z.-F. Zhou, M.-G. Ma, Y. Chen and F. Chen, *Materials Horizons*, 2019, DOI: 10.1039/C8MH01566J.
218. Q. Zhang, G. Yi, Z. Fu, H. Yu, S. Chen and X. Quan, *ACS Nano*, 2019, **13**, 13196-13207.
219. C. Wang, Y. Wang, X. Jiang, J. Xu, W. Huang, F. Zhang, J. Liu, F. Yang, Y. Song, Y. Ge, Q. Wu, M. Zhang, H. Chen, J. Liu and H. Zhang, **0**, 1900060.
220. H. Xu, A. Ren, J. Wu and Z. Wang, 2020, **30**, 2000907.
221. W. Ouyang, J. Chen, J.-H. He and X. Fang, 2020, **6**, 2000168.
222. Z. Kang, Y. Ma, X. Tan, M. Zhu, Z. Zheng, N. Liu, L. Li, Z. Zou, X. Jiang, T. Zhai and Y. Gao, 2017, **3**, 1700165.
223. K. Montazeri, M. Currie, L. Verger, P. Dianat, M. W. Barsoum and B. Nabet, 2019, **31**, 1903271.
224. S. Chertopalov and V. N. Mochalin, *Acs Nano*, 2018, **12**, 6109-6116.
225. W. Deng, H. Huang, H. Jin, W. Li, X. Chu, D. Xiong, W. Yan, F. Chun, M. Xie, C. Luo, L. Jin, C. Liu, H. Zhang, W. Deng and W. Yang, 2019, **7**, 1801521.
226. A. Pan, X. Ma, S. Huang, Y. Wu, M. Jia, Y. Shi, Y. Liu, P. Wangyang, L. He and Y. Liu, *The Journal of Physical Chemistry Letters*, 2019, **10**, 6590-6597.
227. A. Ren, J. Zou, H. Lai, Y. Huang, L. Yuan, H. Xu, K. Shen, H. Wang, S. Wei, Y. Wang, X. Hao, J. Zhang, D. Zhao, J. Wu and Z. Wang, *Materials Horizons*, 2020, **7**, 1901-1911.
228. J. Jeon, H. Choi, S. Choi, J.-H. Park, B. H. Lee, E. Hwang and S. Lee, 2019, **29**, 1905384.
229. Z. Wang, Z. Cheng, C. Fang, X. Hou and L. Xie, *Composites Part A: Applied Science and Manufacturing*, 2020, **136**, 105956.
230. M.-S. Cao, Y.-Z. Cai, P. He, J.-C. Shu, W.-Q. Cao and J. Yuan, *Chemical Engineering Journal*, 2019, **359**, 1265-1302.
231. H.-C. Fu, V. Ramalingam, H. Kim, C.-H. Lin, X. Fang, H. N. Alshareef and J.-H. He, 2019, **9**, 1900180.
232. A. Agresti, A. Pazniak, S. Pescetelli, A. Di Vito, D. Rossi, A. Pecchia, M. Auf der Maur, A. Liedl, R. Larciprete, D. V. Kuznetsov, D. Saranin and A. Di Carlo, *Nature Materials*, 2019, **18**, 1228-1234.
233. N. D. Mermin and H. Wagner, *Phys. Rev. Lett.*, 1966, **17**, 1133-1136.
234. B. Huang, G. Clark, E. Navarro-Moratalla, D. R. Klein, R. Cheng, K. L. Seyler, D. Zhong, E. Schmidgall, M. A. McGuire, D. H. Cobden, W. Yao, D. Xiao, P. Jarillo-Herrero and X. Xu, *Nature*, 2017, **546**, 270-273.
235. C. Gong, L. Li, Z. Li, H. Ji, A. Stern, Y. Xia, T. Cao, W. Bao, C. Wang, Y. Wang, Z. Q. Qiu, R. J. Cava, S. G. Louie, J. Xia and X. Zhang, *Nature*, 2017, **546**, 265-269.
236. S. Liu, X. Yuan, Y. Zou, Y. Sheng, C. Huang, E. Zhang, J. Ling, Y. Liu, W. Wang, C. Zhang, J. Zou, K. Wang and F. Xiu, *npj 2D Materials and Applications*, 2017, **1**, 30.
237. M. Gibertini, M. Koperski, A. F. Morpurgo and K. S. Novoselov, *Nature Nanotechnology*, 2019, **14**, 408-419.

238. N. C. Frey, C. C. Price, A. Bandyopadhyay, H. Kumar and V. B. Shenoy, in *2D Metal Carbides and Nitrides (MXenes): Structure, Properties and Applications*, eds. B. Anasori and Y. Gogotsi, Springer International Publishing, Cham, 2019, DOI: 10.1007/978-3-030-19026-2_15, pp. 291-300.
239. H. Kim and H. N. Alshareef, *ACS Materials Letters*, 2020, **2**, 55-70.
240. M. Khazaei, M. Arai, T. Sasaki, C.-Y. Chung, N. S. Venkataramanan, M. Estili, Y. Sakka and Y. Kawazoe, *Adv. Funct. Mater.*, 2013, **23**, 2185-2192.
241. J. He, P. Lyu and P. Nachtigall, *Journal of Materials Chemistry C*, 2016, **4**, 11143-11149.
242. S. S. Li, S. J. Hu, W. X. Ji, P. Li, K. Zhang, C. W. Zhang and S. S. Yan, *Appl. Phys. Lett.*, 2017, **111**, 5.
243. Y. L. Yue, *J. Magn. Magn. Mater.*, 2017, **434**, 164-168.
244. Q. Gao and H. Zhang, *Nanoscale*, 2020, **12**, 5995-6001.
245. S.-W. Cheong and M. Mostovoy, *Nature Materials*, 2007, **6**, 13.
246. N. A. Spaldin, *Nature Reviews Materials*, 2017, **2**, 17017.
247. J.-J. Zhang, L. Lin, Y. Zhang, M. Wu, B. I. Yakobson and S. Dong, *Journal of the American Chemical Society*, 2018, **140**, 9768-9773.
248. H. Kumar, N. C. Frey, L. Dong, B. Anasori, Y. Gogotsi and V. B. Shenoy, *Acs Nano*, 2017, **11**, 7648-7655.
249. N. C. Frey, H. Kumar, B. Anasori, Y. Gogotsi and V. B. Shenoy, *ACS Nano*, 2018, **12**, 6319-6325.
250. G. Wang, *Journal of Physical Chemistry C*, 2016, **120**, 18850-18857.
251. G. Gao, G. Ding, J. Li, K. Yao, M. Wu and M. Qian, *Nanoscale*, 2016, **8**, 8986-8994.
252. J. Yang, X. Luo, X. Zhou, S. Zhang, J. Liu, Y. Xie, L. Lv and L. Chen, *Computational Materials Science*, 2017, **139**, 313-319.
253. S. Zhao, W. Kang and J. Xue, 2014, **104**, 133106.
254. Y. Zhang and F. Li, *J. Magn. Magn. Mater.*, 2017, **433**, 222-226.
255. X. Li, X. Wu, Z. Li, J. Yang and J. G. Hou, *Nanoscale*, 2012, **4**, 5680-5685.
256. X.-H. Zha, J.-C. Ren, L. Feng, X. Bai, K. Luo, Y. Zhang, J. He, Q. Huang, J. S. Francisco and S. Du, *Nanoscale*, 2018, **10**, 8763-8771.
257. N. C. Frey, A. Bandyopadhyay, H. Kumar, B. Anasori, Y. Gogotsi and V. B. Shenoy, *ACS Nano*, 2019, **13**, 2831-2839.
258. J. He, G. Ding, C. Zhong, S. Li, D. Li and G. Zhang, *Nanoscale*, 2019, **11**, 356-364.
259. A. Bandyopadhyay, D. Ghosh and S. K. Pati, *Phys. Chem. Chem. Phys.*, 2018, **20**, 4012-4019.
260. J. H. Yang, X. P. Luo, S. Z. Zhang and L. Chen, *Phys. Chem. Chem. Phys.*, 2016, **18**, 12914-12919.
261. X. F. Shao, X. B. Liu, X. M. Zhang, J. R. Wang and M. W. Zhao, *Phys. Chem. Chem. Phys.*, 2018, **20**, 3946-3952.
262. Z. Jiang, P. Wang, X. Jiang and J. J. Zhao, *Nanoscale Horizons*, 2018, **3**, 335-341.
263. Y. Yoon, T. A. Le, A. P. Tiwari, I. Kim, M. W. Barsoum and H. Lee, *Nanoscale*, 2018, **10**, 22429-22438.
264. B. Scheibe, K. Tadyszak, M. Jarek, N. Michalak, M. Kempiński, M. Lewandowski, B. Peplińska and K. Chybczyńska, *Applied Surface Science*, 2019, **479**, 216-224.

265. K. Hantanasirisakul, B. Anasori, S. Nemsak, J. L. Hart, J. Wu, Y. Yang, R. V. Chopdekar, P. Shafer, A. F. May, E. J. Moon, J. Zhou, Q. Zhang, M. L. Taheri, S. J. May and Y. Gogotsi, *Nanoscale Horizons*, 2020, **5**, 1557-1565.
266. J. H. Yang, S. Z. Zhang, A. P. Wang, R. N. Wang, C. K. Wang, G. P. Zhang and L. Chen, *Nanoscale*, 2018, **10**, 19492-19497.
267. E. Balci, U. O. Akkus and S. Berber, *Acs Applied Materials & Interfaces*, 2019, **11**, 3609-3616.
268. B. Z. Zhou, S. W. Ji, Z. Tian, W. J. Cheng, X. C. Wang and W. B. Mi, *Carbon*, 2018, **132**, 25-31.
269. N. Omar, M. Daowd, P. v. d. Bossche, O. Hegazy, J. Smekens, T. Coosemans and J. v. Mierlo, *Energies*, 2012, **5**, 2952-2988.
270. J. Lu, Z. Chen, Z. Ma, F. Pan, L. A. Curtiss and K. Amine, *Nature nanotechnology*, 2016, **11**, 1031.
271. K. Zaghib, A. Mauger, H. Groult, J. B. Goodenough and C. M. Julien, *Materials*, 2013, **6**, 1028-1049.
272. D. Deng, *Energy Science & Engineering*, 2015, **3**, 385-418.
273. E. J. Cairns and P. Albertus, *Annual review of chemical and biomolecular engineering*, 2010, **1**, 299-320.
274. D. Auston, S. Samuelsen, J. Brouwer, S. DenBaars, W. Glassley, B. Jenkins, P. Petersen and V. Srinivasan, *Collabra*, 2016, **2**.
275. F. Bonaccorso, L. Colombo, G. Yu, M. Stoller, V. Tozzini, A. C. Ferrari, R. S. Ruoff and V. Pellegrini, *Science*, 2015, **347**, 1246501.
276. F. Feng, J. Wu, C. Wu and Y. Xie, *Small*, 2015, **11**, 654-666.
277. M. Naguib, J. Come, B. Dyatkin, V. Presser, P.-L. Taberna, P. Simon, M. W. Barsoum and Y. Gogotsi, *Electrochemistry Communications*, 2012, **16**, 61-64.
278. O. Mashtalir, M. Naguib, V. N. Mochalin, Y. Dall'Agnese, M. Heon, M. W. Barsoum and Y. Gogotsi, *Nature Communications*, 2013, **4**, 1716.
279. Y. Xie, Y. Dall'Agnese, M. Naguib, Y. Gogotsi, M. W. Barsoum, H. L. Zhuang and P. R. Kent, *ACS nano*, 2014, **8**, 9606-9615.
280. C. Eames and M. S. Islam, *Journal of the American Chemical Society*, 2014, **136**, 16270-16276.
281. Y. Xie, M. Naguib, V. N. Mochalin, M. W. Barsoum, Y. Gogotsi, X. Yu, K.-W. Nam, X.-Q. Yang, A. I. Kolesnikov and P. R. Kent, *Journal of the American Chemical Society*, 2014, **136**, 6385-6394.
282. Q. Tang, Z. Zhou and P. Shen, *Journal of the American Chemical Society*, 2012, **134**, 16909-16916.
283. M. Naguib, J. Halim, J. Lu, K. M. Cook, L. Hultman, Y. Gogotsi and M. W. Barsoum, *Journal of the American Chemical Society*, 2013, **135**, 15966-15969.
284. C. Zhang, S. J. Kim, M. Ghidiu, M. Q. Zhao, M. W. Barsoum, V. Nicolosi and Y. Gogotsi, *Advanced Functional Materials*, 2016, **26**, 4143-4151.
285. M.-Q. Zhao, M. Torelli, C. E. Ren, M. Ghidiu, Z. Ling, B. Anasori, M. W. Barsoum and Y. Gogotsi, *Nano Energy*, 2016, **30**, 603-613.
286. J. Zhou, X. Zha, X. Zhou, F. Chen, G. Gao, S. Wang, C. Shen, T. Chen, C. Zhi and P. Eklund, *ACS nano*, 2017, **11**, 3841-3850.

287. C. Chen, M. Boota, X. Xie, M. Zhao, B. Anasori, C. E. Ren, L. Miao, J. Jiang and Y. Gogotsi, *Journal of Materials Chemistry A*, 2017, **5**, 5260-5265.
288. J. Xiong, L. Pan, H. Wang, F. Du, Y. Chen, J. Yang and C. J. Zhang, *Electrochimica Acta*, 2018, **268**, 503-511.
289. Y. T. Liu, P. Zhang, N. Sun, B. Anasori, Q. Z. Zhu, H. Liu, Y. Gogotsi and B. Xu, *Advanced Materials*, 2018, **30**, 1707334.
290. Z. Ma, X. Zhou, W. Deng, D. Lei and Z. Liu, *ACS Applied Materials & Interfaces*, 2018, **10**, 3634-3643.
291. H. Li, M. Lu, W. Han, H. Li, Y. Wu, W. Zhang, J. Wang and B. Zhang, *Journal of Energy Chemistry*, 2019, **38**, 50-54.
292. C. J. Zhang, S.-H. Park, A. Seral‐Ascaso, S. Barwich, N. McEvoy, C. S. Boland, J. N. Coleman, Y. Gogotsi and V. Nicolosi, *Nature communications*, 2019, **10**, 1-9.
293. Y. Tian, Y. An and J. Feng, *ACS Applied Materials & Interfaces*, 2019, **11**, 10004-10011.
294. F. Zhang, Z. Jia, C. Wang, A. Feng, K. Wang, T. Hou, J. Liu, Y. Zhang and G. Wu, *Energy*, 2020, **195**, 117047.
295. Y. Zhao, C. Liu, R. Yi, Z. Li, Y. Chen, Y. Li, I. Mitrovic, S. Taylor, P. Chalker and L. Yang, *Electrochimica Acta*, 2020, **345**, 136203.
296. G. Mu, D. Mu, B. Wu, C. Ma, J. Bi, L. Zhang, H. Yang and F. Wu, *Small*, 2020, **16**, 1905430.
297. D. Sun, Q. Hu, J. Chen, X. Zhang, L. Wang, Q. Wu and A. Zhou, *ACS Applied Materials & Interfaces*, 2016, **8**, 74-81.
298. C. E. Ren, M. Q. Zhao, T. Makaryan, J. Halim, M. Boota, S. Kota, B. Anasori, M. W. Barsoum and Y. Gogotsi, *ChemElectroChem*, 2016, **3**, 689-693.
299. X. Liang, Y. Rangom, C. Y. Kwok, Q. Pang and L. F. Nazar, *Advanced Materials*, 2017, **29**, 1603040.
300. W. Bao, L. Liu, C. Wang, S. Choi, D. Wang and G. Wang, *Advanced Energy Materials*, 2018, **8**, 1702485.
301. H. Tang, W. Li, L. Pan, C. P. Cullen, Y. Liu, A. Pakdel, D. Long, J. Yang, N. McEvoy and G. S. Duesberg, *Advanced Science*, 2018, **5**, 1800502.
302. H.-Y. Zhou, Z.-Y. Sui, K. Amin, L.-W. Lin, H.-Y. Wang and B.-H. Han, *ACS Applied Materials & Interfaces*, 2020, **12**, 13904-13913.
303. R. Gan, N. Yang, Q. Dong, N. Fu, R. Wu, C. Li, Q. Liao, J. Li and Z. Wei, 2020.
304. C. Xiong, G. Zhu, H. Jiang, Q. Chen and T. Zhao, *Energy Storage Materials*, 2020, **33**, 147-157.
305. F. Zhang, Y. Zhou, Y. Zhang, D. Li and Z. Huang, *Nanophotonics*, 2020, **1**.
306. N. Li, W. Cao, Y. Liu, H. Ye and K. Han, *Colloids and Surfaces A: Physicochemical and Engineering Aspects*, 2019, **573**, 128-136.
307. H. Pan, X. Huang, R. Zhang, D. Wang, Y. Chen, X. Duan and G. Wen, *Chemical Engineering Journal*, 2019, **358**, 1253-1261.
308. H. Zhang, Q. Qi, P. Zhang, W. Zheng, J. Chen, A. Zhou, W. Tian, W. Zhang and Z. Sun, *ACS Applied Energy Materials*, 2018, **2**, 705-714.
309. H. Tang, W. Li, L. Pan, K. Tu, F. Du, T. Qiu, J. Yang, C. P. Cullen, N. McEvoy and C. Zhang, *Advanced Functional Materials*, 2019, **29**, 1901907.

310. C. Du, J. Wu, P. Yang, S. Li, J. Xu and K. Song, *Electrochimica Acta*, 2019, **295**, 1067-1074.
311. Z. Pourali, M. R. Yaftian and M. R. Sovizi, *Materials Chemistry and Physics*, 2018, **217**, 117-124.
312. T. Zhao, P. Zhai, Z. Yang, J. Wang, L. Qu, F. Du and J. Wang, *Nanoscale*, 2018, **10**, 22954-22962.
313. W. Bao, X. Xie, J. Xu, X. Guo, J. Song, W. Wu, D. Su and G. Wang, *Chemistry–A European Journal*, 2017, **23**, 12613-12619.
314. W. Bao, D. Su, W. Zhang, X. Guo and G. Wang, *Advanced Functional Materials*, 2016, **26**, 8746-8756.
315. J. Song, X. Guo, J. Zhang, Y. Chen, C. Zhang, L. Luo, F. Wang and G. Wang, *Journal of Materials Chemistry A*, 2019, **7**, 6507-6513.
316. X. Wang, C. Yang, X. Xiong, G. Chen, M. Huang, J.-H. Wang, Y. Liu, M. Liu and K. Huang, *Energy Storage Materials*, 2019, **16**, 344-353.
317. X. T. Gao, Y. Xie, X. D. Zhu, K. N. Sun, X. M. Xie, Y. T. Liu, J. Y. Yu and B. Ding, *Small*, 2018, **14**, 1802443.
318. Y. Zhang, Z. Mu, C. Yang, Z. Xu, S. Zhang, X. Zhang, Y. Li, J. Lai, Z. Sun and Y. Yang, *Advanced Functional Materials*, 2018, **28**, 1707578.
319. Z. Xiao, Z. Li, P. Li, X. Meng and R. Wang, *ACS nano*, 2019, **13**, 3608-3617.
320. R. York, *Nature climate change*, 2012, **2**, 441-443.
321. S. Chu and A. Majumdar, *nature*, 2012, **488**, 294-303.
322. B. Huang, N. Zhou, X. Chen, W. J. Ong and N. Li, *Chemistry–A European Journal*, 2018, **24**, 18479-18486.
323. J. A. Turner, *Science*, 2004, **305**, 972-974.
324. Y. Tang, C. Yang, X. Xu, Y. Kang, J. Henzie, W. Que and Y. Yamauchi, *Advanced Energy Materials*, 2022, **12**, 2103867.
325. S. Ponnada, M. S. Kiai, D. B. Gorle, R. S. C. Bose, V. Rajagopal, B. Saini, M. Kathiresan, A. Nowduri, R. Singhal, F. Marken, M. A. Kulandainathan, K. K. Nanda and R. K. Sharma, *Catalysis Science & Technology*, 2022, **12**, 4413-4441.
326. T. Y. Ma, J. L. Cao, M. Jaroniec and S. Z. Qiao, *Angewandte Chemie International Edition*, 2016, **55**, 1138-1142.
327. Y. Yuan, H. Li, L. Wang, L. Zhang, D. Shi, Y. Hong and J. Sun, *ACS Sustainable Chemistry & Engineering*, 2019, **7**, 4266-4273.
328. Z. W. Seh, K. D. Fredrickson, B. Anasori, J. Kibsgaard, A. L. Strickler, M. R. Lukatskaya, Y. Gogotsi, T. F. Jaramillo and A. Vojvodic, *ACS Energy Letters*, 2016, **1**, 589-594.
329. V. Ramalingam, P. Varadhan, H.-C. Fu, H. Kim, D. Zhang, S. Chen, L. Song, D. Ma, Y. Wang, H. N. Alshareef and J.-H. He, *Advanced Materials*, 2019, **31**, 1903841.
330. Y. Jiang, T. Sun, X. Xie, W. Jiang, J. Li, B. Tian and C. Su, *ChemSusChem*, 2019, **12**, 1368-1373.
331. S. Li, P. Tuo, J. Xie, X. Zhang, J. Xu, J. Bao, B. Pan and Y. Xie, *Nano Energy*, 2018, **47**, 512-518.
332. M. H. Tran, T. Scha¨fer, A. Shahraei, M. Du¨rrschnabel, L. Molina-Luna, U. I. Kramm and C. S. Birkel, *ACS Applied Energy Materials*, 2018, **1**, 3908-3914.

333. Y. Yoon, A. P. Tiwari, M. Lee, M. Choi, W. Song, J. Im, T. Zyung, H.-K. Jung, S. S. Lee, S. Jeon and K.-S. An, *Journal of Materials Chemistry A*, 2018, **6**, 20869-20877.
334. W. Yuan, L. Cheng, Y. An, H. Wu, N. Yao, X. Fan and X. Guo, *ACS Sustainable Chemistry & Engineering*, 2018, **6**, 8976-8982.
335. S.-Y. Pang, Y.-T. Wong, S. Yuan, Y. Liu, M.-K. Tsang, Z. Yang, H. Huang, W.-T. Wong and J. Hao, *Journal of the American Chemical Society*, 2019, **141**, 9610-9616.
336. T. A. Le, Q. V. Bui, N. Q. Tran, Y. Cho, Y. Hong, Y. Kawazoe and H. Lee, *ACS Sustainable Chemistry & Engineering*, 2019, **7**, 16879-16888.
337. D. A. Kuznetsov, Z. Chen, P. V. Kumar, A. Tsoukalou, A. Kierzkowska, P. M. Abdala, O. V. Safonova, A. Fedorov and C. R. Mu¨ller, *Journal of the American Chemical Society*, 2019, **141**, 17809-17816.
338. J. Liang, C. Ding, J. Liu, T. Chen, W. Peng, Y. Li, F. Zhang and X. Fan, *Nanoscale*, 2019, **11**, 10992-11000.
339. N. H. Attanayake, S. C. Abeyweera, A. C. Thenuwara, B. Anasori, Y. Gogotsi, Y. Sun and D. R. Strongin, *Journal of Materials Chemistry A*, 2018, **6**, 16882-16889.
340. J. Ren, H. Zong, Y. Sun, S. Gong, Y. Feng, Z. Wang, L. Hu, K. Yu and Z. Zhu, *CrystEngComm*, 2020, **22**, 1395-1403.
341. X. Wu, Z. Wang, M. Yu, L. Xiu and J. Qiu, *Advanced Materials*, 2017, **29**, 1607017.
342. Y. Jiang, X. Wu, Y. Yan, S. Luo, X. Li, J. Huang, H. Zhang and D. Yang, *Small*, 2019, **15**, 1805474.
343. J. Zhang, Y. Zhao, X. Guo, C. Chen, C.-L. Dong, R.-S. Liu, C.-P. Han, Y. Li, Y. Gogotsi and G. Wang, *Nature Catalysis*, 2018, **1**, 985-992.
344. Z. Li, Z. Qi, S. Wang, T. Ma, L. Zhou, Z. Wu, X. Luan, F.-Y. Lin, M. Chen and J. T. Miller, *Nano Letters*, 2019, **19**, 5102-5108.
345. J. Filip, S. Zavahir, L. Lorencova, T. Bertok, A. B. Yousaf, K. A. Mahmoud, J. Tkac and P. Kasak, *Journal of The Electrochemical Society*, 2019, **166**, H54.
346. B. Cui, B. Hu, J. Liu, M. Wang, Y. Song, K. Tian, Z. Zhang and L. He, *ACS applied materials & interfaces*, 2018, **10**, 23858-23873.
347. X. Zhang, B. Shao, Z. Sun, Z. Gao, Y. Qin, C. Zhang, F. Cui and X. Yang, *Industrial & Engineering Chemistry Research*, 2020, **59**, 1822-1828.
348. X. Xie, Z. Wu and N. Zhang, *Chinese Chemical Letters*, 2020, **31**, 1014-1017.
349. C. Cui, R. Cheng, H. Zhang, C. Zhang, Y. Ma, C. Shi, B. Fan, H. Wang and X. Wang, *Advanced Functional Materials*, 2020, **30**, 2000693.
350. L. Tie, N. Li, C. Yu, Y. Liu, S. Yang, H. Chen, S. Dong, J. Sun, S. Dou and J. Sun, *ACS Applied Energy Materials*, 2019, **2**, 6931-6938.
351. P. Kuang, M. He, B. Zhu, J. Yu, K. Fan and M. Jaroniec, *Journal of Catalysis*, 2019, **375**, 8-20.
352. C.-F. Du, X. Sun, H. Yu, Q. Liang, K. N. Dinh, Y. Zheng, Y. Luo, Z. Wang and Q. Yan, *Advanced Science*, 2019, **6**, 1900116.
353. M. Yu, S. Zhou, Z. Wang, J. Zhao and J. Qiu, *Nano Energy*, 2018, **44**, 181-190.
354. C.-F. Du, K. N. Dinh, Q. Liang, Y. Zheng, Y. Luo, J. Zhang and Q. Yan, *Advanced Energy Materials*, 2018, **8**, 1801127.
355. L. Xiu, Z. Wang, M. Yu, X. Wu and J. Qiu, *ACS nano*, 2018, **12**, 8017-8028.

356. Y. Wen, P. Chen, L. Wang, S. Li, Z. Wang, J. Abed, X. Mao, Y. Min, C. T. Dinh and P. D. Luna, *Journal of the American Chemical Society*, 2021, **143**, 6482-6490.
357. J. Liu, T. Chen, P. Juan, W. Peng, Y. Li, F. Zhang and X. Fan, *ChemSusChem*, 2018, **11**, 3758-3765.
358. L. Zhao, B. Dong, S. Li, L. Zhou, L. Lai, Z. Wang, S. Zhao, M. Han, K. Gao and M. Lu, *ACS nano*, 2017, **11**, 5800-5807.
359. Y. Tang, C. Yang, Y. Yang, X. Yin, W. Que and J. Zhu, *Electrochimica Acta*, 2019, **296**, 762-770.
360. H. Zou, B. He, P. Kuang, J. Yu and K. Fan, *ACS applied materials & interfaces*, 2018, **10**, 22311-22319.
361. Y. Zhang, H. Jiang, Y. Lin, H. Liu, Q. He, C. Wu, T. Duan and L. Song, *Advanced Materials Interfaces*, 2018, **5**, 1800392.
362. X.-D. Zhu, Y. Xie and Y.-T. Liu, *Journal of Materials Chemistry A*, 2018, **6**, 21255-21260.
363. K. Zhao, X. Ma, S. Lin, Z. Xu and L. Li, *ChemistrySelect*, 2020, **5**, 1890-1895.
364. C. Wang, X.-D. Zhu, Y.-C. Mao, F. Wang, X.-T. Gao, S.-Y. Qiu, S.-R. Le and K.-N. Sun, *Chemical Communications*, 2019, **55**, 1237-1240.
365. N. Hao, Y. Wei, J. Wang, Z. Wang, Z. Zhu, S. Zhao, M. Han and X. Huang, *RSC Advances*, 2018, **8**, 20576-20584.
366. M. Benchakar, T. Bilyk, C. Garnero, L. Loupias, C. Morais, J. Pacaud, C. Canaff, P. Chartier, S. Morisset, N. Guignard, V. Mauchamp, S. Célérier and A. Habrioux, *Advanced Materials Interfaces*, 2019, **6**, 1901328.
367. C. Hao, Y. Wu, Y. An, B. Cui, J. Lin, X. Li, D. Wang, M. Jiang, Z. Cheng and S. Hu, *Materials Today Energy*, 2019, **12**, 453-462.
368. M. Tian, Y. Jiang, H. Tong, Y. Xu and L. Xia, *ChemNanoMat*, 2020, **6**, 154-159.
369. X. Li, Z. Zhang, Q. Xiang, R. Chen, D. Wu, G. Li and L. Wang, *RSC Advances*, 2021, **11**, 12392-12397.
370. L. Yan, B. Zhang, S. Wu and J. Yu, *Journal of Materials Chemistry A*, 2020, **8**, 14234-14242.
371. L. Hu, M. Li, X. Wei, H. Wang, Y. Wu, J. Wen, W. Gu and C. Zhu, *Chemical Engineering Journal*, 2020, **398**, 125605.
372. Y. Wen, Z. Wei, J. Liu, R. Li, P. Wang, B. Zhou, X. Zhang, J. Li and Z. Li, *Journal of Energy Chemistry*, 2021, **52**, 412-420.
373. J. Chen, Q. Long, K. Xiao, T. Ouyang, N. Li, S. Ye and Z.-Q. Liu, *Science Bulletin*, 2021, **66**, 1063-1072.
374. L. Hu, X. Zeng, X. Wei, H. Wang, Y. Wu, W. Gu, L. Shi and C. Zhu, *Applied Catalysis B: Environmental*, 2020, **273**, 119014.
375. Y. Lu, D. Fan, Z. Chen, W. Xiao, C. Cao and X. Yang, *Science Bulletin*, 2020, **65**, 460-466.
376. N. Li, Y. Jiang, C. Zhou, Y. Xiao, B. Meng, Z. Wang, D. Huang, C. Xing and Z. Peng, *ACS Appl Mater Interfaces*, 2019, **11**, 38116-38125.
377. L. X. Liu, W. Chen, H. B. Zhang, Q. W. Wang, F. Guan and Z. Z. Yu, *Advanced Functional Materials*, 2019, **29**.
378. H. An, T. Habib, S. Shah, H. Gao, A. Patel, I. Echols, X. Zhao, M. Radovic, M. J. Green and J. L. Lutkenhaus, *ACS Applied Nano Materials*, 2019, **2**, 948-955.
379. E. S. Muckley, M. Naguib and I. N. Ivanov, *Nanoscale*, 2018, **10**, 21689-21695.

380. A. Junkaew and R. Arroyave, *Phys Chem Chem Phys*, 2018, **20**, 6073-6082.
381. X. Zhao, L. Y. Wang, C. Y. Tang, X. J. Zha, Y. Liu, B. H. Su, K. Ke, R. Y. Bao, M. B. Yang and W. Yang, *ACS Nano*, 2020, **14**, 8793-8805.
382. P. Khakbaz, M. Moshayedi, S. Hajian, M. Soleimani, B. B. Narakathu, B. J. Bazuin, M. Pourfath and M. Z. Atashbar, *The Journal of Physical Chemistry C*, 2019, **123**, 29794-29803.
383. E. Lee, A. VahidMohammadi, B. C. Prorok, Y. S. Yoon, M. Beidaghi and D. J. Kim, *ACS Appl Mater Interfaces*, 2017, **9**, 37184-37190.
384. B. Xiao, Y.-c. Li, X.-f. Yu and J.-b. Cheng, *Sensors and Actuators B: Chemical*, 2016, **235**, 103-109.
385. S. H. Lee, W. Eom, H. Shin, R. B. Ambade, J. H. Bang, H. W. Kim and T. H. Han, *ACS Appl Mater Interfaces*, 2020, **12**, 10434-10442.
386. L. Zhao, Y. Zheng, K. Wang, C. Lv, W. Wei, L. Wang and W. Han, *Advanced Materials Technologies*, 2020, **5**.
387. Z. Yang, A. Liu, C. Wang, F. Liu, J. He, S. Li, J. Wang, R. You, X. Yan, P. Sun, Y. Duan and G. Lu, *ACS Sens*, 2019, **4**, 1261-1269.
388. H. J. Koh, S. J. Kim, K. Maleski, S. Y. Cho, Y. J. Kim, C. W. Ahn, Y. Gogotsi and H. T. Jung, *ACS Sens*, 2019, **4**, 1365-1372.
389. H. Pazniak, I. A. Plugin, M. J. Loes, T. M. Inerbaev, I. N. Burmistrov, M. Gorshenkov, J. Polcak, A. S. Varezhnikov, M. Sommer, D. V. Kuznetsov, M. Bruns, F. S. Fedorov, N. S. Vorobeva, A. Sinitskii and V. V. Sysoev, *ACS Applied Nano Materials*, 2020, **3**, 3195-3204.
390. W. Y. Chen, S. N. Lai, C. C. Yen, X. Jiang, D. Peroulis and L. A. Stanciu, *ACS Nano*, 2020, **14**, 11490-11501.
391. S. J. Kim, H.-J. Koh, C. E. Ren, O. Kwon, K. Maleski, S.-Y. Cho, B. Anasori, C.-K. Kim, Y.-K. Choi and J. Kim, *ACS Nano*, 2018, **12**, 986-993.
392. W. Y. Chen, X. Jiang, S. N. Lai, D. Peroulis and L. Stanciu, *Nat Commun*, 2020, **11**, 1302.
393. S. J. Kim, H. J. Koh, C. E. Ren, O. Kwon, K. Maleski, S. Y. Cho, B. Anasori, C. K. Kim, Y. K. Choi, J. Kim, Y. Gogotsi and H. T. Jung, *ACS Nano*, 2018, **12**, 986-993.
394. W. Yuan, K. Yang, H. Peng, F. Li and F. Yin, *Journal of Materials Chemistry A*, 2018, **6**, 18116-18124.
395. E. Lee, A. VahidMohammadi, Y. S. Yoon, M. Beidaghi and D. J. Kim, *ACS Sens*, 2019, DOI: 10.1021/acssensors.9b00303.
396. L. Zhao, K. Wang, W. Wei, L. Wang and W. Han, *InfoMat*, 2019, **1**, 407-416.
397. X. Wang, K. Sun, K. Li, X. Li and Y. Gogotsi, *Chinese Chemical Letters*, 2020, **31**, 1018-1021.
398. S. N. Shuvo, A. M. Ulloa Gomez, A. Mishra, W. Y. Chen, A. M. Dongare and L. A. Stanciu, *ACS Sens*, 2020, **5**, 2915-2924.
399. A. Hermawan, B. Zhang, A. Taufik, Y. Asakura, T. Hasegawa, J. Zhu, P. Shi and S. Yin, *ACS Applied Nano Materials*, 2020, **3**, 4755-4766.
400. W. Guo, S. G. Surya, V. Babar, F. Ming, S. Sharma, H. N. Alshareef, U. Schwingenschlogl and K. N. Salama, *ACS Appl Mater Interfaces*, 2020, **12**, 57218-57227.
401. J. H. Ciou, S. Li and P. S. Lee, *Small*, 2019, **15**, e1903281.
402. L. Lorencova, T. Bertok, E. Dosekova, A. Holazova, D. Paprckova, A. Vikartovska, V. Sasinkova, J. Filip, P. Kasak, M. Jerigova, D. Velic, K. A. Mahmoud and J. Tkac, *Electrochim Acta*, 2017, **235**, 471-479.

403. L. Lorencova, T. Bertok, J. Filip, M. Jerigova, D. Velic, P. Kasak, K. A. Mahmoud and J. Tkac, *Sensors and Actuators B: Chemical*, 2018, **263**, 360-368.
404. Z. Yang, L. Jiang, J. Wang, F. Liu, J. He, A. Liu, S. Lv, R. You, X. Yan, P. Sun, C. Wang, Y. Duan and G. Lu, *Sensors and Actuators B: Chemical*, 2021, **326**.
405. J. Choi, Y. J. Kim, S. Y. Cho, K. Park, H. Kang, S. J. Kim and H. T. Jung, *Advanced Functional Materials*, 2020, **30**.
406. C. Liu, S. Hao, X. Chen, B. Zong and S. Mao, *ACS Appl Mater Interfaces*, 2020, **12**, 32970-32978.
407. Y. Ma, N. Liu, L. Li, X. Hu, Z. Zou, J. Wang, S. Luo and Y. Gao, *Nat Commun*, 2017, **8**, 1207.
408. Y. Guo, M. Zhong, Z. Fang, P. Wan and G. Yu, *Nano Lett*, 2019, **19**, 1143-1150.
409. Y. Jin, B. Wen, Z. Gu, X. Jiang, X. Shu, Z. Zeng, Y. Zhang, Z. Guo, Y. Chen, T. Zheng, Y. Yue, H. Zhang and H. Ding, *Advanced Materials Technologies*, 2020, DOI: 10.1002/admt.202000262.
410. G. Y. Gou, M. L. Jin, B. J. Lee, H. Tian, F. Wu, Y. T. Li, Z. Y. Ju, J. M. Jian, X. S. Geng, J. Ren, Y. Wei, G. Y. Jiang, Y. Qiao, X. Li, S. J. Kim, M. Gao, H. T. Jung, C. W. Ahn, Y. Yang and T. L. Ren, *ACS Nano*, 2019, **13**, 12613-12620.
411. M. Chen, X. Hu, K. Li, J. Sun, Z. Liu, B. An, X. Zhou and Z. Liu, *Carbon*, 2020, **164**, 111-120.
412. V. Kedambaimoole, N. Kumar, V. Shirhatti, S. Nuthalapati, P. Sen, M. M. Nayak, K. Rajanna and S. Kumar, *ACS Sens*, 2020, **5**, 2086-2095.
413. Y. Gao, C. Yan, H. Huang, T. Yang, G. Tian, D. Xiong, N. Chen, X. Chu, S. Zhong, W. Deng, Y. Fang and W. Yang, *Advanced Functional Materials*, 2020, **30**.
414. T. H. Hyosung An, Smit Shah, Huili Gao, Miladin Radovic, Micah J. Green, Jodie L. Lutkenhaus, *Science Advances*, 2018, **4**, eaaq0118.
415. Y. Yang, L. Shi, Z. Cao, R. Wang and J. Sun, *Advanced Functional Materials*, 2019, **29**.
416. J.-H. Pu, X. Zhao, X.-J. Zha, L. Bai, K. Ke, R.-Y. Bao, Z.-Y. Liu, M.-B. Yang and W. Yang, *Journal of Materials Chemistry A*, 2019, **7**, 15913-15923.
417. Y. Cai, J. Shen, G. Ge, Y. Zhang, W. Jin, W. Huang, J. Shao, J. Yang and X. Dong, *ACS Nano*, 2018, **12**, 56-62.
418. S. Uzun, S. Seyedin, A. L. Stoltzfus, A. S. Levitt, M. Alhabeb, M. Anayee, C. J. Strobel, J. M. Razal, G. Dion and Y. Gogotsi, *Advanced Functional Materials*, 2019, **29**.
419. S. Seyedin, S. Uzun, A. Levitt, B. Anasori, G. Dion, Y. Gogotsi and J. M. Razal, *Advanced Functional Materials*, 2020, **30**.
420. K. Yang, F. Yin, D. Xia, H. Peng, J. Yang and W. Yuan, *Nanoscale*, 2019, **11**, 9949-9957.
421. T. Li, L. Chen, X. Yang, X. Chen, Z. Zhang, T. Zhao, X. Li and J. Zhang, *Journal of Materials Chemistry C*, 2019, **7**, 1022-1027.
422. Y. Yue, N. Liu, W. Liu, M. Li, Y. Ma, C. Luo, S. Wang, J. Rao, X. Hu, J. Su, Z. Zhang, Q. Huang and Y. Gao, *Nano Energy*, 2018, **50**, 79-87.
423. X. Shi, H. Wang, X. Xie, Q. Xue, J. Zhang, S. Kang, C. Wang, J. Liang and Y. Chen, *ACS Nano*, 2019, **13**, 649-659.
424. K. Wang, Z. Lou, L. Wang, L. Zhao, S. Zhao, D. Wang, W. Han, K. Jiang and G. Shen, *ACS Nano*, 2019, **13**, 9139-9147.

425. M. Zhu, Y. Yue, Y. Cheng, Y. Zhang, J. Su, F. Long, X. Jiang, Y. Ma and Y. Gao, *Advanced Electronic Materials*, 2019, **6**.
426. Q. Guo, X. Zhang, F. Zhao, Q. Song, G. Su, Y. Tan, Q. Tao, T. Zhou, Y. Yu, Z. Zhou and C. Lu, *ACS Nano*, 2020, **14**, 2788-2797.
427. Y. Cheng, Y. Ma, L. Li, M. Zhu, Y. Yue, W. Liu, L. Wang, S. Jia, C. Li, T. Qi, J. Wang and Y. Gao, *ACS Nano*, 2020, **14**, 2145-2155.
428. Y. Zhang, T. H. Chang, L. Jing, K. Li, H. Yang and P. Y. Chen, *ACS Appl Mater Interfaces*, 2020, **12**, 8392-8402.
429. E. Ricohermoso, F. Rosenburg, F. Klug, N. Nicoloso, H. F. Schlaak, R. Riedel and E. Ionescu, *Open Ceramics*, 2021, **5**.
430. Y. Cai, J. Shen, G. Ge, Y. Zhang, W. Jin, W. Huang, J. Shao, J. Yang and X. Dong, *ACS Nano*, 2018, **12**, 56-62.
431. K. H. L. Yi-Zhou Zhang, Dalaver H. Anjum, Rachid Sougrat, Qiu Jiang, Hyunho Kim, Husam N. Alshareef, *SCIENCE ADVANCES*, 2018, **4**, eaat0098.
432. Y. Ma, Y. Yue, H. Zhang, F. Cheng, W. Zhao, J. Rao, S. Luo, J. Wang, X. Jiang, Z. Liu, N. Liu and Y. Gao, *ACS Nano*, 2018, **12**, 3209-3216.
433. J. Liu, H. B. Zhang, X. Xie, R. Yang, Z. Liu, Y. Liu and Z. Z. Yu, *Small*, 2018, **14**, e1802479.
434. J. Zhang, L. Wan, Y. Gao, X. Fang, T. Lu, L. Pan and F. Xuan, *Advanced Electronic Materials*, 2019, **5**.
435. Y. Zhang, K. Chen, Y. Li, J. Lan, B. Yan, L. Shi and R. Ran, *ACS Appl Mater Interfaces*, 2019, **11**, 47350-47357.
436. H. Liao, X. Guo, P. Wan and G. Yu, *Advanced Functional Materials*, 2019, **29**.
437. L. Wang, M. Zhang, B. Yang, J. Tan and X. Ding, *ACS Nano*, 2020, **14**, 10633-10647.
438. J. S. Yichen Cai, Chi-Wen Yang, Yi Wan, Hao-Ling Tang, Areej A. Aljarb, Cailing Chen, Jui-Han Fu, Xuan Wei, Kuo-Wei Huang, Yu Han, Steven J. Jonas, Xiaochen Dong, Vincent Tung, *Science Advances*, 2020, **6**, eabb5367.
439. B. Xu, M. Zhu, W. Zhang, X. Zhen, Z. Pei, Q. Xue, C. Zhi and P. Shi, *Adv Mater*, 2016, **28**, 3333-3339.
440. J. Zheng, B. Wang, A. Ding, B. Weng and J. Chen, *Journal of Electroanalytical Chemistry*, 2018, **816**, 189-194.
441. B. Xu, M. Zhu, W. Zhang, X. Zhen, Z. Pei, Q. Xue, C. Zhi and P. Shi, *Advanced Materials*, 2016, **28**, 3333-3339.
442. H. L. Chia, C. C. Mayorga-Martinez, N. Antonatos, Z. Sofer, J. J. Gonzalez-Julian, R. D. Webster and M. Pumera, *Anal Chem*, 2020, **92**, 2452-2459.
443. J. Liu, X. Jiang, R. Zhang, Y. Zhang, L. Wu, W. Lu, J. Li, Y. Li and H. Zhang, *Advanced Functional Materials*, 2018, **29**.
444. Y. Lei, W. Zhao, Y. Zhang, Q. Jiang, J. H. He, A. J. Baeumner, O. S. Wolfbeis, Z. L. Wang, K. N. Salama and H. N. Alshareef, *Small*, 2019, **15**, e1901190.
445. S. S. Shankar, R. M. Shereema and R. B. Rakhi, *ACS Appl Mater Interfaces*, 2018, **10**, 43343-43351.
446. F. Zhao, Y. Yao, C. Jiang, Y. Shao, D. Barcelo, Y. Ying and J. Ping, *J Hazard Mater*, 2020, **384**, 121358.

447. P. A. Rasheed, R. P. Pandey, K. A. Jabbar, J. Ponraj and K. A. Mahmoud, *Analytical Methods*, 2019, **11**, 3851-3856.
448. S. Zhou, C. Gu, Z. Li, L. Yang, L. He, M. Wang, X. Huang, N. Zhou and Z. Zhang, *Applied Surface Science*, 2019, **498**.
449. R. Zhang, J. Liu and Y. Li, *ACS Sens*, 2019, **4**, 2058-2064.
450. N. S. Oliver, C. Toumazou, A. E. Cass and D. G. Johnston, *Diabet Med*, 2009, **26**, 197-210.
451. R. B. Rakhi, P. Nayak, C. Xia and H. N. Alshareef, *Sci Rep*, 2016, **6**, 36422.
452. H. Gu, Y. Xing, P. Xiong, H. Tang, C. Li, S. Chen, R. Zeng, K. Han and G. Shi, *ACS Applied Nano Materials*, 2019, **2**, 6537-6545.
453. J. Zheng, B. Wang, Y. Jin, B. Weng and J. Chen, *Mikrochim Acta*, 2019, **186**, 95.
454. Y. Yao, L. Lan, X. Liu, Y. Ying and J. Ping, *Biosens Bioelectron*, 2020, **148**, 111799.
455. Q. Xu, J. Xu, H. Jia, Q. Tian, P. Liu, S. Chen, Y. Cai, X. Lu, X. Duan and L. Lu, *Journal of Electroanalytical Chemistry*, 2020, **860**.
456. A. Saleh, S. Wustoni, E. Bihar, J. K. El-Demellawi, Y. Zhang, A. Hama, V. Druet, A. Yudhanto, G. Lubineau, H. N. Alshareef and S. Inal, *Journal of Physics: Materials*, 2020, **3**.
457. C. Xu, L. Wang, Z. Liu, L. Chen, J. Guo, N. Kang, X.-L. Ma, H.-M. Cheng and W. Ren, *Nature Materials*, 2015, **14**, 1135.
458. Q. Zhang, Y. Sun, M. Liu and Y. Liu, *Nanoscale*, 2020, **12**, 1826-1832.
459. Q. Xue, H. Zhang, M. Zhu, Z. Pei, H. Li, Z. Wang, Y. Huang, Y. Huang, Q. Deng, J. Zhou, S. Du, Q. Huang and C. Zhi, *Adv Mater*, 2017, **29**.
460. G. Yang, J. Zhao, S. Yi, X. Wan and J. Tang, *Sensors and Actuators B: Chemical*, 2020, **309**.
461. X. Chen, X. Sun, W. Xu, G. Pan, D. Zhou, J. Zhu, H. Wang, X. Bai, B. Dong and H. Song, *Nanoscale*, 2018, **10**, 1111-1118.
462. Q. Zhang, F. Wang, H. Zhang, Y. Zhang, M. Liu and Y. Liu, *Anal Chem*, 2018, **90**, 12737-12744.
463. Z. Guo, X. Zhu, S. Wang, C. Lei, Y. Huang, Z. Nie and S. Yao, *Nanoscale*, 2018, **10**, 19579-19585.
464. G. Cai, Z. Yu, P. Tong and D. Tang, *Nanoscale*, 2019, **11**, 15659-15667.
465. Q. Lu, J. Wang, B. Li, C. Weng, X. Li, W. Yang, X. Yan, J. Hong, W. Zhu and X. Zhou, *Anal Chem*, 2020, **92**, 7770-7777.
466. C. L. Manzanares-Palenzuela, A. M. Pourrahimi, J. Gonzalez-Julian, Z. Sofer, M. Pykal, M. Otyepka and M. Pumera, *Chem Sci*, 2019, **10**, 10010-10017.
467. H. Zhang, Z. Wang, Q. Zhang, F. Wang and Y. Liu, *Biosens Bioelectron*, 2019, **124-125**, 184-190.
468. H. Zhang, Z. Wang, F. Wang, Y. Zhang, H. Wang and Y. Liu, *Anal Chem*, 2020, **92**, 5546-5553.
469. X. Jiang, H. Wang, Y. Chai, W. Shi and R. Yuan, *Anal Chem*, 2020, **92**, 8992-9000.
470. N. Driscoll, A. G. Richardson, K. Maleski, B. Anasori, O. Adewole, P. Lelyukh, L. Escobedo, D. K. Cullen, T. H. Lucas, Y. Gogotsi and F. Vitale, *ACS Nano*, 2018, **12**, 10419-10429.
471. B. B. Murphy, P. J. Mulcahey, N. Driscoll, A. G. Richardson, G. T. Robbins, N. V. Apollo, K. Maleski, T. H. Lucas, Y. Gogotsi, T. Dillingham and F. Vitale, *Advanced Materials Technologies*, 2020, **5**.

Graphical abstract

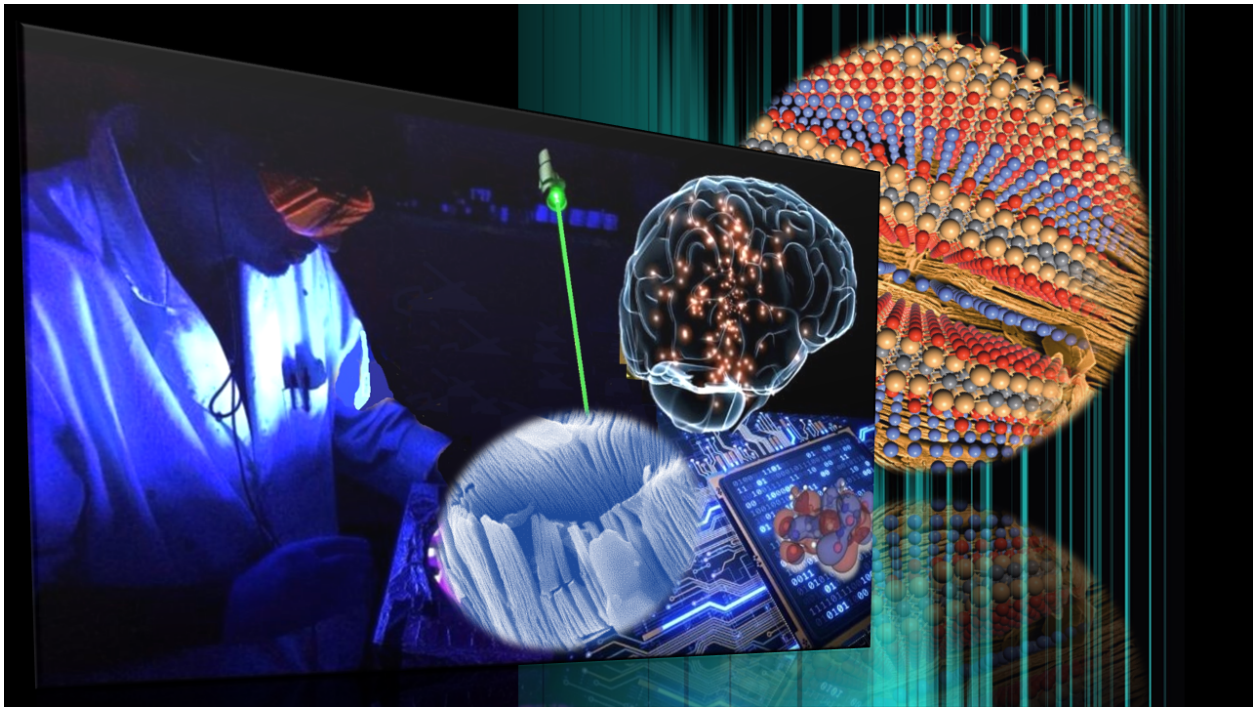

Biographies

Massoud Malaki received his B.Sc. and M.Sc. degrees in Mechanical Engineering from Shahid Rajaee University in 2006 and Amirkabir University of Technology (Tehran Polytechnic) in 2009, respectively. Before starting his PhD in the same field at Isfahan University of Technology, he worked in industry till 2015. He is currently working as a researcher at Isfahan University of Technology, his current research interests are mainly focused on the advanced synthesis of nano-materials, nanostructures and nanocomposites.

Xiantao Jiang is currently an associate professor at Sun Yat-Sen University. He obtained a doctoral degree in optics from Macquarie University, after receiving a Bachelor's degree from Sichuan University and a Master's degree from SICCAS. His research interests include mode-locked lasers, nonlinear optics, and transient absorption microscopy. He has authored over 50 peer-reviewed papers, which have attracted over 5000 citations with an h-index of 34.

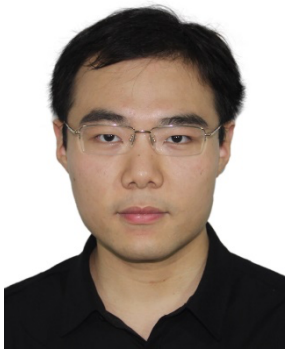

Hanlin Wang received his Ph.D. degree in Chemistry from the Institute of Chemistry, Chinese Academy of Sciences in 2017. He has worked on organic field-effect transistors and smart functional organic devices under the supervision of Prof. Wenping Hu and Prof. Yunqi Liu. Since 2018, he has been a postdoctoral researcher in the group of Prof. Paolo Samorì, University of Strasbourg, France. His current interest is opto-electronic devices based on integration of organic semiconductors and MXene-based 2D materials.

Ramakrishna Podila is presently an associate professor of physics at Clemson University. He obtained his MS and PhD in Physics from the Indian Institute of Technology (IIT) Roorkee and Clemson University, respectively. His PhD was focused on understanding defects in low-dimensional materials using optical spectroscopy. He worked as a post-doctoral fellow at the Brody School of Medicine (Greenville, NC) to study the biological applications of nanomaterials. The research interests of his lab are at the interface of physics, biology, and nanoscience. Dr. Podila's lab aims to seamlessly integrate the principles of condensed matter physics, optical spectroscopy, and physiological chemistry to understand physics at the nanoscale and nano-bio interfaces. His work thus far has led to >70 peer-reviewed articles (H-index: 46) in high-impact journals including Nature, Advanced Materials, Advanced Functional Materials, Journal of American Chemical Society, Nano Letters, 3 patents, and several invited talks.

Han Zhang received his Ph.D. degree from Nanyang Technological University, Singapore in 2010. He was a postdoc researcher in Université libre de Bruxelles from 2010 to 2012, then he moved back to Graphene Research Center, NUS, Singapore as a research fellow. From 2013, he became a full professor and established a research center titled "Shenzhen Engineering Laboratory of phosphorene and optoelectronics" at Shenzhen University. He has been awarded by multiple prizes, including Outstanding Ph.D. Abroad awarded by Chinese Government, New Century Excellent Talent Award, National Science Fund for Excellent Young Scholars, National Thousand Talents Program for Distinguished Young Scholars and so forth. To date, he has co-authored more than 400 peer-reviewed papers with a citation ≥ 69000 and a h-index ≥142. He is one of the Highly Cited Researchers by Clarivate Analytics in 2018 and 2019.

Paolo Samorì is Distinguished Professor at the University of Strasbourg and Director of the Institut de Science et d'Ingénierie Supramoléculaires. He is Fellow of the Royal Society of Chemistry (FRSC), Fellow of the European Academy of Sciences (EURASC), Member of the Academia Europaea, Foreign Member of the Royal Flemish Academy of Belgium for Science and the Arts (KVAB) and Senior Member of the Institut Universitaire de France (IUF). His research interests comprise nanochemistry, supramolecular sciences, materials chemistry with specific focus on graphene and other 2D materials as well as functional organic/polymeric and hybrid nanomaterials for application in optoelectronics, energy and sensing.

Rajender Varma (H-Index 125, Highly Cited Res. 2016, 18, 19, 20, 21, 22; Publons Awardee 2018-19) born in India (Ph.D., Delhi University 1976) is a senior scientist at U.S. EPA with a visiting position at RCPTM, Palacky University, Olomouc, Czech Republic. He has over 48 years of multidisciplinary research experience ranging from eco-friendly synthetic methods using microwaves, ultrasound, etc. to greener assembly of nanomaterials and sustainable appliances of magnetically retrievable nanocatalysts in benign media. He is a member of the editorial advisory board of several international journals, published over 700 papers, and awarded 17 U.S. Patents, 6 books, 26 book chapters, and 3 encyclopedia contributions with 62,000 citations.